

High Strain Rate Damage in Cerebral Arteries: A Molecular and Mechanical Analysis

by

Noah Robert Pearson

A dissertation submitted to the faculty of
The University of Utah
in partial fulfillment of the requirements for the degree of

Doctor of Philosophy

Department of Mechanical Engineering

The University of Utah

May 2023

Copyright © Noah Robert Pearson 2023

All Rights Reserved

ABSTRACT

Cerebral arteries are essential for the maintenance of a healthy brain, yet they are often mechanically injured in a manner that causes dysfunction. The mechanical response of the tissue is largely defined by a complex composition of macromolecules called the extracellular matrix (ECM). The impact of ECM damage on tissue function is poorly understood, but it is thought to influence the physiologic performance of the tissue. Previous studies of ECM damage have mostly investigated the effects of mechanical injury on the ECM and subsequent mechanical properties at quasi-static rates rather than the high strain rates that occur during traumatic brain injury (TBI). This study aims to fill this knowledge gap by examining rate-dependent shifts in tropocollagen denaturation, rate-dependent shifts in failure stress and stretch, and using a visco-hyperelastic constitutive model to describe the loading path through failure across a range of strain rates. In addition, we define the softening behavior of overstretched tissue at sub-yield stretches, showing that softening is independent of rate and not correlated with tropocollagen denaturation in this regime. Additional work is needed to identify the specific molecular structures in the ECM that are responsible for softening at sub-yield overstretch, as these structures may be used as markers of damage and targets for therapeutics.

TABLE OF CONTENTS

ABSTRACT	iii
LIST OF FIGURES	vi
1 INTRODUCTION	1
1.1 Motivation	1
1.2 Hypothesis and objective	2
1.3 Overview of work	3
2 BACKGROUND	4
2.0 Terminology	4
2.1 Cerebral Artery Structure	5
2.2 Collagen fiber structure	7
2.3 Microstructural damage in cerebral arteries	9
2.4 High-rate microstructural disruption in other tissue	10
2.5 Mechanics of arteries	11
2.6 Constitutive modeling of arteries	13
2.7 High-rate damage mechanics in soft tissue	18
3 A STRAIN RATE-DEPENDENT CONSTITUTIVE MODEL FOR GÖTTINGEN MINIPIG CEREBRAL ARTERIES	20
4 MOLECULAR-LEVEL COLLAGEN DAMAGE IS STRAIN RATE DEPENDENT IN CEREBRAL ARTERIES STRETCHED TO FAILURE	21
Notes	21
Abstract	21
1 Introduction	22
2. Materials and methods	26
3. Results	34
4. Discussion	42
Acknowledgements	51
CHAPTER 5 MECHANICAL SOFTENING IS INDEPENDENT OF STRAIN RATE IN CEREBRAL ARTERIES	53

Abstract	53
1. Introduction	54
2. Methods.....	56
3. Results	63
4. Discussion	72
Acknowledgements	82
CHAPTER 6 EXPLORATORY INVESTIGATION OF ECM ALTERATIONS.....	83
1. Introduction	83
2. Methods.....	85
3. Results	87
4. Discussion	91
CHAPTER 7 INTERSPECIES DIFFERENCE IN CHP EXPRESSION.....	94
1. Introduction	94
2. Methods.....	94
3. Results	95
4. Discussion	95
CHAPTER 8 CONCLUSION.....	96
6.1 Synopsis of Chapter 3: Mechanical rate dependence.....	97
6.2 Synopsis of Chapter 4: Tropocollagen denaturation.....	97
6.3 Synopsis of Chapter 5: Softening of viscoelastic properties.....	98
6.4 Synopsis of Chapter 6: Exploratory investigations	99
6.5 Synopsis of Chapter 7: Exploratory interspecies differences	99
6.6 Future work	99
REFERENCES	103

LIST OF FIGURES

Figure 1 Flowchart of image acquisition and processing	30
Figure 2 Image characteristics used during vessel processing.....	31
Figure 3 Adventitial tropocollagen denaturation in vessels stretched axially	35
Figure 4 Mean and standard deviation of collagen denaturation for collagen-aligned deformation.....	36
Figure 5 Medial tropocollagen denaturation in vessels stretched circumferentially	37
Figure 6 Representative images of medial slices in axially stretched vessels	38
Figure 7 Representative images of adventitial slices in circumferentially stretched vessels	39
Figure 8 Mean and standard deviation of collagen denaturation (percent bright pixels) in fibers transverse to the direction of loading.....	40
Figure 9 Schematic loading protocol	58
Figure 10 Custom high-rate tester.....	60
Figure 11 Dynamic modulus for all samples	64
Figure 12 Overstretch curves	66
Figure 13 Mean percent change in baseline stiffness	68
Figure 14 Softening as a function of overstretch, overstretch rate, and characterization frequency.....	69
Figure 15 CHP expression in arteries as a function of overstretch.....	71
Figure 16 Representative stress-stretch curves with unexpected CHP signal	72
Figure 17 Proposed relationship between ECM alteration and softening.....	80

Figure 18 GAG content for controls and failed samples	88
Figure 19 Representative SEM image of the adventitia of an MCA	89
Figure 20 Representative TEM images of MCAs.....	90

CHAPTER 1

INTRODUCTION

1.1 Motivation

The health of cerebral arteries is vital for meeting the high metabolic demands of neural tissue [1], yet they can be damaged in traumatic brain injury (TBI) [2, 3] and in surgical procedures such as angioplasty [4]. Dysfunction of these arteries can have severe consequences, including impaired cognition and tissue death [1]. It is thought that the cerebrovasculature resists brain deformations during TBI [5-7], but softening of these arteries could lead to increased compliance of the brain and an increased risk for more severe injuries in secondary impacts. The mechanical properties, and to a large degree the physiologic function, of cerebral arteries are driven by the extracellular matrix (ECM).

The extra-cellular matrix (ECM) is a complex network of molecules secreted by cells that provides structural support to the tissue [8-10]. The ECM is composed of a variety of macromolecules, including collagen, elastin, and proteoglycans, which interact with each other and with cells to form a three-dimensional scaffold that influences tissue architecture and mechanics [11]. The composition of the ECM is altered by various processes such as disease [11], surgery [12], and injury [3, 13]. The specific composition and arrangement of the ECM affects the mechanical properties of the tissue, such as its stiffness, strength, and viscoelastic behavior [14]. Understanding the interplay between

alterations of the ECM and changes to the mechanical response of the tissue is important for several fields of research, including the development of injury-specific therapeutics [15], optimization of medical devices [16], the development of constitutive models [16, 17], and the design of biomimetic materials [18, 19].

Mechanically induced damage to arteries has been well documented, including alterations of the ECM [20-22], cellular dysfunction [23], and gross tissue failure such as hemorrhage [24, 25]. Additionally, persistent mechanical changes have been identified in cerebral arteries following injury [26, 27]. Even though cerebral arteries experience high strain rate deformations in TBI [13], most of these studies have been conducted at quasi-static rates. Although some studies have noted the absence of rate dependence in cerebral arteries [28, 29], rate has been shown to increase vessel stiffness, failure stretch, and failure stretch [30]. Strain rate has been shown to affect patterns of ECM alteration during failure events of other collagenous soft tissue [10, 31-33], although this has not been studied in cerebral arteries. Finally, the coupled investigation of strain rate, softening, and changes to ECM composition has hardly been performed in any soft tissue, let alone cerebral arteries.

1.2 Hypothesis and objective

The objective of this dissertation was to characterize the progression of microstructural alterations and mechanical softening in cerebral arteries following injurious deformations at various strain rates. We hypothesized that both the development of tropocollagen denaturation and the mechanics of Göttingen minipig cerebral arteries are strain rate dependent. We aimed to define this rate-dependent stiffening in a ready-to-

implement constitutive model suitable for finite element (FE) simulations of traumatic brain injury (TBI). Additionally, we posited that microstructural damage caused by single-ramp overstretch manifests as changes to the viscoelastic mechanical properties of tissue.

1.3 Overview of work

In this doctoral project, we investigated the effect of strain rate on microstructural damage and the mechanical response of middle cerebral arteries (MCAs) from Göttingen minipigs. In Chapter 3, we developed a ready-to-implement constitutive model for the visco-hyperelastic properties of Göttingen minipig MCAs at rates ranging from 0.01 to 300 s⁻¹. In Chapter 4, we stretched the arteries to failure at both low (0.01 s⁻¹) and high (>100 s⁻¹) rates and quantified the rate-dependent changes in tropocollagen denaturation. We found that high-rate failure does not denature tropocollagen as much as low-rate failure. In Chapter 5, we performed subfailure overstretch at various strain rates and compared the evolution of softening with CHP expression. We observed dramatic softening in the absence of tropocollagen denaturation, suggesting that tropocollagen denaturation may not be relevant in single-ramp overstretch that stay below the yield point. In Chapter 6, we explore the use of other techniques to investigate mechanically induced alterations to the ECM. We do not recommend pursuing the explored techniques in our lab. Chapter 7 shows a likely yet not quite statistically significant difference in tropocollagen denaturation at failure between sheep and pigs. This suggests that a full study should examine interspecies differences in ECM alterations.

CHAPTER 2

BACKGROUND

2.0 Terminology

“Damage” is an ambiguous term in the soft-tissue community [16]. Tissue damage has been defined as “injury or harm that reduces value or usefulness” [34, 35]. “Usefulness” in tissue ECM is first and foremost the preservation of physiological function, regardless of whether this is to successfully carry mechanical load or provide an adequate substrate on which cells may thrive. The quantification of damage leads to an objective metric by which we can measure severity of physiologic dysfunction following injury. In the present work, we explore many forms of “damage” that all affect physiologic function. We thus provide a terminology section to avoid confusion as we explore these various forms.

To improve communication in this work, we try to avoid the term “damage” in lieu of more narrow descriptors. “Ultrastructural disruption” here refers to unspecified alterations of the ECM. “Tropocollagen denaturation” refers to changes to the tropocollagen molecule. Note that the terms “interstrand delamination,” “collagen denaturation,” “triple-helix unfolding,” “molecular-level unfolding,” “molecular denaturation,” and “molecular damage” are used in other works as synonymous with “tropocollagen denaturation” presently discussed [10, 36-40]. It is common for groups

use the term “damage” to refer to changes in the mechanical behavior of tissue [41-43]. However, as we limit the use of the term “damage,” we follow terminology often used in continuum damage models of soft tissue (i.e., [41, 44, 45]) leading us to use “softening” as the preferred term to describe permanent (i.e. irreversible) changes to the mechanical response of the tissue during repeated loading (that is, not monotonic stretch until failure). While not necessarily a separate phenomenon but rather a narrow manifestation of it, the decreasing stiffness of the native stress-stretch curve as it approaches failure, often referred to as “softening” [38, 43] is here referred to as “yielding,” although it needs to be pointed out that “yielding” is a controversial term in its own right [39]. Unless specified, all phenomena discussed can be assumed to be referring to passive mechanics rather than active mechanics; that is, the passive mechanical response of the tissue with no contribution of chemically triggered deformations such as those by vascular smooth muscle cells (VSMCs).

2.1 Cerebral Artery Structure

Cerebral arteries are a layered composite material. The intima is the innermost layer and is a sheet of endothelial cells adhered to a basement membrane [46]. An internal elastic lamina (IEL) separates the intima from the media [47], a middle layer made of circumferentially oriented collagen fibers interspersed with smooth muscle cells [48]. Most arteries have an external elastic lamina separating the media from the outermost layer, the adventitia, although this lamina is missing in cerebral arteries [49]. The adventitia is a layer made of axially oriented collagen fibers with fibroblasts as the primary cells [48].

The endothelial cells in the intima are active in physiological signaling. Among their most important roles associated with the regulation of blood flow is the detection of wall shear stress, which triggers changes in artery diameter via chemical signals to the VSMCs [50, 51]. The endothelial lining is also essential for the maintenance of a clear lumen; when the endothelium is disrupted, platelets begin to coagulate, leading to emboli [50].

The internal elastic lamina is made of elastin, a highly distensible protein with apparently excellent fatigue resistance [52] and low dissipation potential [53]. It is often thought that the IEL is responsible for arterial mechanical response to low-strain deformations [46, 54, 55], thus resisting physiologic blood pressures.

The collagen fibers in the media reside in two helically opposed fiber families with a slight offset ($\sim 1^\circ$) from the precise circumferential direction [49]. These fiber families are tightly dispersed, meaning that the directions of the individual fibers do not substantially deviate from the mean fiber family direction. As collagen plays the primary role in resisting deformations aligned with the fibers, the media primarily resists circumferential loading. The vascular smooth muscle cells lie in between the medial collagen fibers, and are more prevalent on the luminal side of the media than the adventitial side [48]. VSMCs play an essential role in regulating the cerebral blood flow. They constrict to reduce flow to less-active parts of the brain and dilate to direct blood to the more active locations [50, 51]. VSMCs have been shown to be directly sensitive to mechanical overstretch [11, 23, 56], as well as sensitive to changes in the properties of the ECM on which they are seeded [11].

Similar to in the media, the adventitial collagen is oriented in two helically opposed fiber families, although with a much greater offset ($\sim 22^\circ$ at 80 mmHg luminal pressure) from the axial direction than the medial fibers are from the circumferential direction [48]. Additionally, the fiber families have a large distribution of individual fiber directions, leading to a more diverse group of collagen fibers. The adventitia is thought to primarily resist axial loading given the relatively small angle of the helices to the axial direction. As the fibers are less aligned with the expected directions of loading (i.e., circumferential loading for overpressure), it is expected that the adventitial fibers will go through larger motions (rotations) during loading.

2.2 Collagen fiber structure

Fibrous collagen is a strongly hierarchical structure spanning many length scales. The largest structure that we discuss in the context of arteries is the collagen fiber. Although it is named a “collagen” fiber, there are in fact many other (non-collagen) proteins, sugars, and molecules within the hierarchy. Collagen fibrils, bound together with interfibrillar crosslinks, form the backbone of the collagen fiber [16]. The interfibrillar crosslinks are primarily proteoglycans in healthy tissue [14, 57].

Many different proteoglycans are found in the artery wall with varying functions. The reader is referred to [58] for a complete description of proteoglycans identified in arteries. Proteoglycans are themselves composite structures made of a protein backbone covalently bonded to negatively charged glycosaminoglycans (GAG) branches regularly spaced along the protein. The negative charge on GAGs makes them hydrophilic, allowing them to support local compressive strains [14].

A collagen fibril comprises tropocollagen molecules bound together with various enzymatic covalent or trivalent crosslinks [59], although a deleterious molecule termed advanced glycation end product (AGE) accumulates between the tropocollagens during aging [60, 61]. The tropocollagen molecules are packed together in a repetitive, highly organized manner. Each head of the tropocollagen molecule is offset by 67 nm from the head of its nearest neighbor [57, 62], leading to striations referred to as “d-bands,” based on patterns observed in electron microscopy. Furthermore, there is a gap of $0.6D$ between the head and tail of neighboring coaxial tropocollagen molecules, observable as negative space by techniques such as electron microscopy and atomic force microscopy. In the context of d-banding, length D is the characteristic length between the heads of adjacent tropocollagen molecules. It is equal to 67 nm [57].

The tropocollagen molecules are a triple helix of three unique alpha chains wound into a single molecule. Types I-III collagen are the most common fibrillar collagen [62, 63], with types I and III the most typical in arteries [64]. They differ in the construct of the triple helix; type III collagen is a homomer of three $\alpha(I)$ -chains whereas type I collagen comprises two $\alpha(I)$ -chains and one $\alpha(II)$ -chain [59, 63]. This small difference manifests itself as a reduction in fibril diameter of type III collagen compared with type I [65], and a decrease in telopeptide chains [62]. In aorta, the adventitia is primarily made of type I collagen whereas the media is approximately 70% type III and 30% type I collagen [64]. As type III collagen appears to be associated with elastic fibers [64], the ratio of type I:III collagen may be different in the muscular cerebral arteries.

Finally, the individual alpha chains are polypeptide chains with the highly repeating peptide sequence (gly-x-y), where gly is glycine and x and y are often proline

and hydroxyproline [66-68]. As hydroxyproline is generally restricted to collagen and is quite uniformly distributed, assays to detect the prevalence of hydroxyproline are commonly used to quantify the amount of collagen in a tissue [31].

2.3 Microstructural damage in cerebral arteries

There have been limited studies on microstructural damage in cerebral arteries following mechanical injury, and those that do exist have all been done under quasi-static loading conditions. An early series of research on the effects of angioplasty-induced circumferential overstretch in cerebral arteries led to observations of fiber tearing, fiber reorientation, medial thinning, splitting of the IEL, and morphological changes to smooth muscle cells [69]. More recently, Converse *et al.* identified mechanically induced denaturation of tropocollagen using collagen-hybridizing peptide (CHP) in ovine middle cerebral arteries (MCAs) [39]. They found that the onset of tropocollagen denaturation coincided with the mechanical yield point of the arteries, suggesting that the denaturation of tropocollagen is responsible for yielding. Additionally, Marino *et al.* fit the data from [39] to a continuum damage model, accounting for plastic fiber strain (presumed to be a result of tropocollagen denaturation) and final fiber rupture [38]. They found that fitting the plastic fiber strain to the CHP results of denatured tropocollagen led to a favorable prediction of the mechanical response of the tissue, reinforcing the conclusion that tropocollagen denaturation is strongly associated with yielding.

2.4 High-rate microstructural disruption in other tissue

High strain-rate ECM alterations have not been explored in cerebral arteries. It has, however, been somewhat explored in other collagenous soft tissues, albeit not extensively. The few studies that do exist suggest a definite change in mechanical properties as a function of strain rate. Willet *et al.* found a rate-induced decrease in the amount of acetyltryptin and α -chymotrypsin-TLCK digestion of failed tendon [31]. They later confirmed this rate dependence using differential scanning calorimetry (DSC), and further showed that tropocollagen disruption is present far away from the rupture site in failed tissue [32]. Similarly, Chambers *et al.* identified a rate-induced decrease in fibrillar kinking [33], an ultrastructural failure mode identified several years earlier by Veres and Lee [36]. Interestingly, Chambers *et al.* noted that tissue with higher concentrations of intrafibrillar crosslinks were more resistant to fibrillar kinking at all strain rates, with all evidence of damage gone in highly crosslinked tendons at their highest rate tested. Veres and Lee previously associated the locations of fibril kinking with digestion-induced voids in the tissue [36], suggesting that the effects Chambers *et al.* observed are the same phenomenon noted by Willet *et al.*: denatured tropocollagen. Zitnay *et al.* strengthened the notion that tropocollagen denaturation is rate dependent during cyclic creep experiments where they found less tropocollagen damage per cycle at high (0.40 s^{-1}) rates compared with low (0.004 s^{-1}) rates [10]. The mechanism behind the rate dependence of tropocollagen denaturation was earlier proposed by Zitnay *et al.* to be a result of hydrogen bonds dominating the quasi-static response of tropocollagen while the much stronger covalent bonds dominate the high-rate response [37].

2.5 Mechanics of arteries

2.5.1 Overview

Cerebral arteries are an orthotropic hyperelastic material with stress-stretch curves in both the circumferential and axial directions typically observed with a toe region transitioning into a long linear portion that finally yields through a pronounced plateau region until final rupture. They are often assumed to be incompressible [38, 70, 71], although this assumption has been repeatedly challenged, especially at high deformations [30, 72-76]. Arteries have a characteristic feature in their pressure-axial force curves at different axial stretches. There is an axial stretch where changes in pressure (between 80 and 120 mmHg) do not lead to changes in axial force. This is considered to be the *in vivo* length of arteries [8, 77]. When exposed to axial supraphysiologic loading, arteries exhibit an exponential-linear stress-stretch curve before yielding into a pronounced failure plateau.

2.5.2 Mechanical softening in cerebral arteries

Few groups have investigated mechanical softening in cerebral arteries. Bell *et al.* were the first to characterize the softening of the material in a sheep MCA model [26]. They found a clear progression of tissue softening as a result of mechanical overstretch, characterized by changes in tare load, *in vivo* stiffness, and strain energy of the tissue. They evaluated the influence of time on the recovery of baseline properties to check if the observed softening was a result of viscous processes, but did not observe any measurable recovery of properties over more than 60 minutes. Upon a secondary stretch (after the initial overstretch) to failure, the failure properties of tissue were not altered, which is

consistent with Mullins-type softening where materials return to their native loading path once they have been distended past their previous maximum deformation. Converse *et al.* were the only others to directly investigate passive mechanical softening in cerebral arteries [27]. In this work, they identify softening in both the axial and circumferential directions following axial overstretch, although the reduction in stress at the *in vivo* configuration was ten times greater in the axial direction than the circumferential direction. They speculate that this directional discrepancy may be a result of damage to the adventitial fibers, which are primarily axially oriented yet have enough of an off-axis angle to affect the circumferential properties.

2.5.3 Rate dependence in arteries

Reports on the dependence of strain rate on the mechanics of cerebral arteries are surprisingly variable. Chalupnik *et al.* [28] and Monson *et al.* [29] did not find rate dependence in cerebral arteries across a range of four orders of magnitude of strain rates. These results were recently countered by Bell *et al.* [30] who found a significant increase in failure stress as strain rate increased. Most studies of other (extra-cranial) arteries have shown some sort of rate effect, largely noting an increase in failure stress [78-80] with some also identifying a decrease in failure stretch [78, 80] and increasing stiffness [78, 80, 81]. Lee and Haut, however, did not find any change in the failure mechanics of carotid arteries across three orders of magnitude of strain rate [82].

2.6 Constitutive modeling of arteries

2.6.1 Quasi-static constitutive modeling

Most contemporary continuum formulations for artery mechanics multiplicatively decompose the deformation gradient into dilatational and distortional portions $\mathbf{F} = J^{1/3}\bar{\mathbf{F}}$ where the volume-preserving portion $\bar{\mathbf{F}}$ is defined by the property $\det\bar{\mathbf{F}} \equiv 1$ and the volume ratio $J = \det\mathbf{F} > 0$. The symmetric right ($\mathbf{C} = \mathbf{F}^T\mathbf{F}$) or left ($\mathbf{b} = \mathbf{F}\mathbf{F}^T$) Cauchy-Green tensors are material and spatial deformation tensors. The modified isochoric equivalents of these are subsequently $\bar{\mathbf{C}} = \bar{\mathbf{F}}^T\bar{\mathbf{F}}$ and $\bar{\mathbf{b}} = \bar{\mathbf{F}}\bar{\mathbf{F}}^T$.

Deformations are generally assumed to be isothermal processes that can be characterized by a free-energy function Ψ . The free-energy equation is generally written in a decoupled form such that $\Psi(\mathbf{C}) = \Psi_{vol}(J) + \Psi_{iso}(\bar{\mathbf{C}})$. Here, the convex function $\Psi_{vol}(J)$ is defined such that the dilatational energy is minimized at $J = 1$, often of the form $\Psi_{vol}(J) = -p(J - 1)$. Running with the assumption of incompressibility, the volume ratio J is generally forced to singularity and the pressure term p is used as a Lagrange multiplier to enforce the constraint. The isochoric portion of the free energy equation $\Psi_{iso}(\bar{\mathbf{C}})$ is often decoupled to account for anisotropy by including an isotropic term $\Psi_{isotr}(\bar{I}_1, \bar{I}_2)$ and an anisotropic term $\Psi_{aniso}(\bar{I}_4, \bar{I}_6)$ such that $\Psi_{iso}(\bar{\mathbf{C}}, \mathbf{a}_{0,1}, \mathbf{a}_{0,2}) = \Psi_{isotr}(\bar{I}_1, \bar{I}_2) + \Psi_{aniso}(\bar{I}_4, \bar{I}_6)$. The invariants \bar{I}_1 and \bar{I}_2 are frame indifferent representations of the principal and deviatoric properties of $\bar{\mathbf{C}}$ such that $\bar{I}_1 = \text{tr}(\bar{\mathbf{C}})$ and $\bar{I}_2 = \frac{1}{2}\{(\text{tr}(\bar{\mathbf{C}}))^2 - \text{tr}(\bar{\mathbf{C}}^2)\}$. The pseudo-invariants \bar{I}_4 and \bar{I}_6 are representative of preferred directions identified in the reference configuration by the unit vectors $\mathbf{a}_{0,1}$ and $\mathbf{a}_{0,2}$ such that $\bar{I}_4 = \bar{\mathbf{C}} : \mathbf{a}_{0,1} \otimes \mathbf{a}_{0,1}$ and $\bar{I}_6 = \bar{\mathbf{C}} : \mathbf{a}_{0,2} \otimes \mathbf{a}_{0,2}$. Here, the $:$ operator is the scalar product of two 2nd order tensors and \otimes is the dyadic operator. Note that \bar{I}_4 and \bar{I}_6

are the square of the stretch ratio of a line element in the preferred direction and are thus used in collagenous tissue to represent fiber deformations.

Individual models are specified by unique formulations of Ψ_{isotr} and Ψ_{aniso} . A common contemporary choice for these is the use of a neo-Hookean model to represent the isotropic response of the tissue $\Psi_{isotr}(\bar{I}_1) = \frac{\mu}{2}(\bar{I}_1 - 3)$ and a Holzapfel-Gasser-Ogden (HGO) representation of the fiber energy $\Psi_{aniso}(\bar{I}_k) = \frac{k_1}{2k_2} \exp\{k_2(\bar{I}_k - 1)^2\} - 1$, where $k = 4, 6$.

2.6.2 Viscoelastic constitutive modeling

There are three general methods for modeling relaxation (rate-dependent) behavior: linear viscoelasticity, quasi-linear viscoelasticity (QLV), and non-linear viscoelasticity. Linear viscoelasticity assumes a linear response to both the stress-strain relationship and the time-dependent behavior, and has been shown to be appropriate to describe the response of tissues at small sinusoidal strains [83]. As linear viscoelasticity is clearly inappropriate for use in the highly non-linear response of soft tissue, QLV is a reasonable way to separate the relaxation function into a nonlinear isochronal (strain dependent) portion and a time-based relaxation function wherein the shape of the relaxation curve is identical regardless of strain [84]. QLV has been shown to be appropriate for various soft tissues [85, 86]; however, it is theoretically not correct, as the relaxation function should be dependent on each the stress, deformation, and rate tensors [85]. In fact, fully non-linear relaxation formulations have repeatedly been shown to be more appropriate than QLV in various tissue [84, 85, 87, 88]. While non-linear relaxation

functions may be more physically appropriate, identifying the additional parameters is experimentally challenging [85], leading most researchers to resort to QLV formulations.

Relaxation in soft tissue exists on a continuous spectrum with rate-independent damping [85]. Accounting for a continuous relaxation spectrum is computationally expensive. Fortunately, the discretization of the relaxation spectrum into a series of exponentials with relaxation times spaced one decade apart does an adequate job of approximating a continuous relaxation spectrum [85, 86].

There are three primary families of viscoelastic constitutive models that are commonly used in contemporary soft tissue mechanics: multiplicative decomposition of deformation tensors, additive decomposition of free-energy equations, and Prony series acting on the stress rate. Prony series are often used in finite element (FE) models involving time-dependent material properties (e.g., [13, 89]) as they are easy to implement in FE packages [90, 91] and are relatively computationally inexpensive. Prony series are of the form

$$\mathbf{T}(t) = \int_0^t \left[M_\infty + \sum_i^n M_i \exp\left(\frac{-t+s}{\tau_i}\right) \right] \frac{\partial \mathbf{T}^e}{\partial s} ds$$

where \mathbf{T}^e is the infinite time response, τ_i are the relaxation time constants, M_i are scalars on the relaxation terms and affect the upper bound (instantaneous) of the tissue response, and t is the current time. M_∞ affects the long-term response but is often fixed at a value of 1 such that the infinite time response is equal to the hyperelastic prediction.

2.6.3 Inelastic constitutive modeling

Continuum damage mechanics is the most common framework by which inelasticity is modeled. Within this framework, some groups account for continuous softening [92-94]; however, most focus on discontinuous (Mullins-type) softening [21, 41, 95, 96]. A plethora of general model forms exist; however, the vast majority of published damage models can be categorized as an energy-penalty model or a plastic-strain model. Several models incorporate both energy penalties and plastic (residual) strain.

Almost all of the energy-penalty models can be traced back to the seminal work of Simo in 1987 [41] where he outlined the application of a reduction factor (first proposed in the infinite domain by Kachanov in 1958 [97]) to a hyperelastic model. This model, of form $\Psi(\mathbf{C}, D) = (1 - D)\Psi^0(\mathbf{C})$, simply reduces the stored energy of a general hyperelastic function $\Psi^0(\mathbf{C})$. Discontinuous damage parameter $D \in [0,1]$ generally evolves through an irreversible evolution function when an equivalent strain \mathcal{E}^s , defined by $\mathcal{E}^s := \sqrt{2\Psi^0(\mathbf{C}(s))}$, is equal to the maximum value \mathcal{E}^m , defined by

$$\mathcal{E}^m := \max_{s \in (-\infty, t)} \sqrt{2\Psi^0(\mathbf{C}(s))}.$$

Note that it is standard practice to state thermodynamic consistency of the preferred formulation by means of the Clausius-Duhem inequality $D_{int} = -\dot{\Psi} + \frac{1}{2}\mathbf{S}:\dot{\mathbf{C}} \geq 0$. It is further expected that the damage criteria ϕ_n are explicitly stated to be less than or equal to zero such that $\phi_n(\mathbf{C}, \mathcal{E}_n^m) = \sqrt{2\Psi^0(\mathbf{C}(s))} - \mathcal{E}_n^m \leq 0$.

If deformation is progressing at the damage surface $\mathcal{E}_n^s \cdot \phi_n = 0$, one must check that the deformation is traveling away from surface. With a normal defined as

$N_n = \partial \phi_i / \partial \mathbf{C}$, one can ensure that $N_n : \dot{\mathbf{C}} > 0$ at the damage surface before altering the damage variable. More concisely,

$$\dot{D}_n = \begin{cases} D'_n(\mathcal{E}_n) \dot{\mathcal{E}}_n, & \text{if } \phi_n = 0 \text{ and } N_n : \dot{\mathbf{C}} > 0 \\ 0 & \text{otherwise} \end{cases}$$

where rate of damage accumulation \dot{D}_n is defined by some function $D'_n(\mathcal{E}_n) = \partial D_n / \partial \mathcal{E}_n$ when all damage criteria are satisfied [98].

It is the choice of the modeler what form the hyperelastic function Ψ^0 takes, which term(s) the reduction factor $(1 - D)$ will be applied to, and what form the damage evolution function(s) will take. This is generally done iteratively, repeatedly checking model performance against experimental data prior to selecting an appropriate final model formulation.

Although elastic-plastic decomposition models are much less common than energy-penalty models in soft tissue, they are not rare. The multiplicative decomposition of the deformation gradient \mathbf{F} into elastic and plastic components $\mathbf{F} = \mathbf{F}^e \mathbf{F}^p$, as proposed by Kröner in 1959 [99], is the core of most plastic strain-based models. In this formulation, \mathbf{F}^p maps deformations into an intermediate zero load state, and \mathbf{F}^e maps the intermediate state to the final deformed configuration.

2.6.4 Visco-hyperelastic-plastic modeling

There are very few visco-hyperelastic-plastic models. Intriguingly, the first modern formulation of these models was included in the debut of modern finite non-linear hyperelastic-plastic damage modeling. Simo, in his pioneering paper on finite non-linear continuum damage theory [41], included formulations appropriate for viscoelasticity by additively decomposing the stress into equilibrium (elastic) and non-

equilibrium (viscoelastic) parts. This work inherently softens both the equilibrium and non-equilibrium components equally with the evolution of discontinuous softening parameters. The application of a single damage parameter equally affecting the viscous and elastic components of the free-energy equation, as pioneered by Simo, has been repeated in a vast majority of the subsequent formulations (i.e., [42, 71, 100-102]). Although these models all apply viscoelasticity to the plastically deformed tissue, they take various forms in applying hyperelasticity and plasticity, as discussed in previous sections of the present work.

2.7 High-rate damage mechanics in soft tissue

There is a paucity of studies on the effect of overstretch on subsequent changes to the viscoelastic properties of soft tissue. Panjabi *et al.* investigated the effect of high strain rate (1 s^{-1}) overstretch on the parameters of a Kelvin-Voigt standard linear model in rabbit anterior cruciate ligament (ACL) [103]. They found a substantial (approximately 50%) decrease in the serial spring and parallel dashpot parameters (although the change in the dashpot parameter was not statistically significant). Duenwald-Kuehl *et al.* also identified a substantial change in the viscoelastic properties of porcine flexor tendons following overstretch [104]. They noted that the overstretch affected the time-dependent properties, and specifically that the max stress and range of stress relaxation were decreased proportionally, indicating that the viscous and elastic properties were equally altered by overstretch. Kurz *et al.*, on the other hand, found that softening of the equilibrium and non-equilibrium stiffnesses of cartilage plugs progressed differently

depending on the rate of overstretch, with the non-equilibrium stiffness softening more aggressively following high strain rate damage [105].

CHAPTER 3

A STRAIN RATE-DEPENDENT CONSTITUTIVE MODEL FOR GÖTTINGEN

MINIPIG CEREBRAL ARTERIES

Noah Pearson

Department of Mechanical Engineering,
The University of Utah,
1495 E 100 S,
Salt Lake City, UT 84112
e-mail: noah.pearson@utah.edu

Gregory M. Boiczuk

Department of Biomedical Engineering,
The University of Utah,
36 S. Wasatch Drive,
Salt Lake City, UT 84112
e-mail: g.boiczuk@utah.edu

Vivek Bhaskar Kote

Department of Defense Biotechnology High
Performance Computing Software Applications
Institute,
Telemedicine and Advanced Technology
Research Center,
United States Army Medical Research and
Development Command,
Fort Detrick, MD 21702;
The Henry M. Jackson Foundation for the
Advancement of Military Medicine, Inc.,
6720A Rockledge Drive,
Bethesda, MD 20817
e-mail: vkote@bhsai.org

Aravind Sundaramurthy

Department of Defense Biotechnology High
Performance Computing Software Applications
Institute,
Telemedicine and Advanced Technology
Research Center,
United States Army Medical Research and
Development Command,
Fort Detrick, MD 21702;
The Henry M. Jackson Foundation for the
Advancement of Military Medicine, Inc.,
6720A Rockledge Drive,
Bethesda, MD 20817
e-mail: asundaramurthy@bhsai.org

Dhananjay Radhakrishnan Subramaniam

Department of Defense Biotechnology High
Performance Computing Software Applications
Institute,
Telemedicine and Advanced Technology
Research Center,
United States Army Medical Research and
Development Command,
Fort Detrick, MD 21702;
The Henry M. Jackson Foundation for the
Advancement of Military Medicine, Inc.,
6720A Rockledge Drive,
Bethesda, MD 20817
e-mail: dsubramaniam@bhsai.org

A Strain Rate-Dependent Constitutive Model for Göttingen Minipig Cerebral Arteries

Computational simulations of traumatic brain injury (TBI) are commonly used to advance understanding of the injury–pathology relationship, tissue damage thresholds, and design of protective equipment such as helmets. Both human and animal TBI models have developed substantially over recent decades, partially due to the inclusion of more detailed brain geometry and representation of tissues like cerebral blood vessels. Explicit incorporation of vessels dramatically affects local strain and enables researchers to investigate TBI-induced damage to the vasculature. While some studies have indicated that cerebral arteries are rate-dependent, no published experimentally based, rate-sensitive constitutive models of cerebral arteries exist. In this work, we characterize the mechanical properties of axially failed porcine arteries, both quasi-statically (0.01 s^{-1}) and at high rate ($>100\text{ s}^{-1}$), and propose a rate-sensitive model to fit the data. We find that the quasi-static and high-rate stress–stretch curves become significantly different ($p < 0.05$) above a stretch of 1.23. We additionally find a significant change in both failure stretch and stress as a result of strain rate. The stress–stretch curve is then modeled as a Holzapfel–Gasser–Ogden material, with a Prony series added to capture the effects of viscoelasticity. Ultimately, this paper demonstrates that rate dependence should be considered in the material properties of cerebral arteries undergoing high strain-rate deformations and provides a ready-to-use model for finite element implementation.
[DOI: 10.1115/1.4053796]

¹Corresponding author.

Manuscript received November 5, 2021; final manuscript received February 2, 2022; published online March 9, 2022. Assoc. Editor: David M. Pierce.

This work is in part a work of the U.S. Government. ASME disclaims all interest in the U.S. Government's contributions.

Jose E. Rubio

Department of Defense Biotechnology High
Performance Computing Software Applications
Institute,
Telemedicine and Advanced Technology
Research Center,
United States Army Medical Research and
Development Command,
Fort Detrick, MD 21702;
The Henry M. Jackson Foundation for the
Advancement of Military Medicine, Inc.,
6720A Rockledge Drive,
Bethesda, MD 20817
e-mail: jrubio@bhsai.org

Ginu Unnikrishnan

Department of Defense Biotechnology High
Performance Computing Software Applications
Institute,
Telemedicine and Advanced Technology
Research Center,
United States Army Medical Research and
Development Command,
Fort Detrick, MD 21702;
The Henry M. Jackson Foundation for the
Advancement of Military Medicine, Inc.,
6720A Rockledge Drive,
Bethesda, MD 20817
e-mail: gunnikrishnan@i-a-i.com

Jaques Reifman

Department of Defense Biotechnology High
Performance Computing Software Applications
Institute,
Telemedicine and Advanced Technology
Research Center,
United States Army Medical Research and
Development Command,
Fort Detrick, MD 21702
e-mail: jaques.reifman.civ@mail.mil

Kenneth Monson¹

Department of Biomedical Engineering,
The University of Utah,
1495 E 100 S,
Salt Lake City, UT 84112;
Department of Mechanical Engineering,
The University of Utah,
1495 E 100 S,
Salt Lake City, UT 84112
e-mail: ken.monson@mech.utah.edu

Introduction

Traumatic brain injury (TBI) is a condition affecting both civilian and military populations. Both human and animal models of TBI have been used for years to improve understanding of brain mechanics during TBI (e.g., Refs. [1–6]), providing insights that lead to a better understanding of the injury–pathology relationship [7], damage thresholds [8], and optimized protection devices, such as helmets [9]. Cerebral blood vessels have been explicitly modeled in finite element (FE) simulations of TBI with increasing frequency in the last several years [10–13]. While the utility of accounting for vessels to improve overall brain-strain predictions has been debated, it is clear that they can dramatically influence

local strains. Models that explicitly include vessels plainly also provide a platform to investigate mechanisms of TBI-induced damage to the vasculature [14].

Because TBI produces deformations over a range of strain rates, researchers typically represent brain tissue as rate-sensitive in TBI models, whether as viscoelastic [4–6,8–10], biphasic [15], or multiphasic [16]. However, no FE TBI model has used a rate-dependent constitutive model for vessels. This is partially a result of ambiguity as to whether or not blood vessels are rate-dependent (see Monson et al. [17] for a more detailed discussion of rate dependency in cerebral vessels) but is surely also due to the lack of a published rate-dependent constitutive model appropriate for the high strain rates associated with TBI [11]. As Bell et al. [18]

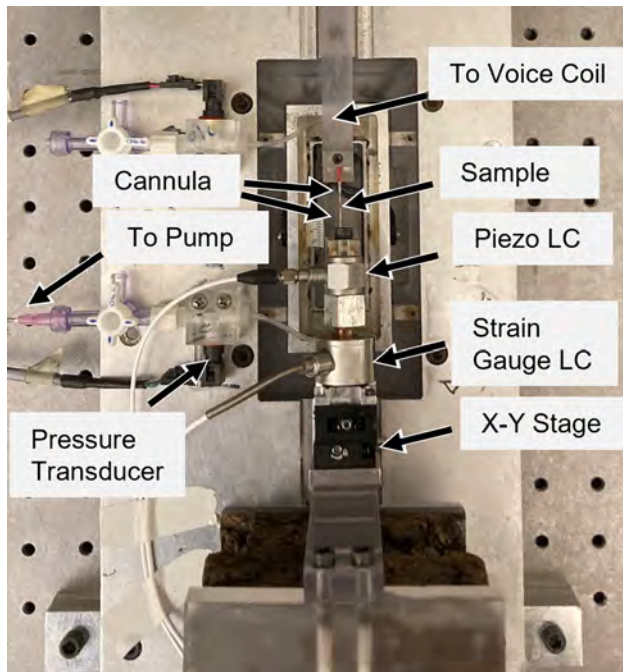


Fig. 1 Image of tester setup. The piezoelectric load cell provides instantaneous load data and was used for high strain rate measurements. The strain gage load cell provides a stable signal over long time frames and was used for all quasi-static measurements. Images were recorded through an overhead microscope (not pictured). For high rate deformations, a drop tower replaced the voice coil as explained in Ref. [18].

observed an approximately three-fold increase in cerebral artery failure stress between quasi-static (0.01 s^{-1}) and high rate ($>700 \text{ s}^{-1}$) groups, it is easy to imagine that neglecting rate stiffening could substantially affect the model predictions, especially in local regions proximal to arteries.

To facilitate the use of rate-dependent constitutive models of blood vessels in FE simulations of TBI, we demonstrate strain rate dependence of cerebral arteries from Göttingen minipigs and fit the data to a Holzapfel–Gasser–Ogden (HGO)-type model [19] coupled with a Prony series to capture the observed viscoelasticity. We anticipate that this work will help clarify the debate over the presence of rate stiffening in cerebral arteries and provide a model appropriate for implementation in FE models of TBI.

Materials and Methods

Overview. Nineteen quasi-static (0.01 s^{-1}) and 38 high strain rate (21 targeted at 150 s^{-1} and 17 targeted at 300 s^{-1}) samples were pulled axially to failure, with luminal pressure at either 80 or 120 mmHg. Stress–stretch curves were created from the collected data, and constitutive models were fit to these curves.

Tissue Acquisition and Preparation. Fifty-seven middle cerebral arteries (MCAs) were resected from 24 Göttingen minipigs. The minipigs were euthanized by Beuthanasia overdose under the approval of both the University of Utah Institutional Animal Care and Use Committee and the Animal Use and Review Committee at Ft. Detrick, MD. Immediately following death, the brain was removed and placed in phosphate-buffered saline (PBS). Arteries were then dissected from the surface of the brain, the attached pia-arachnoid complex tissue was removed, and any side branches were ligated with unwound 6-0 silk suture. Finally, rings were cut from both ends of each sample, and the cross section of the rings was imaged to provide reference wall dimensions.

Testing Apparatus. The testing device and protocol have been previously described [18]. In brief, arteries were mounted to size-matched cannulas and attached using 6-0 silk suture, with cyanoacrylate applied to tissue distal to the suture. Samples were submerged in a bath filled with calcium-free PBS to inhibit smooth muscle function. One cannula was mounted to a load cell assembly (Fig. 1) consisting of a piezoelectric load cell (208C01, PCB Piezotronics, Depew, NY) adjacent to the artery and a strain gage load cell (model 31 250 g, Honeywell, Golden Valley, MN) on the fixed end. The load cell assembly was attached to an X–Y stage used for aligning needles. The stage was, in turn, mounted on a cork isolation block that delayed mechanical noise produced in the high-rate tests until after the artery had failed. For quasi-static motions, the other cannula was attached to a voice coil linear actuator (AVM60-25, Motion Control Products, Bournemouth, UK) with a built-in encoder ($1 \mu\text{m}$ resolution) for monitoring displacement. Images were recorded at a sampling frequency of 3 Hz via a camera (PL-A741, Pixelink, Rochester, NY) mounted on a light microscope (2000 C, Carl Zeiss Microscopy, White Plains, NY). Luminal pressure was monitored with a pressure transducer (26PCDFM6G, Honeywell, Golden Valley, MN) located at each end of the vessel. Target pressures were maintained via a syringe pump operating on a closed-loop feedback controller for preconditioning, and then changed to a simple water (PBS) column at the desired pressure for the failure tests. Data were collected at a sampling frequency of 100 Hz on a Wheatstone bridge-specific data acquisition card (SCXI 1520, National Instruments, Austin, TX) and digitized with a scanning multiplexer (SCXI 1600, National Instruments).

The tester was reconfigured for high-rate tests after preconditioning the vessel. With the artery slightly buckled, the voice coil was replaced by a cable routed over a pulley and attached to a drop tower, as detailed previously [18]. A stop was placed against the vessel side of the sled and secured to the sled with masking tape. A steel ball was then dropped into a catchment attached to the cable, fracturing the tape and rapidly transferring ball momentum to the vessel. Images for the high-rate tests were recorded with a high frame-rate camera (Phantom Miro EX4, Vision Research, Perth, Australia) at 25 kHz, and displacement was monitored optically. Data collection was switched to a simultaneous sampling high sample-rate data acquisition card (PXI 6133, National Instruments) at 250 kHz.

Experimental Protocol. Vessels were first preconditioned by oscillating luminal pressure between 50 and 150 mmHg five times at a low axial stretch. The pressure cycles were then repeated at gradually increasing levels of axial stretch until changes in luminal pressure did not cause a change in axial force. This transition point was considered the *in vivo* stretch [20]. The vessel was finally preconditioned one additional time at a stretch of 1.10 times the *in vivo* length. Following preconditioning, vessels were buckled, set to a luminal pressure of 80 or 120 mmHg, then pulled to failure either quasi-statically (0.01 s^{-1}) or at high strain rate (150 or 300 s^{-1}). As bathwater interferes in both the image acquisition and the load signal, the bath was drained immediately before failure for the high-rate tests. Vessels were out of saline for no more than 30 s prior to failure.

Data Processing. While load signals were collected using both strain-gage and piezoelectric devices, data from the strain-gage load cell were used for all quasi-static motions as strain-gage load cells are more stable over long time periods. Because strain-gage load cells are mechanically excited at high strain rates, we used data from the piezoelectric load cell for all high-rate deformations. We have previously shown that the strain-gage load trace can be mathematically predicted from the piezoelectric load trace using a linear mass-spring-damper model [18].

Microspheres were applied to the artery surface to act as fiducial markers, but excessive motion of these markers relative to the tissue during high-rate tests led us to define stretch as the suture-to-suture stretch ratio. Outer diameter was identified at the same

location in each image frame, smoothed across five image frames, and then upsampled to match the data acquisition rate. Load data were filtered with a fourth-order Butterworth filter [21].

Mean Cauchy stress was calculated with the assumption of incompressibility and plane stress

$$T_\theta = p_i \left(\frac{d_i}{d_o - d_i} \right), \quad T_z = \frac{\lambda_z}{A} \left(F_z + \frac{\pi}{4} p_i d_i^2 \right), \quad T_r = 0 \quad (1)$$

where T_θ , T_z , and T_r are the circumferential, axial, and radial stresses, respectively, λ_z is the current axial stretch, A is the reference cross-sectional area, F_z is the axial force, p_i is the internal pressure, and d_i and d_o are the inner and outer diameter. d_i was calculated with the assumption of incompressibility.

Statistical Analysis. Two-way unbalanced analysis of variance was used to identify significant changes in failure stress and stretch due to differences in pressure and rate groups, making six individual groups. Inhomogeneous variance was identified using a Levene's test. Therefore, a Games-Howell posthoc test [22] was used for individual group comparisons. Analysis showed that neither the pressure groups nor the high-rate groups were statistically different, so the pressure groups were consolidated and the 150 and 300 s⁻¹ groups were combined, leaving two groups: quasi-static and high rate. Statistical significance between these two groups was calculated using a t-test with the Satterthwaite approximation used to account for different variances between groups. A p -value of 0.05 was used as the threshold of significance. A coefficient of determination (R^2 value) was calculated to quantify model performance [23]. This coefficient was identified for both the entire dataset (all sample tests) and for the average curves.

Constitutive Modeling. Previous work in our lab has shown cerebral arteries to be anisotropic [24,25]. As such, an HGO-type model [19], with a Prony series added to capture the viscoelastic response, was used to fit the data. The isothermal Helmholtz free-energy equation for the hyperelastic function was decomposed into dilatational (Ψ_{dil}) and isochoric (Ψ_{iso}) terms

$$\Psi(\mathbf{C}, \mathbf{a}_{0,1}) = \Psi_{\text{dil}}(J) + \Psi_{\text{iso}}(\bar{\mathbf{C}}, \mathbf{a}_{0,1}) \quad (2)$$

where \mathbf{C} is the right Cauchy–Green tensor, $\mathbf{a}_{0,1}$ is the reference fiber direction, J is the Jacobian of the deformation gradient, and the isochoric portion of the right Cauchy–Green tensor $\bar{\mathbf{C}}$ is calculated as $\bar{\mathbf{C}} = J^{-2/3} \mathbf{C}$. As incompressibility was enforced, J was set to one, and the dilatational stress was calculated using a Lagrange multiplier enforcing a radial stress of zero such that

$$\Psi_{\text{dil}} = -p(J - 1) \quad (3)$$

The isochoric strain energy was further decomposed into isotropic (Ψ_{isotr}) and anisotropic (Ψ_{aniso}) terms

$$\Psi_{\text{iso}} = \Psi_{\text{isotr}}(\bar{I}_1) + \Psi_{\text{aniso}}(\bar{I}_4, \mathbf{a}_{0,1}) \quad (4)$$

The isotropic response is represented by the Neo-Hookean model

$$\Psi_{\text{isotr}}(\bar{I}_1) = \frac{\mu}{2} (\bar{I}_1 - 3) \quad (5)$$

where μ is a constant and \bar{I}_1 represents the first invariant of $\bar{\mathbf{C}}$. The anisotropic response Ψ_{aniso} is represented by an exponential fiber stretch model. Here, we deviate from the standard HGO model in two notable ways. While Holzapfel et al. split the artery wall into adventitial and medial layers and then modeled each layer separately, we treat the artery as a single layer with a single, axially oriented fiber family representing the adventitial collagen believed to be responsible for axial stiffness. While not

histologically accurate, we represent only the adventitial collagen fibers because the model is intended to capture simple, primarily axial vessel deformations similar to those explored in the described experiments. As such, the anisotropic portion of the free-energy function is represented by

$$\Psi_{\text{aniso}}(\bar{I}_4) = \frac{k_1}{2k_2} \exp\{k_2(\bar{I}_4 - 1)^2\} - 1 \quad (6)$$

Invariant \bar{I}_4 is the isochoric fiber stretch value $\bar{I}_4 = \bar{\mathbf{C}} : \mathbf{A}_1$, where \mathbf{A}_1 is the structure tensor $\mathbf{A}_1 = \mathbf{a}_{0,1} \otimes \mathbf{a}_{0,1}$. $\mathbf{a}_{0,1}$ represents the reference fiber direction along the axis of the artery.

Cauchy stress for a general hyperelastic function is calculated by taking the derivative of the strain-energy function with respect to the deformation gradient such that

$$\mathbf{T} = J^{-1} \mathbf{F} \frac{\partial \Psi}{\partial \mathbf{F}} \quad (7)$$

When applied to the strain-energy function presented above, we arrive at an elastic Cauchy stress that is the summation of each decomposed component of the strain-energy function such that

$$\mathbf{T} = \mathbf{T}_{\text{dil}} + \mathbf{T}_{\text{isotr}} + \mathbf{T}_{\text{aniso}} \quad (8)$$

where

$$\mathbf{T}_{\text{dil}} = -p \mathbf{I} \quad (9)$$

$$\mathbf{T}_{\text{isotr}} = \mu J^{-1} \text{dev}(\bar{\mathbf{b}}) \quad (10)$$

and

$$\mathbf{T}_{\text{aniso}} = 2k_1 J^{-1} (\bar{I}_4 - 1) \exp[k_2 (\bar{I}_4 - 1)^2] \text{dev}(\bar{\mathbf{a}}_{0,1} \otimes \bar{\mathbf{a}}_{0,1}) \quad (11)$$

Here, the $\text{dev}()$ operator refers to the deviatoric operator, defined such that $\text{dev}(\mathbf{A}) = \mathbf{A} - 1/3 \text{tr}(\mathbf{A}) \mathbf{I}$, \mathbf{I} is the identity tensor, and $\bar{\mathbf{b}}$ is the isochoric portion of the left Cauchy–Green tensor. For a more detailed description of the stress derivation, the reader is referred to Ref. [26].

A Prony series was chosen to model the rate dependence of the arteries. Prony series are commonly the model of choice to represent viscoelasticity in finite element packages [27,28]. Furthermore, many FE simulations of TBI use a Prony series to account for viscoelasticity (e.g., Refs. [12] and [29]). The chosen formulation for the Prony series [8,28,30,31] outputs a final stress \mathbf{T} as a function of the elastic stress \mathbf{T}^e and the time t , defined as

$$\mathbf{T}(t) = \int_0^t \left[M_\infty + \sum_i^n M_i \exp\left(-\frac{-t+s}{\tau_i}\right) \right] \frac{\partial \mathbf{T}^e}{\partial s} ds \quad (12)$$

Here, M_∞ is fixed at 1 such that \mathbf{T}^e is the long-term elastic response, while scalars M_i and time constants τ_i are fit parameters. In this work, we first evaluate the model with a single Prony term. To explore the effect of a broader relaxation spectrum, we then consider a three-term model with additional τ terms fixed an order of magnitude higher and lower than the τ term optimized in the one-term model. The choice of a three-term model (rather than two) allows for a balanced addition of time constants around the initial one-term fit.

Model Fitting. Quasi-static data were fit to the hyperelastic function. The parameters from this fit were then used to seed hyperelastic parameters when the entire dataset was fit to the viscoelastic model. The data were fit using MATLAB's *fmincon* algorithm minimizing the Manhattan distance (L1 norm) between the model prediction and the experimental results for both the

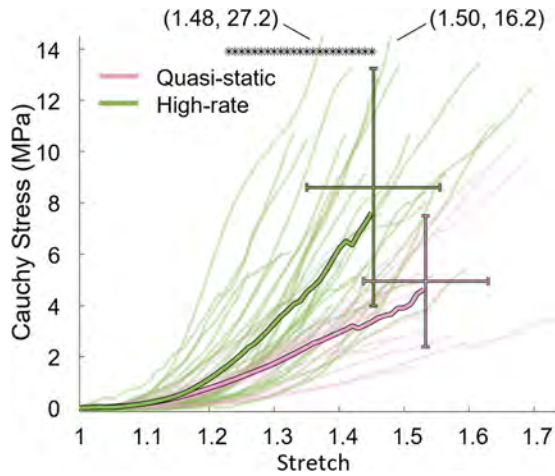


Fig. 2 All axial experimental traces overlaid with average curves (bold). Quasi-static data are presented in pink and high-rate data in green. Asterisks (*) over the data are used to identify stretch bins (spaced at 0.01 increments) at which the experimental curves are significantly different ($p < 0.05$). Average failure stretch and stress are shown at the cross of the error bars. Error bars represent standard deviation of stretch (horizontal) and stress (vertical). Failure coordinates (stretch, stress) are identified for two curves that extend beyond the selected axis limits. Average curves become erratic once they extend past the failure stretch of some individual arteries.

circumferential and axial directions. All samples were fit concurrently.

Results

The resulting stress–stretch curves exhibit the highly nonlinear response typical of arteries (Fig. 2). Similar to Bell et al. [18], we observed more scatter in the high-rate data than in the quasi-static data. Visually, there is a clear trend of rate dependence in the data, although there is overlap between quasi-static and high-rate tests.

No difference ($p < 0.05$) in failure stretch or failure stress was found between the 80 and 120 mmHg groups for any of the quasi-static, 150, or 300 s^{-1} groups. As such, data from both pressures were combined into a single group at each strain rate for subsequent analysis. Similarly, no significant difference was identified between the 150 and 300 s^{-1} groups, so these data were also combined to create one high-rate group.

The quasi-static stress–stretch curves show generally lower stresses than the high-rate curves, as seen in Fig. 2. Notably, the high-rate average curve does not significantly ($p < 0.05$) separate from the quasi-static curve until a stretch of 1.23. High-rate failure stress (8.61 ± 4.63 MPa; mean \pm std) was statistically greater than quasi-static failure stress (4.94 ± 2.56 MPa; $p = 0.0005$). High-rate failure stretch (1.45 ± 0.102) was significantly lower than that of the quasi-static group (1.53 ± 0.096 ; $p = 0.007$).

While we largely achieved the targeted high rates, strain rate increased throughout the tests (Fig. 3). The 150 s^{-1} group had a strain rate (mean \pm std) of $103 \pm 50.4 s^{-1}$ at the start of loading ($\lambda = 1$) and a maximum strain rate of $317 \pm 53.5 s^{-1}$, while the 300 s^{-1} group had corresponding strain rates of 275 ± 118 and $596 \pm 135 s^{-1}$ (Fig. 3).

The one-term Prony series model provides a reasonably accurate representation of the data, including capturing strain rate stiffening for the two different rate groups (Fig. 4). However, it overpredicts stresses at low values of stretch and also slightly underpredicts stress and stiffness at high stretches for high-rate deformations. The fit model provides an R^2 of 0.584 when evaluating variance of the entire dataset but has an R^2 of 0.921 when evaluating the amount of explained variance in the average quasi-static and high-rate curves.

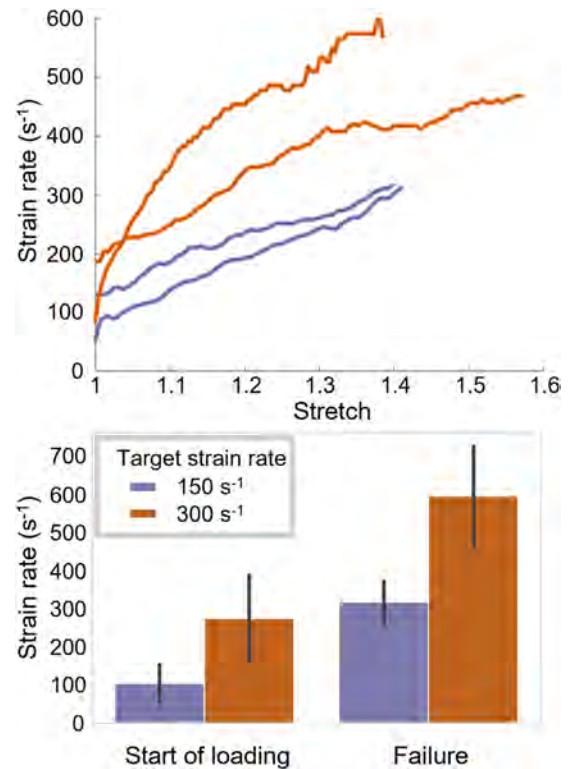


Fig. 3 Representative data for four arteries (top) demonstrate increasing strain rates throughout the deformation; two traces for each rate are shown to provide a sense for observed variation. Bar charts (mean \pm std) of the strain rate at the onset of loading and the maximum strain rate achieved (bottom) define strain rate distribution. Infinitesimal strain was used to determine strain rate.

Values of the hyperelastic (rate-insensitive) model parameters fit to the quasi-static data are somewhat similar to those identified when fitting all data to the Prony series (Table 1), with the neo-Hookean term μ nearly identical, and the fiber-stress scalar k_1 different by approximately a factor of two. Interestingly, the three-term Prony series converged to the same parameters as the one-term Prony series, with the scale on the two additional time constants approaching zero. As a result, it is not included in the plot.

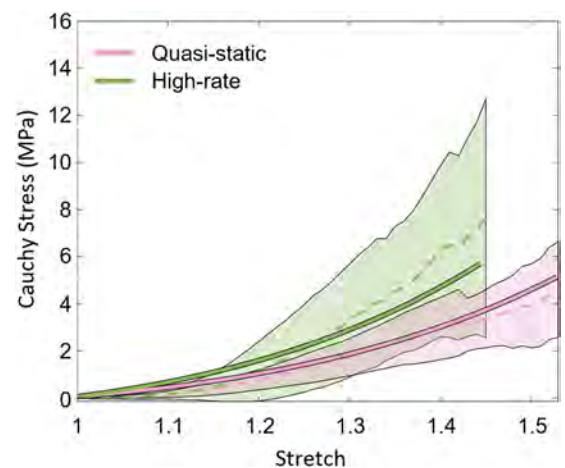


Fig. 4 Quasi-static and high-rate model predictions (bold) overlaid on all axial experimental data (dashed). Shaded regions represent standard deviation.

Table 1 Model parameters for constitutive models fit to the experimental data

Parameters	Hyperelastic fit	One-term Prony	Three-term Prony
μ (kPa)	70.6	71.0	71.0
k_1 (kPa)	352	741	741
k_2	5.75×10^{-3}	4.16×10^{-2}	4.16×10^{-2}
M_∞		1	1
M_1		0.573	4.08×10^{-11}
τ_1 (s)		4.02×10^{-2}	4.02×10^{-3}
M_2			0.573
τ_2 (s)			4.02×10^{-2}
M_3			4.95×10^{-11}
τ_3 (s)			0.402
L1 error (MPa)	241	79.9	79.9

The “hyperelastic fit” was fit exclusively to quasi-static data, whereas the models with Prony series were fit to all data. Notice that the three-term Prony model fit is equivalent to the one-term Prony fit as evidenced by M_1 and M_3 approaching zero.

Discussion

The objectives of this paper were to evaluate the rate dependence of Göttingen minipig cerebral arteries and to present a constitutive model that accurately simulates their response. Our results show a clear trend of rate stiffening, with statistically significant strain rate dependence of stress above a stretch of 1.23 and of both the failure stretch and failure stress values. With the experimental conclusion that cerebral arteries are strain rate sensitive, we modeled the experimental data as an HGO-type model with a one-term Prony series that provides a reasonably representative prediction of the data.

Experiment. The identified rate-dependent difference in failure stress supports the results found by Bell et al. [18] in rat MCAs, yet contrasts with the findings of Chalupnik et al. [32] and Monson et al. [33] in human cerebral arteries. We also find a rate-dependent difference in failure stretch, which contrasts with our previous work [18] reporting no change in the failure stretch of rat middle cerebral arteries over five orders of magnitude of strain rate; reasons for the dissimilar findings are unknown. From a damage perspective, the identified change in failure stretch is notable as it indicates that a stretch-based damage model that is insensitive to strain rate, such as that used by Marino et al. [34], may not be appropriate for high-rate deformations.

The identification of rate dependence only above a stretch of 1.23 is interesting. While reasons for this stretch threshold are currently unknown, we don’t believe it is necessarily the result of inherent strain dependence in rate stiffening. Rate-dependent changes in stress are determined by integrating rate-stiffened responses over deformation, thus leading to smaller changes in stress between rate groups at lower stretch values. Combined with the inherently worse signal-to-noise ratio of the load cells at lower loads, this integration of stiffness may lead to the observed viscoelastic threshold. As a result, our observation could be consistent with any mechanism of rate stiffening active over the full deformation range of the tissue.

The presented data span roughly four orders of magnitude of strain rate, investigating possible differences between quasi-static tests and two distinct groups of high-rate data (150 and 300 s^{-1} targets). We found a significant difference between quasi-static and high-rate groups, yet we did not find a difference between the 150 and 300 s^{-1} groups. While this indicates little change in stress due to fluctuations in strain rate at high strain rates, the nature of the progression of rate-stiffening between 0.01 and 100 s^{-1} remains undefined. Although strain rates of cerebral vessels in TBI are largely undefined, brain tissue rates are reported to occur within this unexplored range (e.g., Hardy et al. [35] found peak strain rates in the range 6.9–146.5 s^{-1} in cadaveric human heads).

As a result, it is critical that future work define vessel response at these intermediate rates.

The present experiment was setup to emphasize axial deformation, since we hypothesize that arteries are primarily loaded axially during TBI [17]. While we tested arteries at luminal pressures corresponding to diastolic and systolic pressures, we did not conduct large deformation biaxial tests. These tests would clearly be needed to furnish a model appropriate to describe large biaxial or circumferential deformations. While we focus here on axial deformations, recent TBI modeling work predicts that vessels experience significant deformations in both the axial and circumferential directions [36], so future research should focus on accounting for both.

It should be noted that experimental calculation of stress and strain in this work is limited to mean wall stress. Furthermore, we assume a biaxial stress state, resulting in a radial stress of zero throughout the specimen. Although this is common for thin-walled pressure vessels, it results in a physically impossible radial stress of zero at the inner wall of the artery. These assumptions mean that predictions of transmural stress variations using the presented model are not validated.

Another limitation related to large deformations is that the radial stretch was not monitored. It is experimentally challenging to measure radial stretch in small cerebral arteries, yet these data are necessary to evaluate the appropriateness of the assumption of incompressibility. Previous studies in our lab on both human [24] and rat [18] cerebral arteries suggested that the incompressibility assumption does not hold at large deformations (by virtue of physically invalid predictions of internal diameter). While we did not find such volume inversion in this study, further research is needed to address the assumption of incompressibility in large deformations of cerebral arteries.

Lastly, we did not perform a histological examination of collagen fibers. A more complete experimental dataset would include reference fiber directions for the medial fibers and dispersion parameters for all fibers. These data will promote more microstructurally motivated constitutive models and likely aid in developing microstructurally motivated damage models.

Model. The presented model is fit up to the failure point of each sample. It does not, however, model the failure itself, nor does it simulate any damage prior to failure. The appropriateness of the model for use at large deformations implies that it is acceptable for use in FE models of TBI, including severe TBI where the chance of hemorrhage is high. Furthermore, while Yu et al. applied a viscoelastic model to cerebral arteries [37], ours is the first such model fit to experimental data that accounts for rate stiffening, an important feature given that we have shown the failure stress to increase by approximately 75% during high-rate deformations.

We chose an HGO-type model for the hyperelastic portion of the presented constitutive model due to its implicit representation of the histological structure of the arterial wall (e.g., collagen fibers). However, we only accounted for the axially oriented adventitial fibers due to the axially dominant nature of our loading protocol. This approach adequately represents our data but leaves the definition of vessel response to large circumferential loading, resisted by the circumferentially oriented medial fibers, for later investigation. It must be pointed out that by neglecting the helical collagen fibers in the media, the presented model is ill-equipped to represent supraphysiologic loading in the circumferential direction, such as occurs in balloon angioplasty. Additionally, modeling collagen fiber dispersion has repeatedly been shown to improve model behavior, with increased dispersion associated with increased stiffness of the material [38]. Neglecting dispersion in the present model may alter the progression of stiffening. As a result of these limitations, it should be clear that the current model’s application is limited to applications where the deformations are primarily axial.

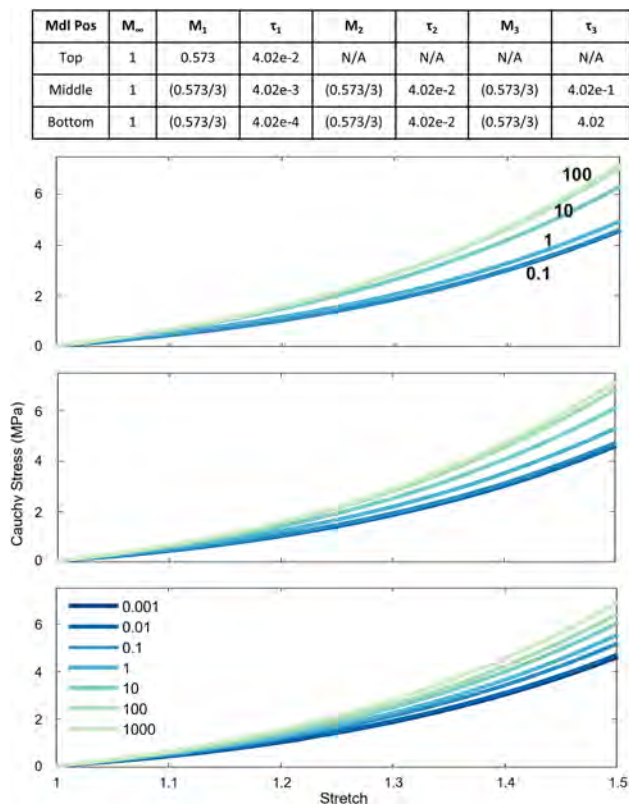


Fig. 5 Stress–stretch curves corresponding to various models applied to strain rates ranging from 0.001 to 1000 s^{-1} . Top: one-term Prony series fit to present data. Middle: hypothetical three-term Prony series with M_i set to $1/3 M_i$ in the one-term model to preserve the upper bound of model stress. τ_i are set one order of magnitude apart centered on the τ_1 fit in the one-term model. Bottom: Hypothetical three-term model with τ_i set two orders of magnitude apart. The fit model is most sensitive to strain rate between 1 and 10 s^{-1} , whereas increasing the number and dispersion of the Prony terms allows model sensitivity to strain rate to progress more evenly.

We targeted strain rates of 150 and 300 s^{-1} for the high-rate tests. We buckled the vessel and accelerated the fixturing as quickly as possible to obtain these high rates. Unfortunately, the acceleration was not complete by the time the vessel reached its reference length. Although we could not achieve a constant strain rate, the Prony series naturally accounts for the increasing strain rates during the fitting process, since it acts on the time derivative of stress. That said, the lower end of the stress–stretch curve is fit to a lower strain rate than the upper end of the curve, limiting our ability to infer strain dependent viscoelasticity.

Many modeling groups prefer to use a one-term Prony series for computational simplicity. In contrast, we explored higher term Prony series with additional time constants applied a decade above and below the optimized one-term fit to evaluate if there is a better fit with our data. We found that the optimization process set the scalars on the additional Prony terms to zero, indicating that a one-term Prony series is the most appropriate fit for our data. The single time constant contrasts with the often discretized [30] continuous spectrum of relaxation that has been used as a complete description of tissue viscoelasticity for many years [39].

To further explore the utility of the higher-order Prony series, we compare our model to variations with broader relaxation spectra (Fig. 5). We consider a broader range of strain rates (0.001–1000 s^{-1}) than was explored in our experiments (0.01–300 s^{-1}). It should be clear that this extended version of the model is not validated for use, but this exercise reveals some interesting model characteristics. In particular, there is no discernable change in the predicted behavior between 0.001 and 0.1 s^{-1}

or, similarly, between 100 and 1000 s^{-1} , using the model with the converged parameters reported in Table 1 (top plot). As a result, the model is most sensitive to strain rate between 1 and 10 s^{-1} . In contrast, Prony series variations with the same lower and upper bounds, but with larger ranges of time constants (middle and bottom plots), demonstrate broader, more evenly distributed rate sensitivity.

Interestingly, each presented model variation captures the general rate dependence observed in our experimental data. However, we do not currently know how rate dependence progresses between the quasi-static and 150–300 s^{-1} groups reported in this paper. It is also notable that there is no predicted strain rate sensitivity above 100 s^{-1} in the fit version of the model (top), potentially explaining the lack of observed difference between the 150 and 300 s^{-1} experimental groups. Fung’s [39] presentation of quasi-linear viscoelasticity postulates low and high thresholds of rate sensitivity, below and above which tissue properties are not dependent on strain rate, so it may be that the high threshold of sensitivity for this tissue is approximately 100 s^{-1} . Alternatively, as suggested by the third model (bottom), the order of magnitude of the 150 and 300 s^{-1} strain rates may be too similar to discern any rate-dependent changes in failure stress even if the upper bound of rate sensitivity is above the rates presently tested. In any case, it is clear that the inclusion of more time constants may be needed to accurately model cerebral vessel rate dependence once experimental data become available within this intermediate range.

Conclusion

This work demonstrates that porcine cerebral arteries are strain rate sensitive across the strain rates predicted in TBI. Additionally, we provide the first experimentally based visco-hyperelastic constitutive model of cerebral arteries ready to be applied to FE models of TBI. This model is fit up to failure, making it appropriate for investigating axially induced damage mechanisms in cerebral arteries as a result of TBI.

Funding Data

- U.S. Department of Defense (DoD) (Funder ID: 10.13039/100000005).
- Defense Health Program managed by the U.S. Army Military Operational Medicine Research Program Area Directorate (Fort Detrick, MD) (Funder ID: 10.13039/100000090).
- The Henry M. Jackson Foundation for the Advancement of Military Medicine (HJF), partially funded U.S. Army Medical Research and Development Command (Contract No. W81XWH-17-2-0008; Funder ID: 10.13039/100016156).
- National Science Foundation (NSF) (Award No. 2027367; Funder ID: 10.13039/100000147).

Conflict of Interest

The opinions or assertions contained herein are the private views of the authors and are not to be construed as official or reflecting the views of the United States (U.S.) Army, the U.S. Department of Defense (DoD), or The Henry M. Jackson Foundation for the Advancement of Military Medicine, Inc. (HJF). Any citations of commercial organizations and trade names in this report do not constitute an official U.S. Army, DoD, or HJF endorsement or approval of the products or services. This paper has been approved for public release with unlimited distribution.

References

- [1] Hayashi, T., 1970, “Brain Shear Theory of Head Injury Due to Rotational Impact,” *J. Fac. Eng. Univ. Tokyo*, **30**, pp. 307–313.
- [2] Shugar, T. A., Asce, A. M., and Katona, M. G., 1975, “Development of Finite Element Head Injury Model,” *J. Eng. Mech. Div.*, **101**(3), pp. 223–239.

- [3] Ruan, J. S., Khalil, T., and King, A. I., 1994, "Dynamic Response of the Human Head to Impact by Three-Dimensional Finite Element Analysis," *ASME J. Biomech. Eng.*, **116**(1), pp. 44–50.
- [4] Mao, H., Zhang, L., Jiang, B., Genthikatti, V. V., Jin, X., Zhu, F., Makwana, R., Gill, A., Jandir, G., Singh, A., and Yang, K. H., 2013, "Development of a Finite Element Human Head Model Partially Validated With Thirty Five Experimental Cases," *ASME J. Biomech. Eng.*, **135**(11), p. 111002.
- [5] Kleiven, S., 2003, "Influence of Impact Direction on the Human Head in Prediction of Subdural Hematoma," *J. Neurotrauma*, **20**(4), pp. 365–379.
- [6] Zhao, W., and Ji, S., 2019, "White Matter Anisotropy for Impact Simulation and Response Sampling in Traumatic Brain Injury," *J. Neurotrauma*, **36**(2), pp. 250–263.
- [7] Goriely, A., Geers, M. G., Holzapfel, G. A., Jayamohan, J., Jerusalem, A., Sivaloganathan, S., Squier, W., van Dommelen, J. A., Waters, S., and Kuhl, E., 2015, "Mechanics of the Brain: Perspectives, Challenges, and Opportunities," *Biomech. Model. Mechanobiol.*, **14**(5), pp. 931–965.
- [8] Cloots, R. J., van Dommelen, J. A., Kleiven, S., and Geers, M. G., 2013, "Multi-Scale Mechanics of Traumatic Brain Injury: Predicting Axonal Strains From Head Loads," *Biomech. Model. Mechanobiol.*, **12**(1), pp. 137–150.
- [9] Zhang, L., Makwana, R., and Sharma, S., 2013, "Brain Response to Primary Blast Wave Using Validated Finite Element Models of Human Head and Advanced Combat Helmet," *Front. Neurol.*, **4**, p. 88.
- [10] Zhang, L., Bae, J., Hardy, W. N., Monson, K. L., Manley, G. T., Goldsmith, W., Yang, K. H., and King, A. I., 2002, "Computational Study of the Contribution of the Vasculature on the Dynamic Response of the Brain," *Stapp Car Crash J.*, **46**, pp. 145–164.
- [11] Hua, Y., Lin, S., and Gu, L., 2015, "Relevance of Blood Vessel Networks in Blast-Induced Traumatic Brain Injury," *Comput. Math. Methods Med.*, **2015**, pp. 1–8.
- [12] Unnikrishnan, G., Mao, H., Sundaramurthy, A., Bell, E. D., Yeoh, S., Monson, K., and Reifman, J., 2019, "A 3-D Rat Brain Model for Blast-Wave Exposure: Effects of Brain Vasculature and Material Properties," *Ann. Biomed. Eng.*, **47**(9), pp. 2033–2044.
- [13] Zhao, W., and Ji, S., 2020, "Incorporation of Vasculature in a Head Injury Model Lowers Local Mechanical Strains in Dynamic Impact," *J. Biomech.*, **104**, p. 109732.
- [14] Farajzadeh Khosroshahi, S., Yin, X., C. K. D., McGarry, A., Yanez Lopez, M., Baxan, N., Sharp, D. J., Sastre, M., and Ghajari, M., 2021, "Multiscale Modelling of Cerebrovascular Injury Reveals the Role of Vascular Anatomy and Parenchymal Shear Stresses," *Sci. Rep.*, **11**(1), p. 12927.
- [15] Hosseini-Farid, M., Ramzanpour, M., McLean, J., Ziejewski, M., and Karami, G., 2020, "A Poro-Hyper-Viscoelastic Rate-Dependent Constitutive Modeling for the Analysis of Brain Tissues," *J. Mech. Behav. Biomed. Mater.*, **102**, p. 103475.
- [16] Lang, G. E., Vella, D., Waters, S. L., and Goriely, A., 2015, "Propagation of Damage in Brain Tissue: Coupling the Mechanics of Oedema and Oxygen Delivery," *Biomech. Model. Mechanobiol.*, **14**(6), pp. 1197–1216.
- [17] Monson, K. L., Converse, M. I., and Manley, G. T., 2019, "Cerebral Blood Vessel Damage in Traumatic Brain Injury," *Clin. Biomech.*, **64**, pp. 98–113.
- [18] Bell, E. D., Converse, M., Mao, H., Unnikrishnan, G., Reifman, J., and Monson, K. L., 2018, "Material Properties of Rat Middle Cerebral Arteries at High Strain Rates," *ASME J. Biomech. Eng.*, **140**(7), p. 071004.
- [19] Holzapfel, G. A., Gasser, T. C., and Ogden, R. W., 2000, "A New Constitutive Framework for Arterial Wall Mechanics and a Comparative Study of Material Models," *J. Elast.*, **61**(1/3), pp. 1–48.
- [20] Weiszacker, H. W., Lambert, H., and Pascale, K., 1983, "Analysis of the Passive Mechanical Properties of Rat Carotid Arteries," *J. Biomech.*, **16**(9), pp. 703–715.
- [21] Comm, S. T. I. S., 1995, *Instrumentation for Impact Test - Part 1 - Electronic Instrumentation*, SAE International, Warrendale, PA.
- [22] Megevand, P., 2021, "*games_howell*," GitHub, Geneva, Switzerland.
- [23] Budday, S., Sommer, G., Holzapfel, G. A., Steinmann, P., and Kuhl, E., 2017, "Viscoelastic Parameter Identification of Human Brain Tissue," *J. Mech. Behav. Biomed. Mater.*, **74**, pp. 463–476.
- [24] Monson, K. L., Barbaro, N. M., and Manley, G. T., 2008, "Biaxial Response of Passive Human Cerebral Arteries," *Ann. Biomed. Eng.*, **36**(12), pp. 2028–2041.
- [25] Bell, E. D., Kunjir, R. S., and Monson, K. L., 2013, "Biaxial and Failure Properties of Passive Rat Middle Cerebral Arteries," *J. Biomech.*, **46**(1), pp. 91–96.
- [26] Holzapfel, G., 2000, *Nonlinear Solid Mechanics: A Continuum Approach for Engineering*, Wiley, Chichester, UK.
- [27] Dassault Systèmes, 2009, "Abaqus Analysis User's Manual," Dassault Systèmes, Vélizy-Villacoublay, France, accessed Dec. 14, 2021, <http://130.149.89.49:2080/v6.9ef/books/usb/default.htm?startat=pt05ch19s07abm12.html>
- [28] Maas, S., Herron M., Weiss J., and Ateshian G., 2021, "FEBio Theory Manual," FEBio Software Suite, accessed Dec. 14, 2021, https://help.febio.org/FEBio-Theory/FEBio_tm_3-4-Section-5.4.html
- [29] Ji, S., Zhao, W., Ford, J. C., Beckwith, J. G., Bolander, R. P., Greenwald, R. M., Flashman, L. A., Paulsen, K. D., and McAllister, T. W., 2015, "Group-Wise Evaluation and Comparison of White Matter Fiber Strain and Maximum Principal Strain in Sports-Related Concussion," *J. Neurotrauma*, **32**(7), pp. 441–454.
- [30] Puso, M. A., and Weiss, J. A., 1998, "Finite Element Implementation of Anisotropic Quasi-Linear Viscoelasticity Using a Discrete Spectrum," *ASME J. Biomech. Eng.*, **120**(1), pp. 62–70.
- [31] Kraus, M. A., Schuster, M., Kuntsche, J., Siebert, G., and Schneider, J., 2017, "Parameter Identification Methods for Visco- and Hyperelastic Material Models," *Glass Struct. Eng.*, **2**(2), pp. 147–167.
- [32] Chalupnik, J. D., Daly, C. H., and Merchant, H. C., 1971, *Material Properties of Cerebral Blood Vessels*, University of Washington, Seattle, Final Report Contract No. NIH-69-2232.
- [33] Monson, K. L., Goldsmith, W., Barbaro, N. M., and Manley, G. T., 2003, "Axial Mechanical Properties of Fresh Human Cerebral Blood Vessels," *ASME J. Biomech. Eng.*, **125**(2), pp. 288–294.
- [34] Marino, M., Converse, M. I., Monson, K. L., and Wriggers, P., 2019, "Molecular-Level Collagen Damage Explains Softening and Failure of Arterial Tissues: A Quantitative Interpretation of CHP Data With a Novel Elastodamage Model," *J. Mech. Behav. Biomed. Mater.*, **97**, pp. 254–271.
- [35] Hardy, W. N., Mason, M. J., Foster, C. D., Shah, C. S., Kopacz, J. M., Yang, K. H., King, A. I., Bishop, J., Bey, M., Anderst, W., and Tashman, S., 2007, "A Study of the Response of the Human Cadaver Head to Impact," *Stapp Car Crash J.*, **51**, pp. 17–80.
- [36] Zhao, W., and Ji, S., 2022, "Cerebral Vascular Strains in Dynamic Head Impact Using an Upgraded Model With Brain Material Property Heterogeneity," *J. Mech. Behav. Biomed. Mater.*, **126**, p. 104967.
- [37] Yu, Y., Perdikaris, P., and Karniadakis, G. E., 2016, "Fractional Modeling of Viscoelasticity in 3D Cerebral Arteries and Aneurysms," *J. Comput. Phys.*, **323**, pp. 219–242.
- [38] Gasser, T. C., Ogden, R. W., and Holzapfel, G. A., 2006, "Hyperelastic Modelling of Arterial Layers With Distributed Collagen Fibre Orientations," *J. R. Soc. Interface*, **3**(6), pp. 15–35.
- [39] Fung, Y.-C., 1993, *Biomechanics: Mechanical Properties of Living Tissues*, Springer-Verlag, New York.

CHAPTER 4

MOLECULAR-LEVEL COLLAGEN DAMAGE IS STRAIN RATE DEPENDENT IN CEREBRAL ARTERIES STRETCHED TO FAILURE

**Noah Pearson (Co-first author), William J. Anderl (Co-first author), Matthew I.
Converse, S. Michael Yu, Kenneth L. Monson**

Notes

Will and I coauthored this work. Will lead the development of the methods evaluation in the paper, with the exception of the hydroxyproline assay and the new threshold definition, which I handled. Will was responsible for all discussions on the methods development. I tested the vessels, developed the new threshold definition based on control variance, and wrote all discussions on the implications of the results pertaining to the ECM. This work is currently in review for publication.

Abstract

While soft tissues are commonly damaged during various mechanical loadings, the manifestation of this damage at the microstructural level is not fully understood. Specifically, while rate-induced stiffening has been previously observed in cerebral arteries, associated changes in microstructural damage patterns following gross tissue

failure at high rates is largely not understood. In this study, we deformed porcine middle cerebral arteries to failure at 0.01 and $>150 \text{ s}^{-1}$ followed by probing for denatured tropocollagen using collagen hybridizing peptide (CHP). We found that collagen fibrils aligned with the loading direction experience less tropocollagen denaturation following high-rate failure than quasi-static failure. Furthermore, there was evidence of tropocollagen denaturation in fibrils transversely aligned to the loading axis at both rates, which, to our knowledge, is the first observation of collagen fibril damage due to transverse loading. These results indicate that strain rate is an important factor to consider when studying mechanically induced damage, and that fiber stretch may need to be reconsidered as a primary damage parameter in microstructurally informed continuum damage models due to the evidence of transverse damage.

1 Introduction

1.1 Constituent Damage in Arteries

Cerebral arteries play a critical role in sustaining life, as they are responsible for continuously distributing nutrients to the brain. While arteries are highly durable tissue, they are commonly damaged through trauma, such as traumatic brain injury (TBI) [2, 3], as well as by surgical procedures such as angioplasty [4]. Vessel injury has been widely studied and includes investigations of gross tissue failure and hemorrhage [24, 25], cellular dysfunction [26], and injury to the extra-cellular matrix (ECM) [20-22]. Furthermore, persistent changes to the mechanical response of arteries subsequent to overstretch have been reported following both circumferential and axial loading [39, 45, 106]. Much of this research aims to associate ECM damage with changes to the

mechanical response of the tissue [38, 43, 53, 54, 94], and to thus allow a better understanding of the implications of injury, angioplasty, and even remodeling of aneurysms [15, 24].

1.2 Rate Dependence and Microstructure

Many soft tissues, including arteries, are strain-rate sensitive. This rate sensitivity implies that when the material is deformed sufficiently slowly, the tissue's internal microstructure can freely reorganize to achieve the lowest internal energy configuration for the current deformation. The material thus constantly dissipates energy and only stores the absolute minimum energy at truly quasi-static strain rates. However, at high strain rates, the molecules cannot reorganize quickly enough to reach the minimum energy state for the current stretch. As stiffness is the second derivative of this strain energy with respect to strain, the inability of these tissues to reorganize is manifest as rate-dependent stiffening, such that higher strain rates produce higher stresses at a given level of stretch. There is some disagreement among researchers regarding the rate dependence of arteries [28-30, 78, 80-82, 107], perhaps due to different animal species and vessel types.

Given the observed rate-induced changes to microstructural energy dissipation in arteries, we anticipate an associated change in microstructural damage patterns, similar to that discussed in the broader soft tissue literature. Willet et al. observed a rate-dependent change in the binding rate of trypsin in tendon [31] that they attributed to the imposed strain rate being too high for intermolecular sliding, limiting the number of sites available for proteolysis. Continuing this work, Chambers et al. identified a strain rate dependence

of ultrastructural damage in bovine digital tendons between 1 and 10% s⁻¹ [33]. As arteries are often deformed to failure and bleed in TBI, we can assume that other intact vessels are also overstretched, though not to the point of failure. We have previously observed molecular-level collagen denaturation in cerebral arteries subjected to quasi-static loading [39], but damage patterns occurring at the high-rate deformations of TBI have not been defined.

1.3 Probing Collagen Structure

As discussed in detail elsewhere [3], healthy cerebral arteries have three layers: intima, media, and adventitia. The intima is composed of a layer of endothelial cells adhered to a thin basement membrane and is generally not considered to be mechanically relevant. The intima is separated from the media by the internal elastic lamina (IEL); this structure is the primary site of elastin in cerebral arteries. The media is made up of two helically opposed collagen fiber families that are largely circumferentially oriented. The media also contains smooth muscle cells that control dilation necessary to regulate the flow of blood in the brain. The adventitia largely consists of axially oriented fibers with a higher degree of dispersion than the medial fibers.

Fibrous collagen has a prominent structural hierarchy in fully matured tissues. Collagen fibers are large, optically resolved structures made up of many so-called collagen fibrils primarily bound together by proteoglycan bridges [57]. These fibrils, in turn, are made of bundles of tropocollagens, also known as collagen molecules, tightly packed together with short chemical crosslinks [108]. The tropocollagen molecule is

itself a super-secondary protein structure comprised of three polypeptide strands, called alpha chains, wrapped into a triple helix [109].

A recently developed collagen-hybridizing peptide (CHP) leverages a synthetic alpha chain imitation to enable reliable quantification of tropocollagen unwinding and denaturation [37, 110, 111]. CHP has lately been applied to identify mechanically induced damage to the tropocollagen matrix following overstretch of blood vessels and tendons [10, 37, 39, 40, 112, 113]. Furthermore, the amount of tropocollagen damage has been shown to correlate with both degree of overstretch [39, 113] and number of fatigue cycles [40].

Early CHP studies of mechanically induced damage relied entirely on fluorescence microscopy to quantify CHP binding [37, 39], but Lin et al. recently pioneered a protease-based method to read total CHP binding on a microplate reader [114]. This method allows for high throughput analysis and can overcome some limitations of optical imaging, though it does not allow for spatially detailed evaluation.

1.4 Study Goals

To investigate the influence of strain rate on mechanical damage to tropocollagen, we stretched cerebral arteries to failure at low (0.01 s^{-1}) and high ($>100 \text{ s}^{-1}$) rates, in both the axial and circumferential directions. We then probed the failed vessels for tropocollagen denaturation using CHP, comparing manual and automated quantification approaches. We also evaluated the use of the digestion method [114], as well as novel modifications for normalization of microplate readings, in analyzing CHP binding in small arteries.

2. Materials and methods

2.1 Overview

Göttingen minipig middle cerebral arteries (MCAs) were pulled to failure either quasi-statically (0.01 s^{-1}) or at high rate ($>100 \text{ s}^{-1}$), and in either the axial or circumferential directions. Following failure, vessels were stained with fluorescent CHP, mounted onto slides, and imaged using confocal microscopy. The same samples were then digested with Proteinase K, and CHP fluorescence of the resulting liquid was quantified. Fluorescence relative to controls was evaluated and compared between groups to determine the effect of strain rate and loading direction on collagen damage.

2.2 Tissue Preparation

Göttingen minipigs were euthanized by Beuthanasia overdose following a protocol approved by the University of Utah Animal Care and Use Committee. The brain was removed from the head and placed in calcium-free phosphate-buffered saline (PBS). MCAs were then resected, the pia-arachnoid complex was removed, and any side branches were ligated. Arteries were stored in PBS at 4°C until testing. All tests were performed within 48 hours of death. Dissected control sections of MCAs were maintained from each animal for use as a baseline reading of CHP.

2.3 Apparatus

Tests were conducted as previously described by Converse et al [39], except that all vessels were stretched to failure. High rate cases utilized a drop tower described by Bell et al [30]. Briefly, for axial tests, intact vessels were cannulated onto size-matched

needles submerged in a calcium-free PBS bath. The arteries were secured to the cannulas with 6-0 suture, and cyanoacrylate was applied distally to further secure samples to the needles. A voice coil actuator (AVM60-25, Motion Control Products, Bournemouth, UK) provided quasi-static axial displacements, and a syringe pump was used to maintain pressure. Circumferentially stretched samples were cut into rings and penetrated with parallel needles, similar to typical wire myography. A digital camera (PL-A741, Pixelink, Rochester, NY) recorded specimen motion to allow determination of strains. For high-rate tests, the voice coil was replaced with a drop tower where a steel ball was dropped into a catchment that transferred momentum to the fixture on one end of the artery via a steel cable. Additionally, the low frame-rate camera used for quasi-static motions was swapped for a high frame-rate camera (Phantom Miro EX4, Vision Research, Perth, Australia) to capture the high-rate deformations at 25 kHz.

2.4 Mechanical Test Procedure

In axial tests, arteries were preconditioned by oscillating luminal pressure from 50 to 150 mmHg five times at a given axial stretch. Axial stretch was incrementally increased from 1.0 to the in vivo stretch, the configuration where no change in axial force was detected during a pressure cycle [77]. One additional preconditioning cycle was then conducted at an axial stretch of 1.10 times the in vivo stretch. Following preconditioning, arteries were set to a physiologic luminal pressure (80 or 120 mmHg), axially buckled, and then failed either quasi-statically (0.01 s^{-1}) or at high rate ($>100 \text{ s}^{-1}$). The bath was drained immediately prior to the high-rate failure ramps. Samples were exposed to air for less than 30 seconds prior to failure.

In circumferential tests, the unloaded circumference of the sample was optically determined by imaging each side of the ring prior to testing and averaging the identified circumferences. Samples were then mounted onto the tester, stretched to 1.10 times the in vivo stretch, and allowed to stress-relax for five minutes to precondition the tissue. The in vivo stretch was approximated as the average circumferential stretch observed during preconditioning of all axial samples when pressurized to 100 mmHg and axially extended to in vivo stretch. As in the axial tests, samples were buckled and then stretched to failure either quasi-statically (0.01 s^{-1}) or at high rate ($>100 \text{ s}^{-1}$).

2.5 Staining

Immediately following failure, samples were returned to a PBS bath and refrigerated until staining, as previously described [39]. Briefly, a solution of $20 \mu\text{M}$ F-CHP (fluorophore tagged CHP; 3Helix #FLU300, Salt Lake City) was prepared in PBS. This solution was heated to $80 \text{ }^\circ\text{C}$ for 10 minutes and then cooled in an ice bath for 2 minutes. The tested arteries and associated controls were then each placed in $100 \mu\text{L}$ of the F-CHP solution and incubated at $4 \text{ }^\circ\text{C}$ for at least 16 hours. Following incubation, each vessel underwent three rinsing cycles in which they were repeatedly placed in a fresh PBS solution for 30 minutes with gentle agitation. After the final rinse, vessels were cut open longitudinally and laid flat, intima down, on glass slides using a mounting medium of Fluoromount (Fluoromount G; Southern Biotech).

2.6 Confocal Microscopy and Image Analysis

Each vessel was imaged using a confocal microscope with a 10X objective (Fluoview FV1000, Olympus), excited with the 488 nm laser channel (F-CHP emission is 512 nm). Several fields of view (512 X 512 pixels) were used to capture the entire vessel area at z-axis increments of 2 μm through the vessel wall for a complete digital capture of the vessel volume. Following image acquisition, a custom MATLAB (2021b, MathWorks) code was used to stitch images together such that the vessel could be analyzed in entirety.

Vessels were initially analyzed with a semi-manual approach (Figure 1). A single slice from each layer (media and adventitia) of the artery was used to quantify the CHP binding of the entire layer. Collagen fiber direction was used to identify which layer each image slice belonged to; that is, adventitial slices were selected as those in which the preponderance of visible collagen fibers were oriented along the axis of the vessel, and medial slices were selected for a predominant circumferential fiber orientation. The brightest slice within the identified layers was selected as the representative slice. Following stitching and slice selection, a digital mask was created to remove the image background, non-biological artifacts (i.e. sutures and dust), and confounding features such as areas of bunched tissue. Occasionally, image capture areas overlapped during microscopy leading to double exposure of some tissue; these were also manually identified and removed. The remaining (unmasked) vessel area was evaluated for attached CHP following a strategy similar to one previously developed [39]. Briefly, each sample, including controls, was normalized by the mean intensity value of its masked control (or, in the case of a control, normalized by its own mean). A threshold was

defined at two standard deviations above the mean of the normalized control image brightness (Figure 2a). The percent of pixels in the normalized sample image brighter than this threshold was determined and used as the final metric of damage.

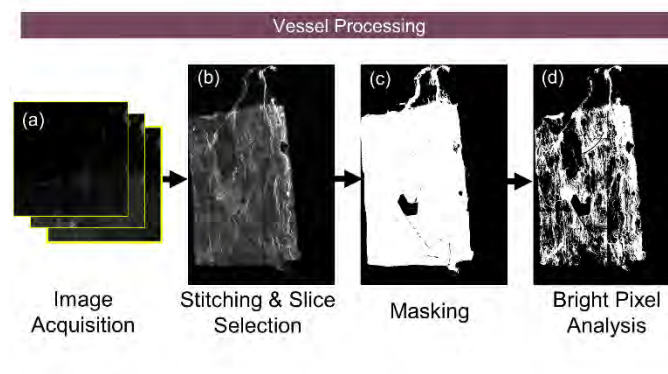


Figure 1 Flowchart of image acquisition and processing. Images (512x512 pixels) were captured and stitched, followed by either manual or automated approaches to evaluate CHP attachment. Bright pixels (d) are reported as a percentage of unmasked area (c).

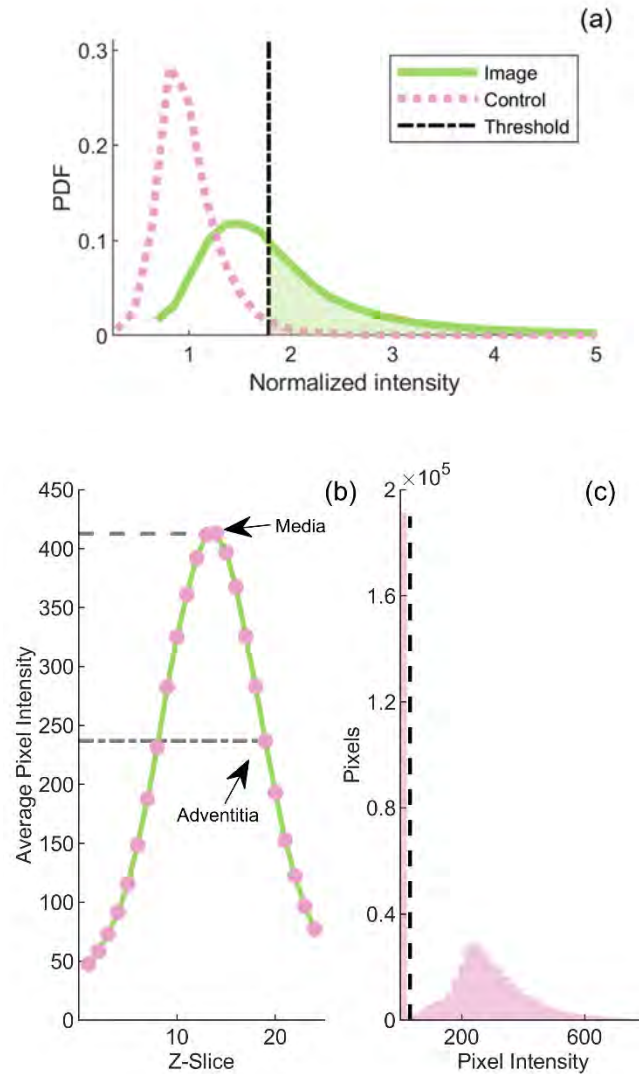


Figure 2 Image characteristics used during vessel processing for a representative sample. For both manual and automatic methods, the number of pixels brighter than two standard deviations above the mean of the control sample was tallied (a), as shown by the shaded region of the probability density function (PDF). The average brightness of vessel slices (b) was used to automatically determine the location of the media and adventitia. The media is indicated as the slice with the greatest intensity, while the adventitia is identified as the 57th percentile of slice brightness. A pixel intensity histogram (c) was used in the automated approach to mask debris and the image background (mask threshold shown as a dashed line).

An automated approach was also investigated to minimize the potential for researcher bias. In the manual method, the media was observed to be the slice with the greatest average intensity. This observation was thus used to select medial slices

automatically. Similarly, the adventitial slice was identified, on average, at the 57th percentile of intensity (± 14 percentile points) in the manual method. As such, in our automated code, adventitial slices were selected as those closest to the 57th percentile of brightness within each image z-stack at depths above the previously identified media. As the intention of the automated approach was to remove sample-to-sample bias, we feel that this method is sufficiently robust for automatically identifying the adventitia.

Automatic selection parameters for both representative slices are presented in Figure 2b. Note that the percentile was selected based only on axially failed vessels (as opposed to those failed circumferentially); a greater amount of tissue area in axially failed vessels allowed for more easily recognizable fiber direction and more researcher confidence in the results of the manual approach. Following layer selection and stitching, a digital mask was automatically generated based on the histogram of all pixels in the compiled image. The first local minimum of the histogram (Figure 2c) was found to distinguish brightness values between dark pixels (usually occurring in the background of the image area, as well as some imaging artifacts such as dust and debris) and the pixels representing the tissue being examined. All pixels with a brightness less than that occurring at the histogram minimum were masked out and not considered during quantification. Confounding image features such as branches and areas of double exposure were not removed in the automatic approach.

2.7 Proteinase K Assay

After confocal imaging, samples from the axially stretched group were removed from slides and placed in 100 μ L of 1 mg/mL Proteinase K (Sigma Aldrich, P2308) at 60

°C for 24 hours; we found that exposure for three hours (as suggested by Lin for tendon [114]) did not appear to adequately homogenize these cerebral vessels, potentially due to additional structural constituents in blood vessels. After homogenization, the 100 μ L volume was split into two 50 μ L duplicates, and fluorescence was quantified using a microplate reader (SpectraMax Gemini XPS) set to an excitation wavelength of 485 nm and an emission wavelength of 525 nm, as outlined by Lin et al.

Multiple techniques were evaluated for normalizing total fluorescence. The first technique used was simply normalizing by the two-dimensional area of the vessel, as obtained during confocal microscopy. The second normalization technique was dry sample weight measured using a microbalance (UMX2 ultra-microbalance, Mettler Toledo). The final technique was a hydroxyproline assay (Sigma-Aldrich MAK008), performed to quantify the amount of collagen in the sample by virtue of the amount of hydroxyproline (an amino acid largely restricted to collagen) [115]. In brief, the oxidized hydroxyproline in a hydrolyzed solution of the digested samples was reacted with 4-(dimethylamino)benzaldehyde to produce a colorimetric solution. The absorbance was read at 561 nm by the microplate reader. The absorbance, proportional to hydroxyproline content, was compared to a standard curve to calculate the concentration of hydroxyproline in the solution, and by extension, the amount of collagen in the sample.

2.8 Statistical Analysis

Student's t-test was used to compare the quasi-static and high rate groups for each test type (i.e., the effect of rate was separately evaluated in both the adventitia and media in both axially and circumferentially stretched samples). Because results from different

layers and test directions were categorically different, layer and test direction were not evaluated as variables.

3. Results

As in our previous work, experiments here produced collagen molecule damage in fibers aligned with the direction of loading. However, these experiments also revealed CHP binding in vessel layers where the predominant fiber direction is transverse to the direction of loading (e.g., medial damage resulting from axial loading). As a result, we differentiate between damage observed in fibers aligned with and transverse to the direction of loading in the Results and Discussion.

3.1 Rate Dependence of Tropocollagen Damage in Fibers Aligned with Loading Direction

Aligned loading resulted in different extents of tropocollagen denaturation between the quasi-static and high-rate groups as identified by confocal microscopy. Axial samples pulled quasi-statically showed visually apparent areas of axially oriented fibrous damage in the adventitia (Figure 3), similar to that reported in our previous work [39]. Generally, vessels pulled at high rates showed little fibrous damage. This visually apparent difference between rate groups was confirmed statistically (Figure 4; $p=0.025$, manual masking). Although high-rate samples displayed significantly less denaturation than quasi-static vessels, CHP staining was still substantially greater than that found in controls. As with the adventitia of axially stretched specimens, the media of vessels failed circumferentially showed generally increased denaturation at quasi-static rates compared

to high rates (Figure 5). As previously reported [39], circumferential stretch typically produced an increase in general brightness of the media in contrast to bright, individual fibers, as typical in axial stretch. Rate dependence in the media was further confirmed statistically (Figure 4; $p=0.007$).

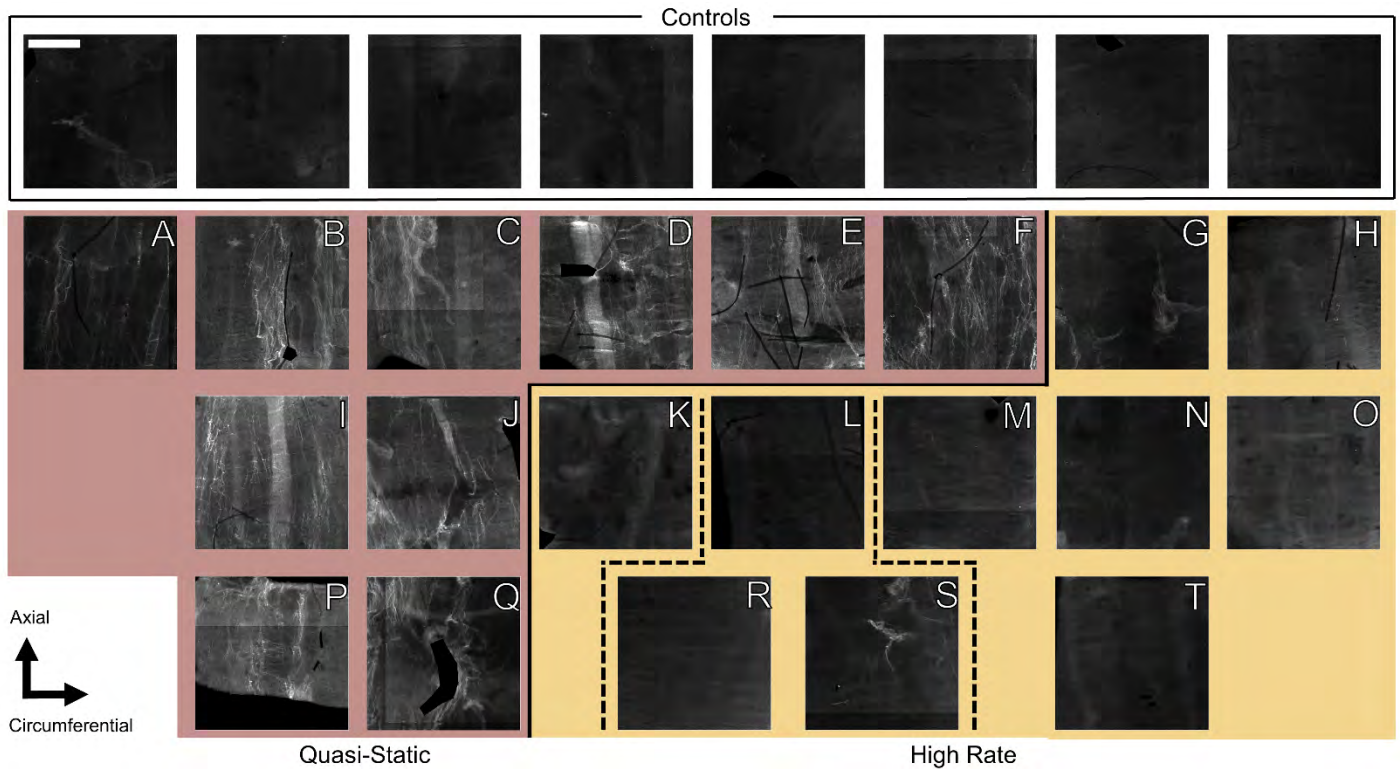


Figure 3 Adventitial tropocollagen denaturation in vessels stretched axially at quasi-static and high rates. A single representative image was selected from each vessel to demonstrate observed differences between quasi-static (left) and high-rate (right) loading scenarios. The first row consists of controls; corresponding damaged vessels are displayed vertically beneath. A strong trend of rate dependence was observed, with vessels stretched quasi-statically exhibiting consistently more CHP attachment than high-rate counterparts. All images shown were manually masked and normalized by average control brightness to simplify visual comparison. Note that samples R and S are in the same group as E and L. Scale bar is 300 μm .

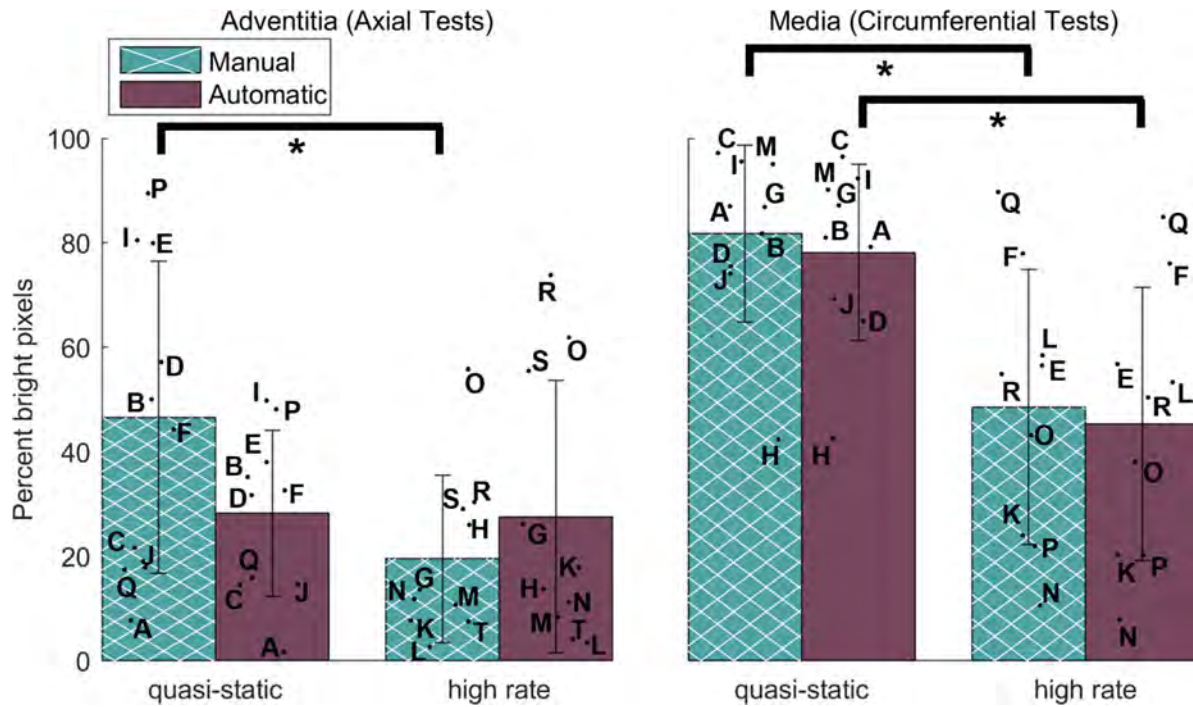


Figure 4 Mean and standard deviation of collagen denaturation (percent bright pixels) as a function of loading rate for collagen-aligned deformation. Results for both axial (adventitia damage) and circumferential (medial damage) tests are shown. Both manual and automatic quantification results are also presented. Adventitial tropocollagen (left) is delaminated much more readily in samples axially failed quasi-statically than in axial samples failed at high strain-rate, as quantified by the amount of bound CHP observed with a confocal microscope. Rate dependence in aligned collagen is maintained in circumferentially failed vessels as observed by CHP expression binding in the media (right). For reference, the undeformed control samples all have 2.5% bright pixels on this scale given our methods. Letters identify quantified values for individual samples labeled in Figures 3 and 4.

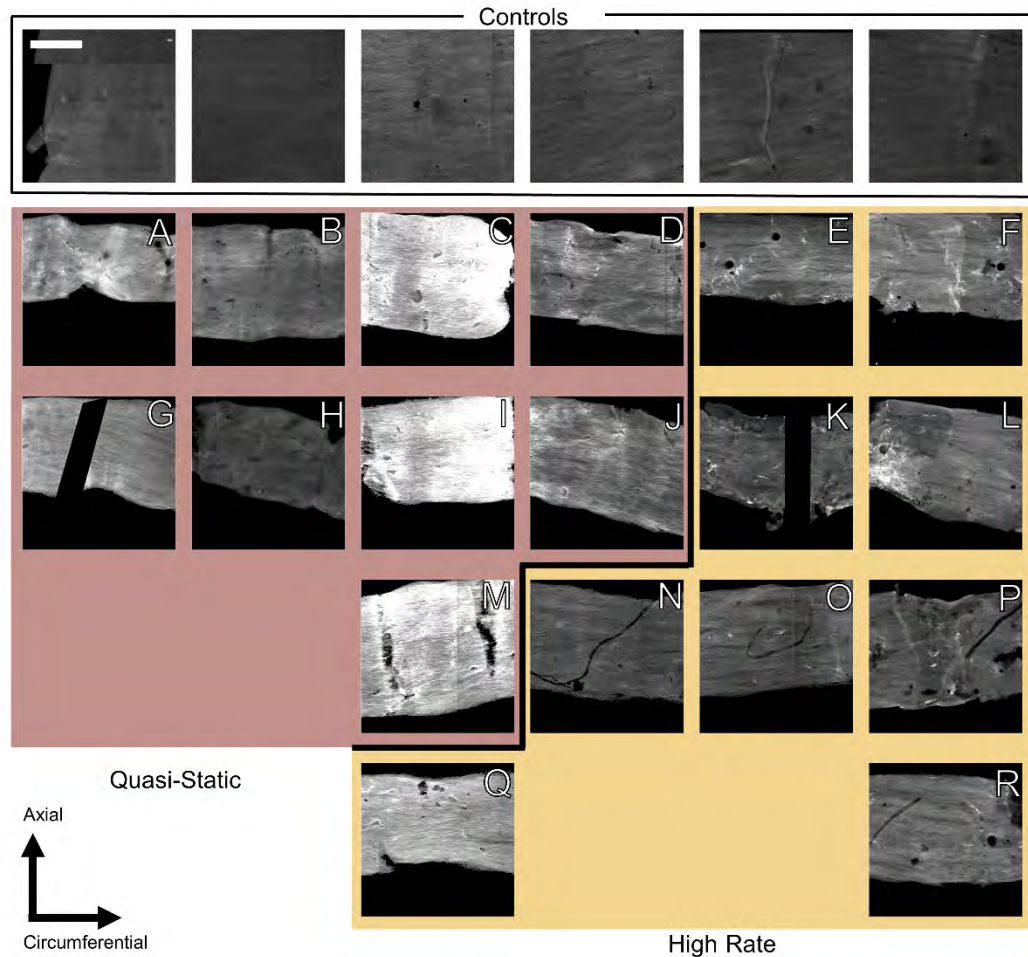


Figure 5 Medial tropocollagen denaturation in vessels stretched *circumferentially* at quasi-static and high rates. Circumferentially damaged vessels exhibited a more diffuse brightness pattern than those stretched axially, but dependence on rate persisted. All images shown were manually masked and normalized by average control brightness to simplify visual comparison. Scale bar is 300 μm .

3.2 Evidence of Tropocollagen Damage in Fibers Transverse to the Loading

Direction

In addition to damage seen in load-aligned fibers, increased brightness was unexpectedly observed in layers containing transversely oriented fibers, most notably in the media of axially stretched vessels (Figure 6). Increased brightness of adventitial fibers in circumferential tests was also apparent for some cases (Figure 7). In both cases, this

damage generally appeared less distinct than that seen in aligned fibers. This increased brightness in transversely oriented fibers did not visibly appear to be dependent on strain rate, statistically (Figure 8).

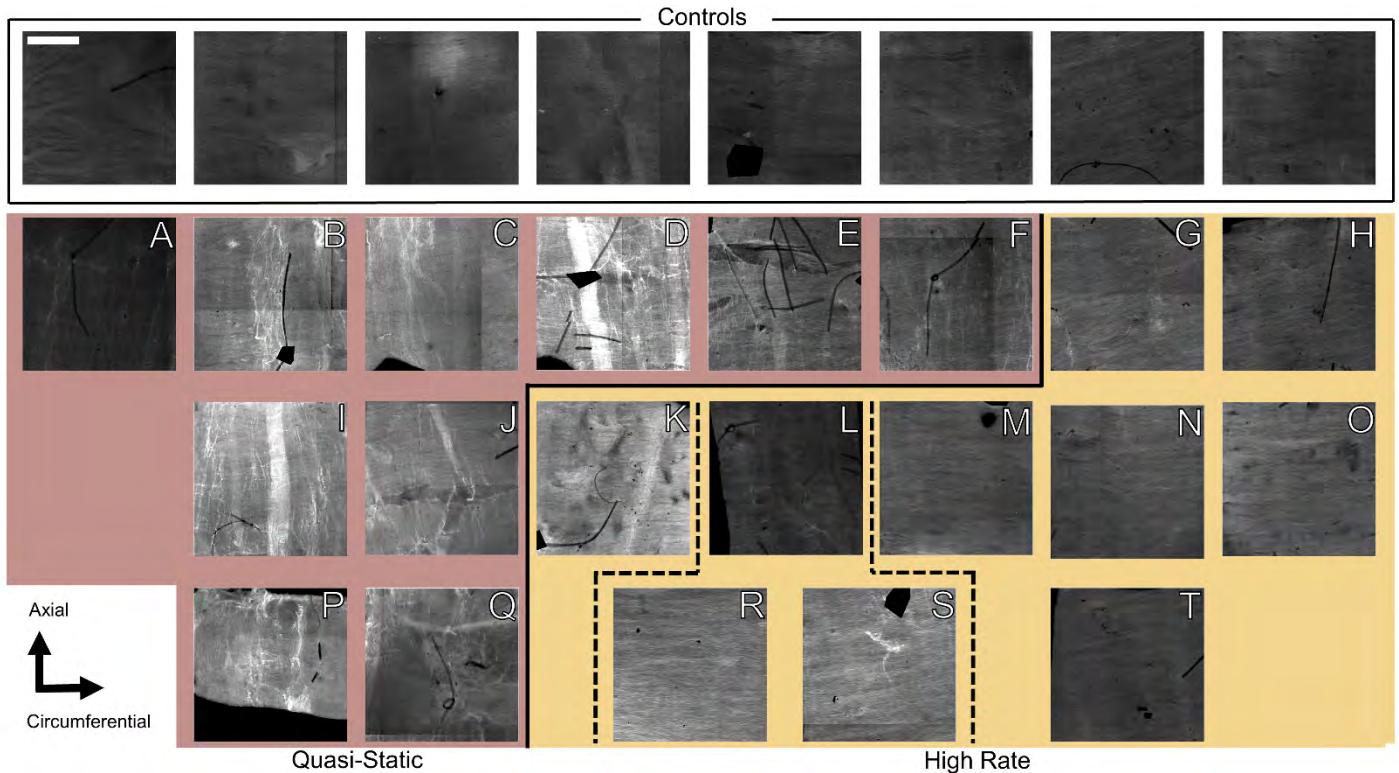


Figure 6 Representative images of *medial* slices in *axially* stretched vessels (i.e., loading direction transverse to fiber direction). Out-of-focus light is apparent in some of the quasi-static samples (for example, compare samples B and I here with B and I in Figure 3); however, the lack of out-of-focus light in the high-rate vessels is suggestive that the detected damage is due to transverse loading, alleviating concerns that signal from the damaged adventitia leads to our conclusion of transverse damage. All images shown were manually masked and normalized by average control brightness to simplify visual comparison. Scale bar 300 μm .

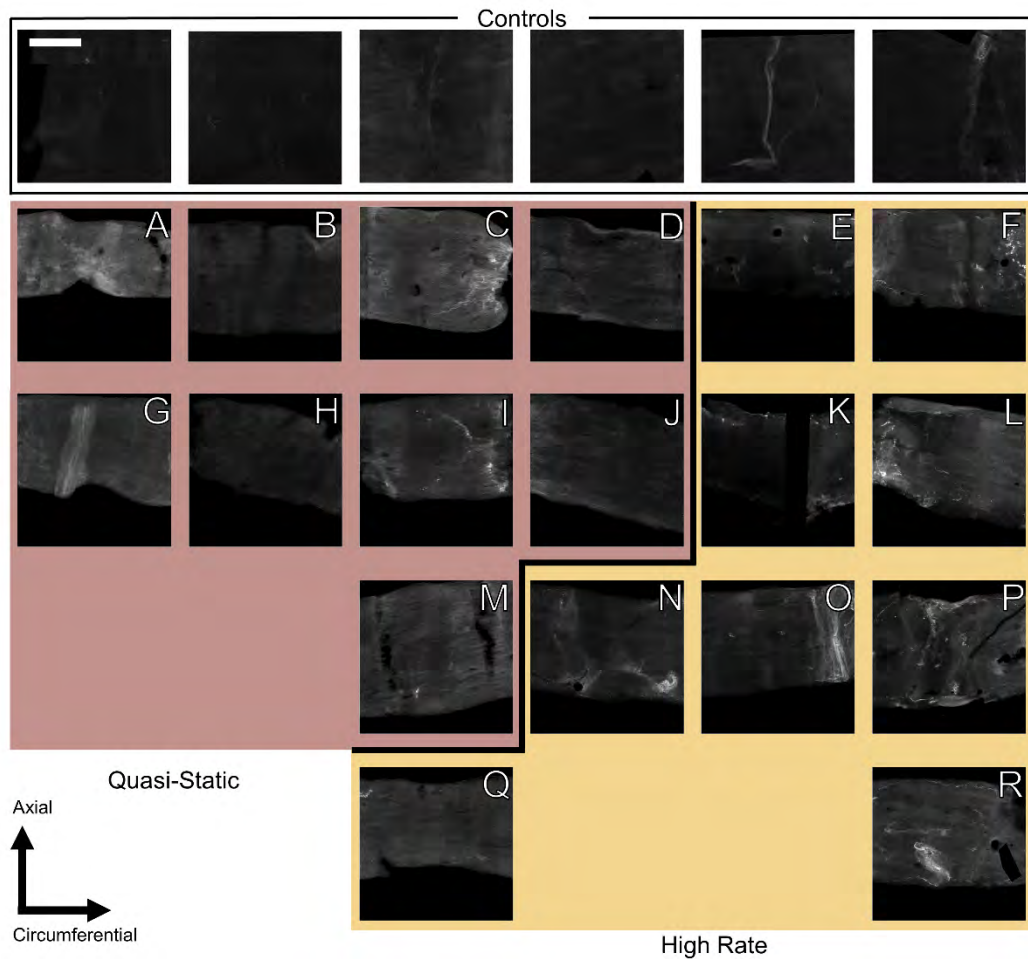


Figure 7 Representative images of *adventitial* slices in *circumferentially* stretched vessels. Most vessels, both quasi-static and high rate, are absent of oriented fibrous damage characteristic of axially stretched samples. All images shown were manually masked and normalized by average control brightness to simplify visual comparison. Scale bar is 300 μm .

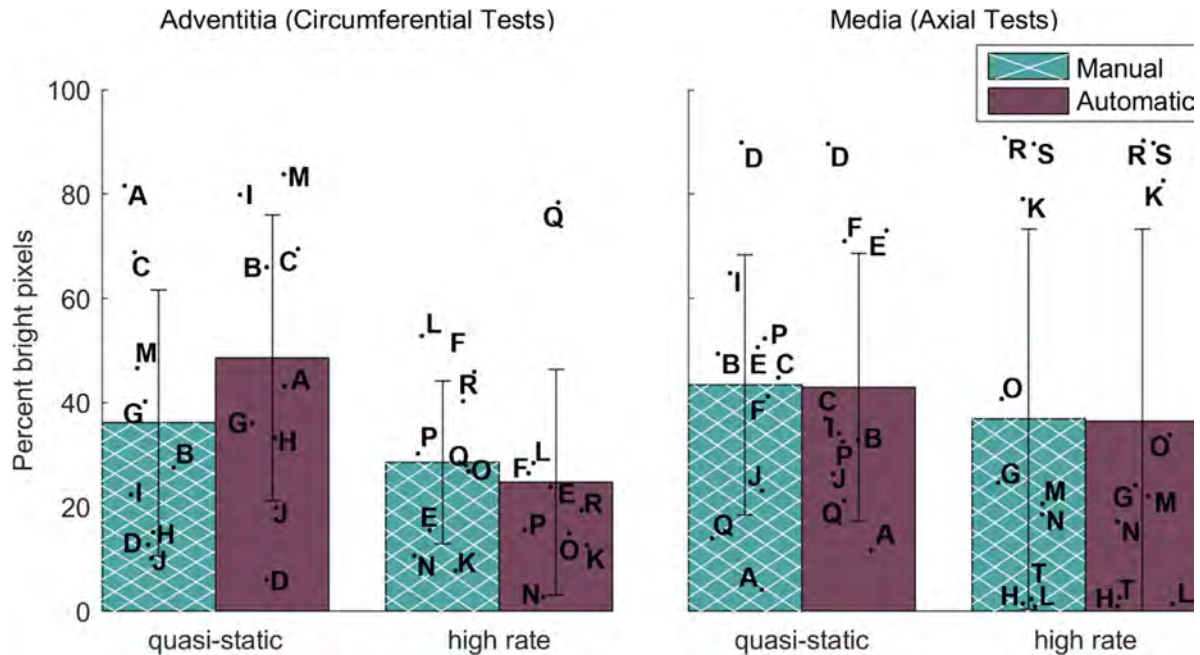


Figure 8 Mean and standard deviation of collagen denaturation (percent bright pixels) in fibers transverse to the direction of loading, as a function of loading direction and rate. Results are summarized for medial and adventitial collagen following axial and circumferential tests, respectively. Both manual and automatic methods are shown. In both vessel layers, denaturation of transversely loaded tropocollagen is apparently unaffected by strain-rate in most comparisons.

3.3 Image Quantification Algorithm

Another objective of this study was to evaluate modifications of our previously reported [39] quantification algorithm, specifically the automated features included to reduce researcher bias. Table 1 shows little difference in results between methods relying heavily on human input and those which were automated, with the exception of the axially failed adventitial samples; this exception is possibly due to contributions from tissue anomalies as explained in the Discussion.

Table 1 CHP quantification (percent bright pixels, using a threshold of two standard deviations of the corresponding unnormalized control sample) and p-values associated with the rate comparison for each set of tests

	<u>Manual (mean \pm std)</u>			<u>Automated (mean \pm std)</u>		
	Quasi-static	High Rate	p-value	Quasi-static	High Rate	p-value
Axial	46.6 \pm 29.9	19.6 \pm 16.0	0.025	28.3 \pm 15.9	27.6 \pm 26.1	0.948
Adventitia						
Circ. Media	81.7 \pm 17.0	48.6 \pm 26.3	0.007	78.1 \pm 16.9	45.3 \pm 26.1	0.007
Axial Media	43.4 \pm 25.0	36.9 \pm 36.5	0.646	42.9 \pm 25.6	36.5 \pm 36.9	0.656
Circ.	36.1 \pm 25.5	28.5 \pm 15.6	0.459	48.6 \pm 27.4	24.7 \pm 21.6	0.058
Adventitia						

3.4 Enzymatic Quantification

Among the three normalization methods evaluated for enzymatic digestion, two-dimensional area was found to be closely related to both vessel weight (correlation coefficient = 0.96, n = 12) and the hydroxyproline assay (correlation coefficient = 0.98, n = 14), suggesting any one of the three is reasonable to use for normalization. All presented digestion results were thus normalized by two-dimensional area. Regardless of normalization technique, and in contrast to local analysis of single layers by microscopy, global enzymatic digestion suggested no significant differences between either group of damaged vessels and their corresponding controls or between rates.

4. Discussion

The primary objective of this research was to evaluate the rate dependence of molecular-level collagen denaturation in cerebral arteries stretched to failure. Results show that collagen fibers aligned with the direction of loading are highly sensitive to strain rate, with less damage occurring at high rates, despite all samples being pulled to structural failure. Additionally, denaturation of transversely oriented fibers was observed but was not rate dependent.

4.1 Aligned Collagen

Our results show that tropocollagen denaturation is strongly dependent on rate in failure tests of cerebral arteries. While not previously observed in arteries, several researchers have reported similar results in tendon. Willet et al. failed bovine tail tendon at either 0.01 or 10 s⁻¹ prior to acetyltrypsin and α -chemotrypsin proteolysis [31]. They found a statistically higher degree of tropocollagen disruption in the quasi-static group than in the high-rate group in their study and subsequently reinforced the significance of rate dependence in experiments using differential scanning calorimetry [32]. Chambers et al. similarly failed bovine extensor and flexor tendons at either 1 or 10% s⁻¹ and imaged the fibrils with scanning electron microscopy (SEM). While damage developed differently in the two tendon types due to cross-linking differences, results demonstrated a general decrease in tropocollagen damage with increasing rate, including no apparent collagen disruption in flexor tendons at the highest rate [33]. Although not involving tests to failure, Zitnay et al. quantified tropocollagen damage as a function of rate in cyclic

fatigue experiments of rat tail tendons [10]. Using CHP, they found less tropocollagen damage per cycle at high (40% s⁻¹) than low (0.4% s⁻¹) rates.

Mechanisms governing collagen damage observed in failure of soft tissues are of interest in ongoing research. The models of Zitnay et al. showed that tropocollagen unfolding is rate dependent, with weaker hydrogen bonds dominating the quasi-static response and stronger covalent bonds controlling the high-rate response [37]. While it is tempting to apply these results to our findings, it is important to note that we previously reported a statistically significant reduction of failure stretch in arteries failed at high strain rates compared with those failed quasi-statically [107]. Because our previous work showed that the threshold for collagen denaturation is relatively high (close to the failure point) in quasi-static tests of cerebral arteries [39], it is possible that the rate-induced reduction in failure stretch results in the collagen fibers not achieving a high enough stretch to induce tropocollagen denaturation. Additionally, the presently identified reduction of tropocollagen unfolding with complete tissue disruption at high rates closely matches the previously reported lack of CHP binding at locations of tissue cut with scissors [37, 39], indicating that a similar failure mechanism may be active; that is, perhaps tropocollagen molecules are torn apart with little relative sliding between alpha chains at high rates.

Several groups have speculated on the question of how damage accumulates elsewhere in the collagen hierarchy during high-rate deformations. One idea is that inter-fibrillar proteoglycans viscously slide relative to each other and that the onset of damage occurs when proteoglycan overlap decreases beyond a critical level [14, 16], such that the fibril arrangement within the fiber is plastically changed. Puxkandl et al. found an

increase in the ratio of fibril to bulk tissue elongation between 0.001 and 0.1% s⁻¹ in synchrotron X-ray diffraction of rat-rail tendon. However, this observed increase in fibril strain with rate is inconsistent with more recent experiments that show rate-stiffening in isolated collagen fibrils [116]. Further, Bonner et al. performed experiments similar to those of Puxkandl et al. at higher rates (0.001 – 0.05 s⁻¹), in human lateral collateral ligaments, and found that increasing strain rate reduced fibril strain by a factor of approximately three at high strain [117]. These latter findings appear to agree with the here-observed reduction in tropocollagen denaturation at high rates, and suggest that strain is accumulating in the interfibrillar matrix. Bonner et al. proposed a damage mechanism wherein the interfibrillar matrix is debonded from the collagen fibrils at higher strain rates. Matrix debonding could explain our findings and would not negate Gasser's model of proteoglycan slipping, nor our observations of tropocollagen denaturation, at lower strain rates.

Veres and Lee proposed a fibrillar kinking damage mechanism that may alternatively explain our present results [36]. Chambers et al. [33] recently investigated the effect of strain rate on this damage mechanism and concluded that in both moderately and highly crosslinked tendon there is a shift toward less fibrillar kinking. They attribute this to localized point failures at high strain rates; that is, at high strain rates the tissue does not have sufficient time to distribute the load. With this mechanism in mind, tropocollagen denaturation may still be the primary failure mode at high strain rates, yet at a much lower level than at quasi-static rates.

4.2 Transverse Collagen

To our knowledge, this is the first study to observe tropocollagen denaturation in fibers oriented transverse to the direction of loading, likely because collagen damage is typically studied in tissues having just one collagen fiber family. While it is clear that the media is loaded in tests to failure, it is not obvious that the collagen fibers would be damaged as they are not loaded in the fiber direction. For example, transverse loading of a single-fiber-family composite material typically results in failure of the matrix while the fibers are left intact. Because examining transverse fibers was not a focus of this study, we were initially surprised by these findings and had concerns that mounting or preconditioning was responsible for the increased CHP binding. To investigate this, we subjected a small number of samples to just the mounting and removal procedures (n=4), as well as to mounting, preconditioning, and removal (n=3). While these sample sizes are too small to draw firm conclusions, negligible levels of CHP binding were observed (an average of 0.07% bright pixels), suggesting that this is a real phenomenon that warrants further study.

The mechanism of this transverse damage is unclear. Collagen fibers in arteries are not perfectly aligned with the axial and circumferential directions, but are, rather, distributed around a slightly offset angle. Canham et al. found the most extreme medial fibers to be a mean of only 1.5 degrees offset from the circumferential direction in human MCAs. Wicker et al., on the other hand, found the adventitial fibers of rabbit basilar arteries to be offset by a mean of 20.2° in samples pressurized to 80 mmHg [48]. A simple calculation of adventitial fiber stretch using the deformation gradient [118] of the circumferentially failed vessels leads to the conclusion that the adventitial fibers were

hardly stretched past what they experienced in the preconditioning process, alleviating concern that the identified transverse damage was a result of fibers rotating to be aligned with loading.

Another consideration is the 3-D organization of collagen fibrils within a fiber. While fibrils are generally aligned with the fiber direction, some align transverse to the fiber direction at times [119]. These laterally oriented fibrils may become overstretched during transverse loading of the fiber. Additionally, Converse et al. [39] noted that fluorescence from CHP can illuminate adjacent vessel layers and lead to incorrect identification of damage there. Here, we believe that damage in transversely loaded fibers is not an imaging artifact because the signal pattern does not match that seen in load-aligned layers. All things considered, it seems reasonable that tropocollagen could also be pulled apart in the transverse direction, much like a string being separated transversely into its separate fibers. In this case, there may be less sliding between the procollagen molecules than in aligned fiber deformations, but binding sites would still be opened up to allow for CHP attachment.

Interestingly, we've previously demonstrated transverse softening in cerebral arteries [27], where axial overstretch induced circumferential softening. We previously reasoned that this was a natural consequence of damage in one direction of a biaxially loaded structure, but observations of transverse damage here suggest that it may also contribute. In any case, these results imply that contemporary continuum damage models of collagenous tissue, where collagen damage is accumulated solely as a function of fiber stretch (i.e. [38, 93, 96]), may need to be re-evaluated.

Finally, it is also notable that damage to transverse fibers was not rate dependent, in contrast to that in aligned fibers. This difference may shed light on rate dependent damage distribution through the collagen hierarchy with additional research.

4.3 Medial vs Adventitial Damage

As observed by Converse et al., there are qualitative differences in spatial damage patterns between the media and adventitial layers. In general, images of circumferentially stretched vessels contained more noise than axially stretched samples. The circumferentially failed vessel samples were smaller than axial vessels (2-D Area Axial: $2.58 \pm 0.90 \text{ mm}^2$, Circumferential: $1.14 \pm 0.19 \text{ mm}^2$). As a result, there was a higher percentage of the area characterized by catastrophic tissue damage in these samples, where tissue is damaged to the point that layer specific differences are difficult to distinguish, and tissue bunches up and produces artificially high fluorescence. The masking of such areas, however, is subject to the experience of the researcher and may significantly decrease the total area available for quantification. This global disruption of specimens combined with the decreased sample size of circumferential versus axial vessels may account for the larger standard deviations in the circumferential data.

4.4 Methods Evaluation

As part of this work, we sought to improve our CHP quantification methodology. This was a two-fold evaluation: (1) we investigated the utility of increased automation in the confocal image analysis algorithm, and (2) we applied the Lin quantification method

[114] where microplate readings of enzymatically digested tissue provide a global quantification of CHP attachment.

Confocal evaluation of CHP-marked damage previously relied heavily on the experience and decision-making of the researcher performing the analysis. Masking of image artifacts and non-biological features required manual input, providing a potential source of bias. Both masking and selection of vessel layers for analysis were automated here to minimize introduction of bias. This increased automation was largely shown to not alter the results of CHP quantification by confocal microscopy, with the exception of the axially failed adventitia samples. Some samples had substantial branches that were manually masked out; however, as the branch points were brighter than surrounding tissue, the automated masking algorithm did not remove these artifacts. As such, we suspect that unmasked branches in the control samples may have elevated the damage threshold, changing the results compared with the manual method. Alternatively, axial damage may simply be more affected by variations in slice selection. The approach developed to select adventitial slices may not have been adequately able to account for strong background signal from the media of the vessel, which has been observed to occur at the transitional depth between adventitial and medial layers. In any case, we are confident that the rate effect observed using the manual approach in these samples is real and thus conclude that more refinement of the automated approach is needed.

Analysis of imaged vessels was improved via development of a variance-controlled standard (i.e. two standard deviations above the mean) for control brightness threshold values. Previous methods relied on arbitrary assessment of perceived damage to determine a threshold value, leading to a potentially more conservative approach. As

noted, areas of more subtle damage were often excluded from the final analysis [39]. Moving to an approach based on the distribution of control pixel brightness allows for more sensitivity when detecting damage areas and is more accommodating of inter-specimen differences in controls. It is, however, interesting to observe that when the previously established method is applied in quantifying the adventitia of axially stretched vessels processed automatically, the resulting difference between quasi-static and high-rate groups is more similar to that seen in the manual approach. This is likely a reflection of the inherent differences in sensitivity between the quantification methods. This observation provides direction for further development of quantitative measures which are both sensitive and specific to observed damage patterns.

We recognize that our image quantification strategy is still relatively rudimentary, and we expect future work to continually improve the quantification of CHP-identified damage in vessels. However, the automation of vessel processing was intended to support the manual approach and has shown that the significant trends observed were not the result of human bias.

Analysis of digested tissue resulted in no substantial difference in brightness relative to vessel controls, regardless of rate-dependent grouping. Both controls and damaged vessels, however, were more fluorescent than blanks of pure Proteinase K. Within the context of results found using confocal microscopy, it seems likely that the enzymatic approach described here is not sensitive enough for use with tissue samples of this size (average area of 2.58 mm²; thickness of roughly 80 μ m). While these results do not eliminate the possibility of using this approach for future studies, the size of the target tissue and scale of associated damage should be carefully considered before relying

solely on an enzymatic assay. It is also possible that undissolved elastin particulates confounded the assay as the solution was not filtered prior to microplate analysis, although we saw no remarkable change in emittance following the addition of elastase to the Proteinase K solution. Normalization is a particular challenge. Weighing samples of this size is generally unreliable outside of a clean room and with commonly available balances, as the average dry weight of the examined vessels was 38.8 μg (max 115.0 μg , min 14.2 μg) and may easily be confounded by dust or other debris introduced during weighing. Similarly, the hydroxyproline assay requires several transfers of liquid, with each transfer potentially contributing to compounding errors. Two-dimensional area is the least likely of the three methods to be affected by error. Obtaining 2-D area via microscopy has the additional benefit of providing microscopy data which may be critical for a full understanding of damage characteristics. Because comparison between all three normalization methods led to little difference between any given method, we recommend using 2-D area. We ultimately conclude that the microplate reader-based method may not be appropriate for small arteries due to the high level of baseline collagen remodeling, low sensitivity of the microplate reader, and the loss of layer-specific analysis due to protease digestion. Researchers should thus consider using confocal-based imaging for the evaluation of CHP in small tissues and in cases where layer-specific information is important.

4.5 Biologic Implications

Preliminary post-mortem controlled cortical impact (CCI) studies on sheep (unpublished) showed a lack of CHP binding in cerebral arteries, even in regions

immediately proximal to sites of hemorrhage. These *in vivo* results are consistent with the present *in vitro* findings; that is, high-rate failure does not appear to lead to substantial tropocollagen denaturation. Furthermore, tropocollagen denaturation may not be relevant in cerebral vasculature following TBI.

There are several potential implications of the observed rate dependence of molecular damage. Perhaps the most interesting is the effect that rate may have on healing, or on remodeling subsequent to injury. Veres et al. found that macrophage-like cells (U937) behave differently when seeded on fibrils damaged by overstretch than they do on matched controls [120]; specifically, they reported U937-induced enzymatic digestion in locations of denatured tropocollagen [36]. Given this association between denatured collagen and healing response, a substantial decrease in molecular denaturation during tissue damage may elicit a weaker biologic response to the injury. Rate may then be a useful parameter to change the healing response following procedures such as angioplasty or surgical incision. Likewise, other vascular interventions may be better informed by a more complete damage model considering rate as an important factor in collagen damage levels.

Acknowledgements

- The Henry M. Jackson Foundation for the Advancement of Military Medicine (HJF), partially funded by the U.S. Army Medical Research and Development Command (Contract No. W81XWH-17-2-0008).
- National Science Foundation (NSF) (Award No. 2027367).

- We acknowledge Cell Imaging Core at the University of Utah for use of equipment

CHAPTER 5

MECHANICAL SOFTENING IS INDEPENDENT OF STRAIN RATE IN CEREBRAL ARTERIES

Abstract

Collagenous soft tissues are frequently injured by supraphysiologic mechanical deformation, leading to measurable changes in both extra-cellular matrix (ECM) structure and mechanical properties. While each of these alterations have been well studied following quasi-static deformation, little is known about the influence of high strain rate. Previous investigations of high-rate ECM alterations found tropocollagen denaturation and fibrillar kinking to be rate dependent. Given these observations of rate dependence in microstructure alterations, the present work evaluated if the rate and magnitude of overstretch affect the baseline viscoelastic properties of porcine middle cerebral arteries (MCAs). Changes in tissue response were assessed using a series of harmonic oscillations before and after subfailure overstretch across a variety of rates and magnitudes. We used collagen-hybridizing peptide (CHP) to evaluate the role of tropocollagen denaturation in mechanical softening. Experiments show that softening is dependent on overstretch magnitude but independent of overstretch rate. We also note that softening progresses at the same rate for both equilibrium (quasi-static) and non-equilibrium (high-

rate) properties. Finally, we observe that tropocollagen denaturation is not the source of the observed sub-yield softening behavior. This study expands fundamental knowledge on the form-function relationship of constituents in collagen fibrils and clarifies material behavior following sub-failure overstretch across a range of strain rates.

1. Introduction

The function of many soft tissues, such as arteries, tendons, and ligaments, is closely related to their mechanical properties [8-10]. These properties are governed by the composition of constituents [8, 102], which can be altered by various processes, including aging [121], disease [11], and traumatic events, such as surgery [12] and injury [3, 13]. Of particular interest to soft tissue mechanics is the interplay between alterations of the extracellular matrix (ECM) and damage, or softening of the mechanical response of the tissue. The definition of this interplay is critical to constitutive model development. It also helps identify targets for injury-specific therapeutics [15] and promotes the optimization of medical devices [16].

Persistent changes to the ECM structure resulting from mechanical overstretch have been extensively studied at quasi-static rates (e.g., [36, 37, 39, 122, 123]). While much less is known about changes due to high strain rate deformations, the few studies investigating the question largely agree that there is a rate-dependent shift in mechanisms of ECM alterations [10, 31-33]. Even less is known about the effect of high-rate overstretch on mechanical softening, but it may also be rate-sensitive. A study by Kurz *et al.* supports this speculation and additionally determined that equilibrium (quasi-static) and non-equilibrium (high-rate) tissue response softened differently depending on the rate

of overstretch. In their study on compression of cartilage plugs, the non-equilibrium behavior softened more dramatically following high-rate overstretch [105].

High-rate damage of cerebral arteries is of particular interest as they are frequently damaged in traumatic brain injury (TBI) [2, 3]. They are readily stretched to failure (and hemorrhage) in severe injuries, and physiologic dysfunction is often observed even in an intact cerebrovascular network [124]. Additionally, computational models suggest that the cerebrovasculature plays a vital role in the resistance of the brain to mechanical deformations [5-7]. We have previously shown that subfailure overstretch of cerebral arteries denatures tropocollagen [39] and softens the vessels both uniaxially [26] and biaxially [27]. As strain rates in the range of 10-100 s⁻¹ are typical in TBI [125], it is important to characterize high-rate alterations to the cerebrovascular ECM. We have recently shown a definitive and substantial reduction in tropocollagen denaturation (also commonly referred to as tropocollagen delamination or unfolding) following high strain rate failure of cerebral arteries compared with quasi-static failure [Chapter 4]. We have not, however, explored the effect that overstretch rate has on the mechanical response of tissue.

The objective of this paper was to define the influence of overstretch rate and magnitude on both mechanical softening and tropocollagen denaturation in cerebral arteries. Specifically, we evaluated whether the rate of overstretch (i.e., quasi-static vs high rate) would affect the softening behavior due to overstretch of the tissue following deformations across a variety of overstretch magnitudes. This softening was assessed in both the equilibrium and non-equilibrium components of the response. We also probed for tropocollagen denaturation following overstretch to correlate softening behavior with

tropocollagen unfolding. This study contributes to fundamental knowledge on form-function relationships of the ECM and provides insights into functional changes of soft tissue following differing rates of injury (i.e. quasi-static vs. high rate).

2. Methods

2.1 Overview

Middle cerebral arteries from Göttingen minipigs were preconditioned prior to the characterization of their axial viscoelastic properties. They were then overstretched in a single subfailure ramp at strain rates ranging from 0.05 to 50 s⁻¹ to overstretches ranging from 1.1 to 1.4 times the *in vivo* stretch. The samples were then recharacterized, removed from the tester, and stained with collagen hybridizing peptide (CHP) to quantify denatured tropocollagen. Changes to the dynamic modulus across the range of frequencies were evaluated as a function of both magnitude and rate of overstretch.

2.2 Tissue acquisition and sample preparation

Göttingen minipigs (24–26 week-old) were euthanized by Beuthanasia overdose under the approval of the University of Utah Institutional Animal Care and Use Committee. Fifty-four samples were resected from 14 unique animals. The brains were removed, and the middle cerebral arteries (MCA) were resected. The pia-arachnoid complex was dissected off the artery surface, and all side branches were ligated to allow pressurization. Thin rings removed from each end were imaged to provide a reference cross-sectional area.

2.3 Test procedure

Vessels were preconditioned as previously described [30] by oscillating luminal pressure five times from 50-150 mmHg at a stationary axial stretch. This oscillation was repeated at increasing levels of axial stretch until the *in vivo* axial stretch λ_{IV} was identified, where pressure oscillations did not change the measured axial force [77]. The pressure was then oscillated one more time at 1.05 times the *in vivo* stretch.

Following preconditioning, the baseline viscoelastic properties of the vessel were evaluated using a discrete frequency sweep, with characterization at frequencies of 0.32, 1.00, 3.18, 10.00, and 31.80 Hz at a mean stretch of $1.05 * \lambda_{IV}$ and a stretch amplitude of $0.05 * \lambda_{IV}$ (Figure 9). This corresponds with peak characterization strain rates of 0.1, 0.3, 1.0, 3.1, and 10.0 s^{-1} . We also explored the influence of higher rates in the characterization process, but instabilities in the voice coil controller at these rates rendered the data useless. Vessels remained perfused with PBS but were unpressurized during oscillations. Arteries were immersed in PBS for the slowest (0.32 Hz) oscillations. The bath was drained for all higher-frequency oscillations to avoid interference between the artery and surrounding media. Arteries were out of the bath for approximately 70 seconds.

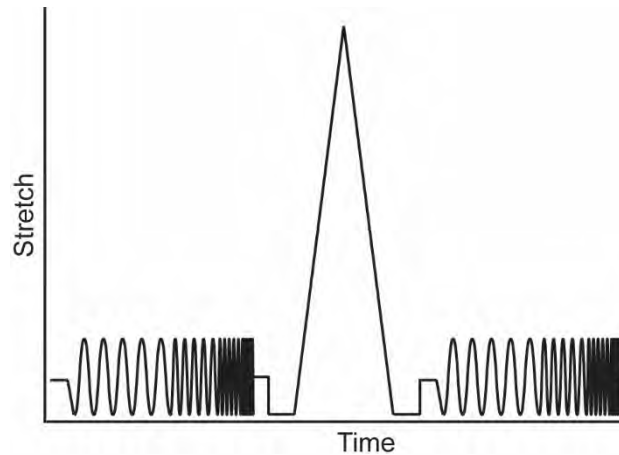


Figure 9 Schematic loading protocol (not to scale) showing the stretch profile used for baseline characterization of tissue at increasing frequencies before and after a triangle-wave overstretch curve.

Immediately following baseline characterizations, the vessels were overstretched to a targeted sub-failure stretch level ($\lambda_{IV} * 1.1, 1.2, 1.3, \text{ or } 1.4$) at a targeted strain rate ($\dot{\lambda} = 0.05, .5, 5, \text{ or } 50 \text{ s}^{-1}$) in an unpressurized state. The 0.05 s^{-1} samples were immersed in PBS during the test to prevent dehydration, but the bath was drained for the higher rate groups. The arteries were buckled to a stretch of 0.8, stretched to the targeted overstretch level, and immediately returned to buckled configuration. After overstretch, the vessel's baseline viscoelastic characterization was repeated.

2.4 Mechanical tester

The mechanical tester was custom-built for high-rate oscillations and overstretch (Figure 10). Similar to our previously described horizontal tester [30], the vessels were mounted to cannulas immersed in a PBS bath. One cannula was attached to a LabVIEW (National Instruments, Austin, TX) controlled syringe pump to drive preconditioning

pressures. The readings from pressure transducers on either side of the vessel were averaged to calculate luminal pressure. One cannula was mounted to a load cell assembly where a piezoelectric load cell (208C01, PCB Piezotronics, Depew, NY) was serially mounted to the proximal end of a strain-gauge load cell (model 31 250g, Honeywell). The load cell assembly was fixed to an X-Y stage (used to align the cannulas) mounted to a custom vibration isolator (a 3.58 kg aluminum block mounted on vibration isolators, VIB100-0205, Newport Corporation, Irvine, CA). The other cannula was attached to a voice coil linear actuator (LAS16-23-000A, Sensata Technologies, Attleboro, MA). The voice coil was controlled by an analog PID controller (412CE, Copley Controls, Canton, MA) tasked with following a waveform output by the custom LabVIEW program via an analog pin on a multifunction I/O device (USB-6001, National Instruments).

Displacement was recorded by sampling a Hall sensor built into the voice coil. Shims were used to create a mechanical stop to prevent overshoot in the high-rate (100 s^{-1}) overstretch ramps. Triangle waves were output to drive the overstretch displacements, with the loading and unloading velocities equal. All data were recorded with a data acquisition card (SCXI 1520, National Instruments) and sequentially digitized with a scanning multiplexer (SCXI 1600, National Instruments). Data were recorded at 100 times the oscillation frequency for harmonic oscillations and 800 times the strain rate for the overstretch ramps. High rate video was recorded with a Chronos 1.4, (Kron Technologies, Burnaby, Canada).

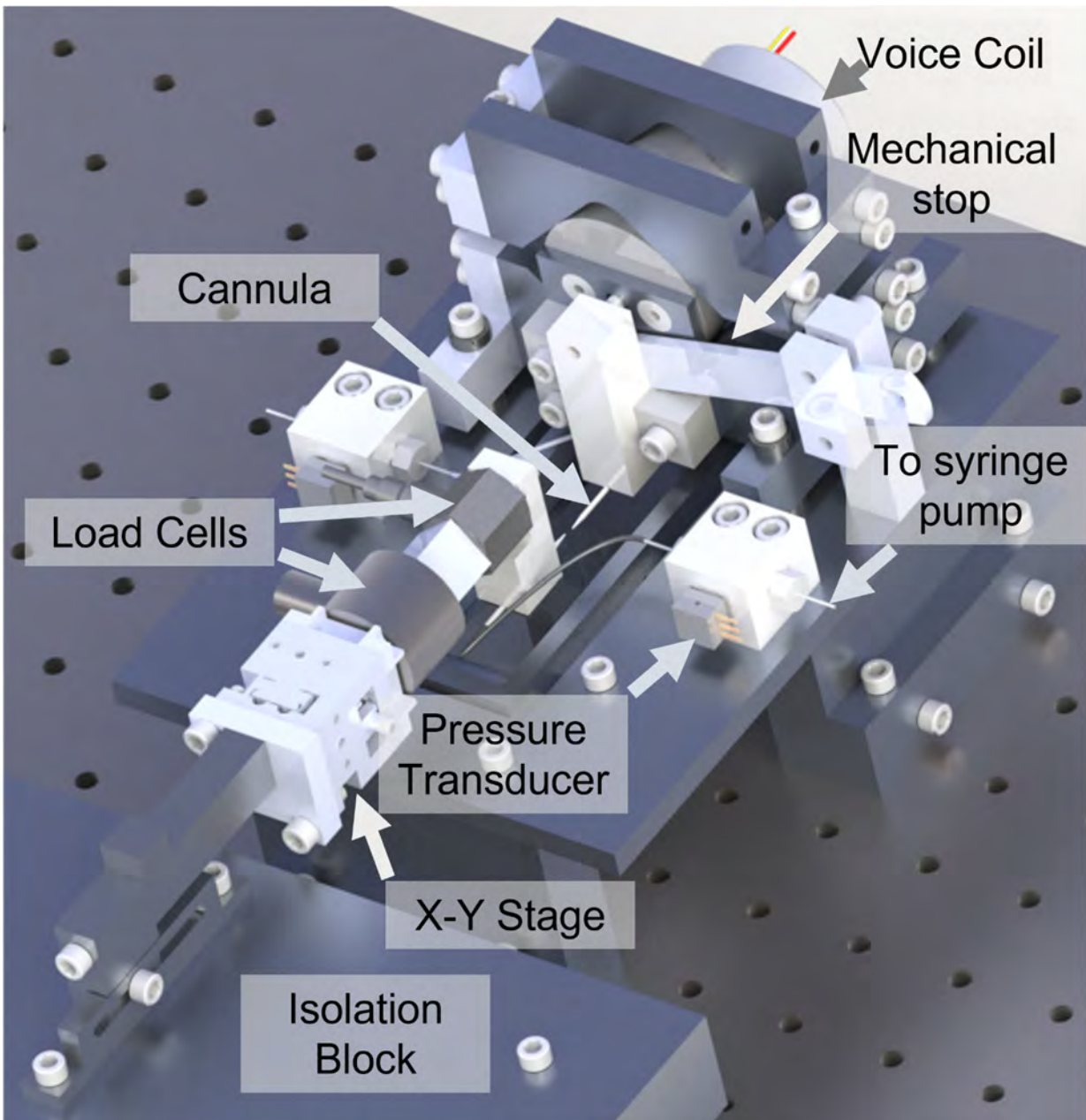


Figure 10 Custom high-rate tester configured for the highest rate tests (notice the mechanical stop extending toward the voice coil).

2.5 Mechanical analysis

The axial first Piola-Kirchoff stress P_{zz} , calculated as F/A where F is the current axial force, and A is the reference cross-sectional area, was used for uniaxial stress analysis. Axial stretch λ_z was calculated from suture-to-suture measurements. Dynamic modulus k was calculated using the peak-to-peak stress-strain values of the first cycle of each characterization frequency f defined as $k_f = \Delta P_{zz} / \Delta \lambda_z$. The strain-gauge load cell was used for all calculations, although we verified that the piezoelectric and strain-gauge load signals were not different at the tested frequencies using our previously published transform function [30].

We defined a reduction factor $(1 - d_f)$ at each frequency as that frequency's dynamic modulus in the post-overstretch characterization divided by the dynamic modulus of the baseline characterization such that $(1 - d_f) = k_{f,post} / k_{f,pre}$ where subscripts *pre* and *post* indicate pre-overstretch and post-overstretch characterizations, respectively. A linear regression was fit to the sample-average damage term $d = \frac{1}{n} \sum_{f=1}^n d_f$ as a function of overstretch magnitude for all samples. The fit was extrapolated to the point where $d = 0$ to identify an initial a damage threshold $\lambda_{p,0}$ above which we expect softening.

2.6 Molecular damage evaluation

Following mechanical testing, molecular damage was quantified by staining samples with CHP using a procedure similar to that previously published [39]. Samples were removed from the tester and stored in PBS at 4°C until staining (initiated within 24 hours of testing). The samples were immersed in 100 μ L of 20 μ M F-CHP (5-FAM

conjugate) for 12-18 hours at 4°C under mild agitation and then rinsed three times in phosphate-buffered saline for 10 minutes to clear unbound CHP. The central region of the artery samples was isolated to eliminate end effects, rinsed in deionized water, mounted onto a microscope slide, dried, and embedded in mounting gel.

CHP binding was detected with a confocal microscope (FV1000, Olympus Corporation, Tokyo, Japan) using a 488 nm Argon gas laser with 2 μm z-stacks. The brightest slice in the adventitia was used to quantify the CHP, and denaturation was quantified as the percent of pixels brighter than two standard deviations above the mean of the control sample intensity [Chapter 4]. An in-house masking algorithm was used to remove artifacts automatically. The number of bright pixels was then normalized by the two-dimensional area (in pixels) to allow comparison between samples.

2.7 Statistical analysis

To ensure we were observing rate-stiffening effects during our baseline characterization, repeated measures ANOVA was used to identify significant differences in k_f across the different frequencies for each pre- and post-overstretch characterization. As Mauchly's test showed a violation of sphericity, a Greenhouse-Geisser correction was used to calculate the p-value. A Tukey-Kramer *post hoc* test evaluated inter-frequency changes in significance.

While specific overstretches were targeted during experiments, slight variations in artery *in vivo* lengths (determined during *post hoc* analysis) led to a continuum of overstretches rather than precisely defined bins. As a result, we used linear regression to evaluate the effect of independent variables on the measured

softening of the artery. A multiple linear regression was fit to the data using softening as the dependent variable. Strain rate, max stretch, and evaluation frequency were independent variables. Multiplicative interaction terms were added between the independent variables to capture the effect of interactions. A p-value assessing the likelihood that a given fit parameter was not equal to zero was calculated for each term using the t statistic. Similarly, a regression confirmed significant rate stiffening in the overstretch curves. It was fit to the stress corresponding to a stretch of 1.2 as a function of the log of strain rate.

3. Results

3.1 Baseline characterization

The arteries demonstrated rate-dependent stiffening during the pre-overstretch baseline characterization (Figure 11a). Repeated measures ANOVA showed that this was statistically significant ($p = 0.022$), and *post hoc* analysis showed significant stiffening between each of the different groups ($p < 0.001$). Samples stiffened an average of 44.2% between the lowest and highest frequencies evaluated (Figure 11b) in a concave-up manner.

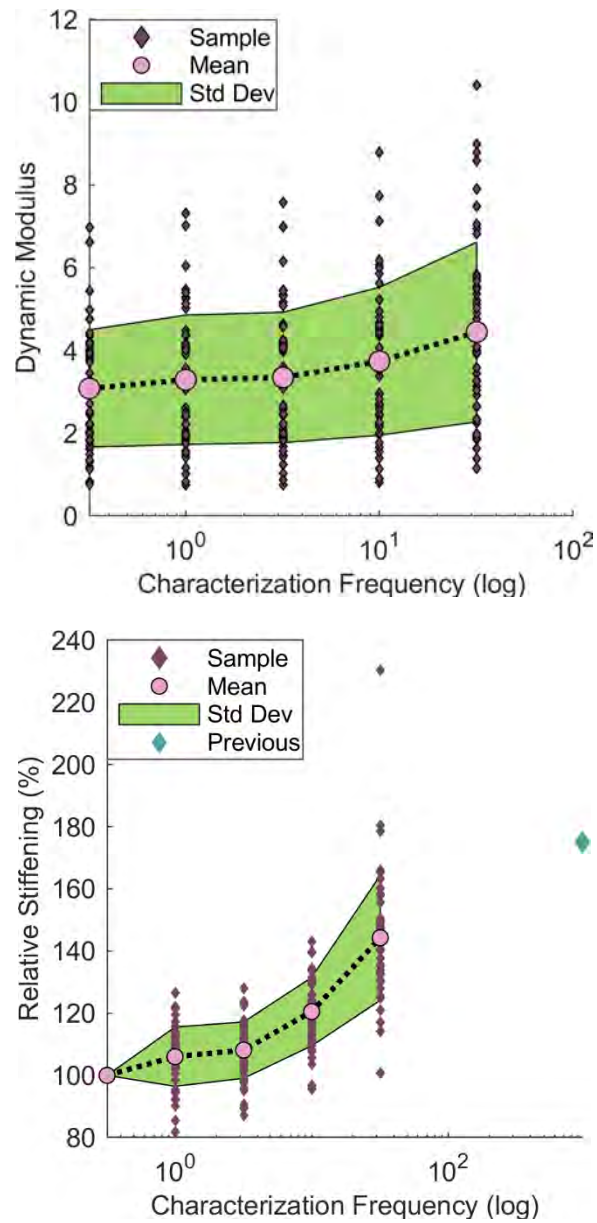


Figure 11 (a) Baseline (before overstretch) dynamic modulus for all samples. (b) Dynamic modulus normalized to the lowest frequency response. The percent change in failure stress determined in previous work [107] is included for comparison at the location approximate to what would be the equivalent frequency (based on maximum oscillatory strain rate).

3.2 Overstretch

The overstretch curves demonstrated the typical two-part, exponential-linear, behavior of arteries (Figure 12). They also demonstrated clear rate stiffening both visually and statistically ($p < 0.001$). As noted, overstretch strains and strain rates deviated slightly from the targeted values, especially at the highest rate (Table 2). For the highest rate group (50 s^{-1}), noise from contact with the mechanical stop is evident. Furthermore, there was clear relaxation as the voice coil slowed in anticipation of the stop. Note that this late softening of the highest rate curves is not related to yielding; in fact, we did not reliably observe clear yielding, defined by a sustained change in the convexity of the stress-stretch curve, in any of the overstretch curves. Additionally, while the actuator immediately began on the unloading path once reaching the target displacement in the 0.05 through 5 s^{-1} tests, it briefly lingered ($8.99 \pm 1.26 \text{ ms}$) at the maximum position before returning in the 50 s^{-1} tests.

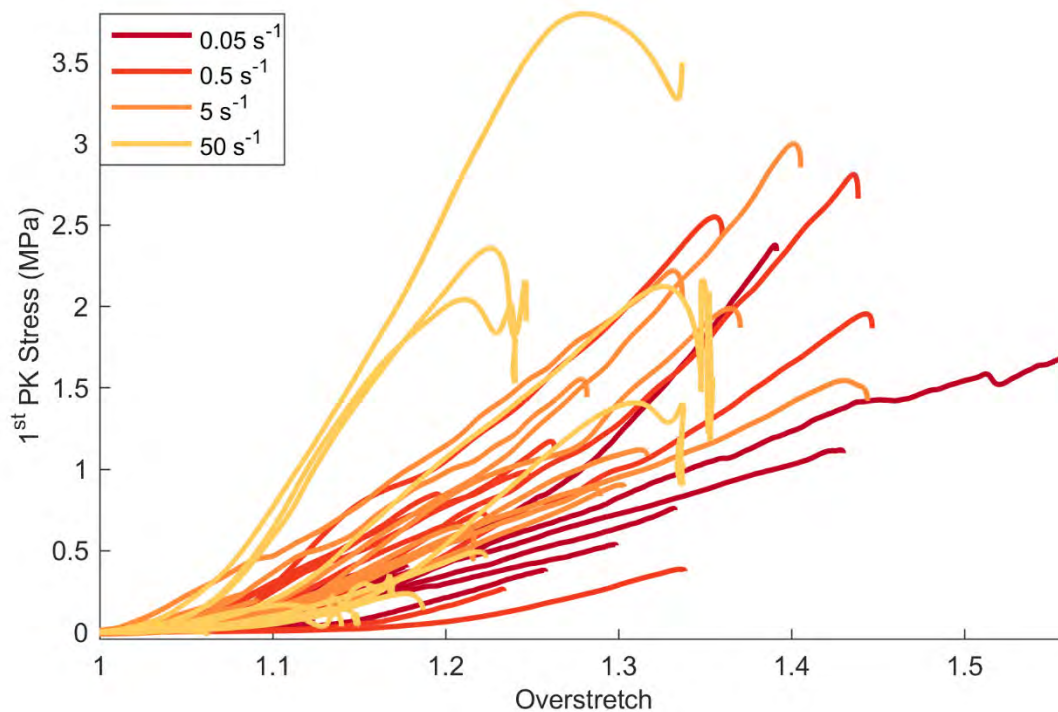


Figure 12 Overstretch curves demonstrate rate stiffening.

Table 2 Targeted and actual strain rates for each overstretch rate group.

Target Strain Rate (s^{-1})	Achieved strain rate (s^{-1}) (Mean \pm std)
5×10^{-2}	$(5.44 \pm 0.94) \times 10^{-2}$
5×10^{-1}	$(4.50 \pm 1.53) \times 10^{-1}$
5×10^0	$(4.22 \pm 1.99) \times 10^0$
5×10^1	$(5.31 \pm 1.20) \times 10^1$

3.3 Mechanical Softening

Softening of the vessels showed a clear trend with increasing overstretch, but there appeared to be no dependence on overstretch rate (Figure 13). The influence of overstretch appeared to be linear, with softening occurring at all deformations beyond the maximum characterization stretch. Tests targeting the maximum overstretch of 1.4 resulted in stiffness values as low as 10% of their pre-overstretch value. Sham vessels also showed a degree of softening between the pre- and post-overstretch responses, softening an average of $8.5 \pm 6.4\%$ (mean \pm std). An overstretch-dependent softening regression was fit to the data to identify both the damage threshold and the slope for the softening evolution (Figure 13). Our regression crosses the damage threshold λ_p at 1.05 ± 0.025 (mean \pm 95% confidence), meaning that an overstretch of $1.05 * \lambda_{IV}$ would be expected to initiate softening. The slope of the regression was found to be 2.73 ± 0.31 (mean \pm 95% confidence).

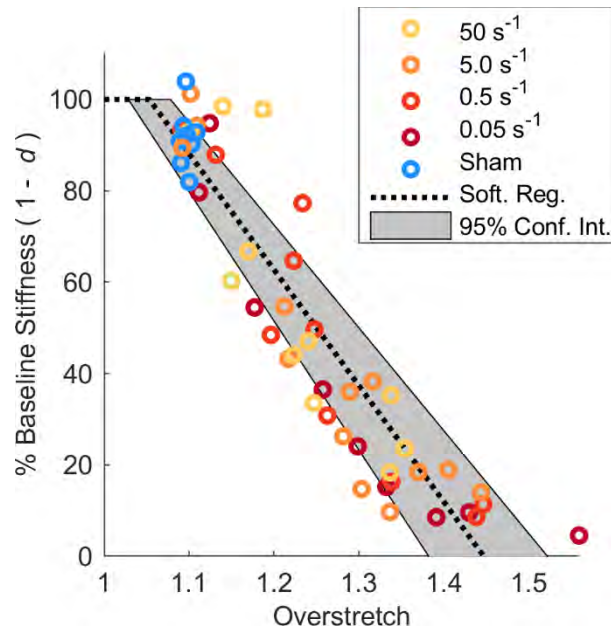


Figure 13 Mean (i.e., averaged over all characterization rates) percent change in baseline stiffness as a function of *in vivo*-normalized overstretch and overstretch rate. The plot shows that softening is a linear function of overstretch (beyond the threshold shown) and that rate of overstretch did not play a significant role. The fit reduction factor ($1 - d$) is plotted past the initial damage threshold $\lambda_{p,0}$. The shaded area represents 95% confidence intervals. Note that sham vessels have been placed at the maximum characterization stretch ($\lambda = 1.10$).

Results further show that softening did not repeatably change across characterization frequency with different rates of overstretch, as evidenced by the absence of any repeatable slope in the frequency-softening lines seen in Figure 14. Evaluation of the softening data using a multiple linear regression model found that only the max stretch ($p=0.008$) and offset parameters ($p=0.001$) significantly influenced softening (Table 3), reinforcing the visually identified conclusion that rate of overstretch and rate of characterization were not implicated in softening.

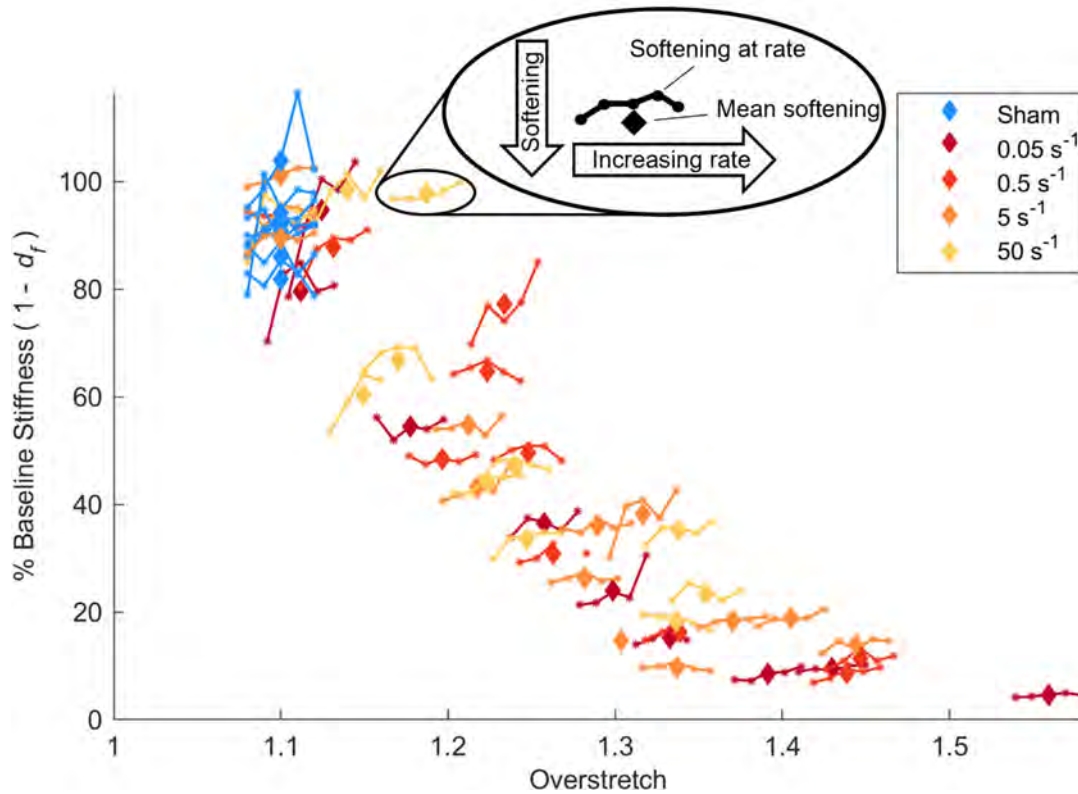


Figure 14 Softening as a function of overstretch, overstretch rate, and characterization frequency. Sample lines represent the degree of softening at each tested frequency, where the far left and right sides of each line are the amounts of softening observed with the 0.318 and 13.8 Hz recharacterizations, respectively. Line color corresponds with targeted rate of overstretch, and diamonds represent the mean softening across all frequencies. Note that a few of the samples have unconnected characterization points that correspond with data acquisition failures.

Table 3 P-values assessing the likelihood that a parameter value is statistically equal to zero for a multiple linear regression model. Statistically significant parameters are bolded.

Parameter	P value
Strain rate	0.865
Max stretch	0.008
Evaluation frequency	0.955
Strain rate * Max stretch	0.875
Max stretch * Evaluation frequency	0.987
Strain rate * Evaluation frequency	0.914
Strain rate * Max stretch * Evaluation frequency	0.913
Offset	0.001

3.4 Tropocollagen denaturation

Confocal microscopy of collagen hybridizing peptide binding to the tissue showed no consistent pattern in tropocollagen denaturation as a function of either magnitude or rate of overstretch (Figure 15). While approximately half of the samples (47.7%) did not have any more CHP expression than their paired controls, even fewer (26.2%) exhibited more than the range of sham samples (4.673 +/- 5.78 %BP). It is worth noting that two higher-expression samples skew the sham samples (the median value for sham vessels is 2.73 %BP). Quasi-static and high-rate failure data from our previous paper are included

in the plot for comparison. The stress-stretch curves of several of the samples with unexpected CHP expression are plotted in Figure 16 to show that unusual CHP expression is not associated with unusual mechanics.

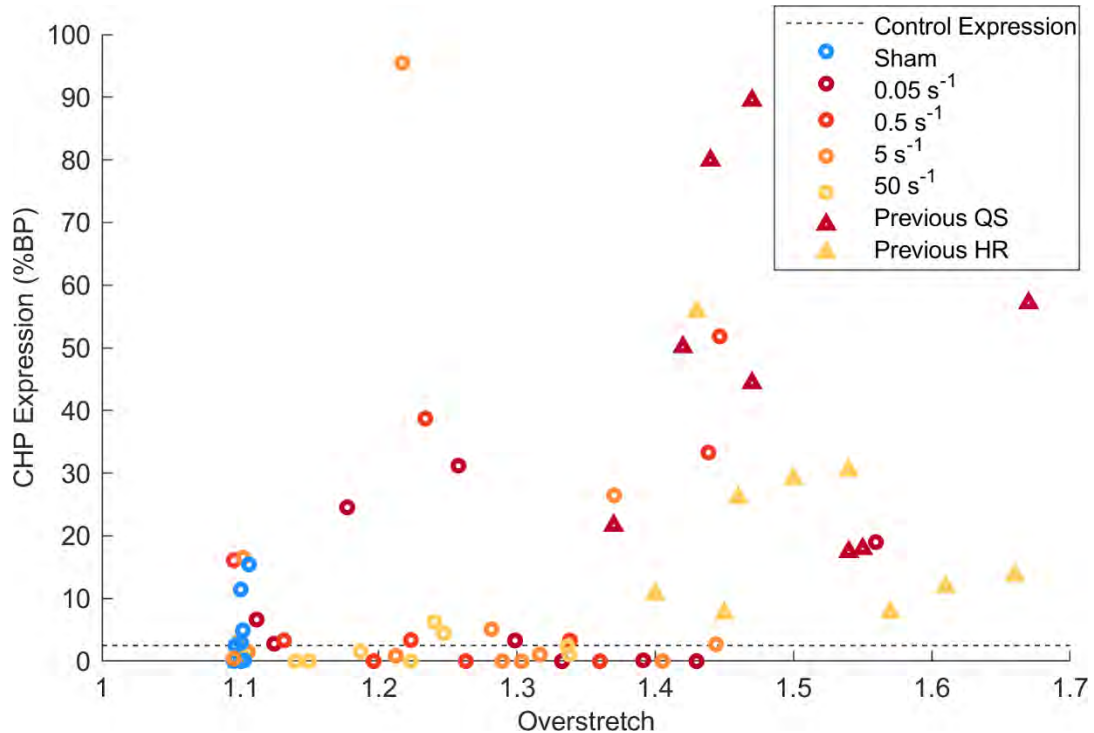


Figure 15 CHP expression in arteries as a function of overstretch. For reference, 2.5% BP (dashed horizontal line) is expected in the control vessels. Note that the included quasi-static (QS) and high rate (HR) failure values were not collected as part of this study. They are previously published data [Chapter 4] and are included here as a reference for comparison.

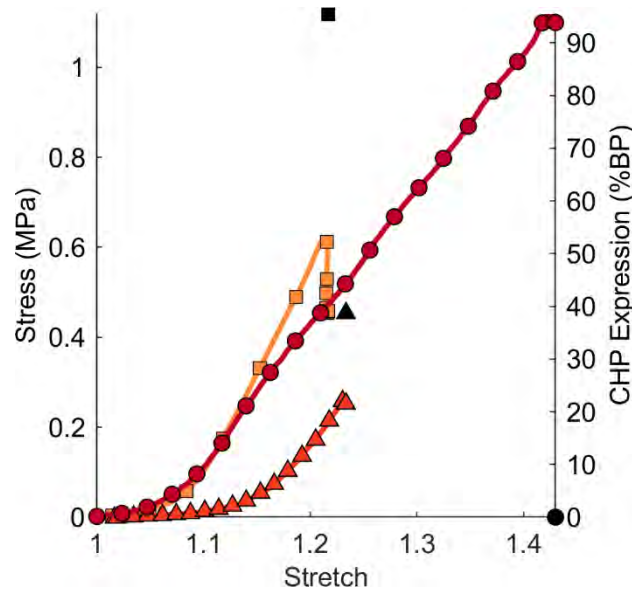


Figure 16 Three representative stress-stretch curves (colored) at different strain rates of samples with unexpected CHP signal (matching shape, black). These curves do not show atypical mechanics that explain the unusual CHP expression.

4. Discussion

One objective of this paper was to evaluate the influence of overstretch rate in the softening of cerebral arteries, including whether rate would selectively soften equilibrium versus non-equilibrium material behavior after overstretch. We also tested the hypothesis that the nature of overstretch-induced collagen damage would transition from tropocollagen to other elements of the collagen superstructure as overstretch rate increased. Our findings show that softening, while dependent on overstretch magnitude, is not dependent on overstretch rate and that the resulting softening affects the equilibrium and non-equilibrium components of vessel mechanical behavior equally. Our

results also suggest that tropocollagen denaturation does not play a substantial role in softening at the deformations considered here, suggesting that some other feature(s) of collagen are altered by overstretch to cause the softening response.

4.1 Mechanical Softening

The dependence of softening on the magnitude of overstretch, its independence on rate of overstretch, and the equivalent progression of softening in both the quasi-static and high rate responses together facilitate simple formulations of continuum damage models. More specifically, these results indicate that a single damage parameter, with a simple evolution function, can model the softening of the tissue for both the equilibrium and non-equilibrium components of a hyper-viscoelastic damage model. There are few visco-hyperelastic damage models for soft tissue and even fewer that have been directly fit to experimental data. Most of the proposed models that account for softening are already formulated in a manner consistent with our findings, e.g., [42, 71, 100]. As an example, one could apply damage to our previously published (hyperelastic) model [107] by modifying the shear stress parameter μ and fiber stiffness parameter k_1 by the reduction term $(1 - d)$. As viscoelastic stiffening is dependent upon elastic stress rate, softening will implicitly be applied to the time-dependent response of the tissue.

While we believe this is the first study to measure changes to the viscoelastic properties of collagenous tissue following overstretch at various rates, our results seem to agree with those of Panjabi *et al.* [103], who found a similar decrease in both the serial spring and the parallel dashpot coefficients in a 3-element Kelvin-Voigt standard linear solid model representing rabbit ACL following high rate overstretch. The present data

also agree with Duenwald-Kuehl *et al.*, who found a high correlation between the decrease in maximum stress and the magnitude of stress relaxation in porcine flexor tendons, indicating that the equilibrium and non-equilibrium components softened equally [104]. In contrast, our results are different from those of Kurz *et al.*, who noted significantly increased alteration of the high-rate response of cartilage as overstretch rate increased compared with the quasi-static response of the tissue [105]. However, it should be noted that they found a statistically insignificant decrease in the equilibrium stiffness as overstretch rate increased. Furthermore, findings from compressive damage in cartilage may not be highly informative to the mechanics of arteries, as loading in cartilage is generally assumed compressive [126].

Softening was identified in sham vessels not stretched past the maximum characterization stretch, indicating that some softening was induced during the characterization process. Indeed, the softening regression indicates that the damage threshold was only slightly above the *in vivo* length. We did not directly measure the softening threshold; extrapolation of the regression to the undamaged (baseline) response was used to identify the damage threshold λ_p . This technique may be less precise than a series of tests in the near-damage regime to precisely identify the location of λ_p , but we suspect variability between samples would make identification of λ_p through testing similarly imprecise. While this damage threshold is very close to the physiologic stretch of the vessel, it is in line with previous literature. Bell *et al.* found 18.5% softening in the *in vivo* stiffness of ovine MCAs stretched to 1.1 times the *in vivo* length [26], almost precisely the 18.4% softening predicted by our regression at the same stretch.

Furthermore, Bell *et al.* allowed the vessels to recover for up to 60 min post-overstretch and did not observe any measurable recovery of mechanical properties, indicating that the identified damage threshold is a result of a permanent material reorganization rather than recoverable time-dependent processes such as poroelasticity. The proximity of the damage threshold to the *in vivo* stretch emphasizes the importance of conservative preconditioning protocols; that is, it is clear that deformations even slightly beyond the *in vivo* stretch initiate softening.

4.2 Tropocollagen Denaturation

Tropocollagen denaturation as a result of mechanical overstretch was not readily identified in this study. Although this statement may not be immediately evident in Figure 15, closer examination shows that the few large values attract the eye while most of the samples are very close to control values. CHP is a rather noisy marker for damage, as indicated by the signal-to-noise ratio of previous CHP work in arteries [39]. As such, the CHP expression in the sham vessels (and the few samples with elevated expression) is likely a manifestation of CHP variance. In fact, while the sham vessels show slightly elevated levels of CHP expression, the median value of sham CHP is only a quarter of a percent higher than the methods-defined expression of the undamaged controls (2.5%).

While it may be initially surprising that we observed such extreme softening values in the absence of tropocollagen delamination, the findings are consistent with the previously reported association between CHP onset and yielding in ovine MCAs [38, 39] as well as rat tendon [113, 127]. It appears that these porcine vessels have a similarly high threshold for consistent molecular unfolding; our current data support Converse *et*

al.'s unfolding stretch threshold of 1.4 in ovine tissue [39], followed by a subsequent increase in CHP expression up to the point of failure, a stretch of approximately 1.45 and 1.53 at quasi-static and high rates, respectively (referring to the previously reported failure data [107]). There was no clear yielding in the current overstretch curves, but we expect that a yield point would be identified near a stretch of 1.4, consistent with our approximate CHP threshold and the yield point of ovine MCAs [39].

The lack of CHP signal seen here could be due to limitations of current CHP detection methodologies, as highlighted in [39] [Chapter 4]. However, consideration of a number of alternative methods, such as the microplate assay suggested by Lin [114], did not improve sensitivity in small arteries such as those presently explored. In any case, our presently identified CHP expression is remarkably muted compared to the data collected from failure samples of the same tissue [Chapter 4].

The lack of tropocollagen denaturation at the sub-yield overstretch studied here suggests that some other element of the collagen hierarchy must be responsible for the dramatic softening observed. Intrafibrillar bonds (covalent enzymatic cross-links) are a step above tropocollagen in the collagen hierarchy. Fracture of these bonds is possible; however, we would expect tropocollagen denaturation in the degradation of fibrillar integrity as fibrillar tropocollagen is unstable outside of the fibril [67], thus likely ruling out dissociation of fibril structure. Another possible location for molecular-level damage is the interfibrillar proteoglycan bridges. Proteoglycans bind collagen fibrils together to form fibers. Others have theorized that proteoglycans are primarily responsible for the softening of arteries [8, 14, 16] and other soft tissues [117, 128]. These theories, however, are controversial [96] and have yet to be substantially reinforced by direct experimental

observations of proteoglycan or glycosaminoglycan disruption following mechanical overload [38]. Reese *et al.* noted that hydrogels synthesized in either the presence of decorin or just the decorin core protein maintain a stiffness approximately twice that of hydrogels grown in the absence of decorin [129], implying a mechanical role of the interfibrillar proteoglycan. On the other hand, Fessel and Snedeker found no change in stiffness following glycosaminoglycan depletion in tendons; however, they did not directly image proteoglycans [130], and depletion of the glycosaminoglycans does not necessarily affect the protein backbones. Two mechanisms have been proposed by which interfibrillar proteoglycans lead to inelastic mechanics: slippage and debonding. The slippage theory is predicated on the idea that proteoglycans adhere together via weak hydrogen bonds that disassociate in a “sliding filament mechanism” [14, 16]. This slippage would “soften” the material by elongating the collagen fibers, increasing the permanent set of each fiber. Alternatively, the debonding theory speculates that the protein backbone of proteoglycans is fully separated from the collagen fibril itself, decreasing the fiber’s focal stiffness at the debonded proteoglycans’ location [117]. Note that these two theories are not necessarily mutually exclusive. The slippage theory could be an inelastic mechanism during quasi-static overstretching when there is sufficient time to reorganize the molecular structure, while debonding may be the dominant damage mechanism at high rates when there is not enough time to dissociate the hydrogen bonds, leading to a stiffened sliding response and inducing failure at the protein root. Another principal constituent in artery walls is elastin; however, recently reported work from our lab has suggested that direct observations of internal elastic lamina failure do not

correspond with a marked change in the stress-stretch curve at the point of lamina failure [47].

We recommend that future efforts focus on interfibrillar cross-links as the most likely connection between microstructural disruption and softening; however, continued investigation of tropocollagen denaturation is essential to fully define its role in mechanical damage.

4.3 Rate-Dependent Stiffening

Another valuable contribution of this work is a more detailed characterization of viscoelastic stiffening. This work identifies significant rate stiffening at a lower threshold than previously reported [107] in the same tissue. This is likely due to improvements in methodology, as the signal-to-noise ratio of the presently reported tester is substantially better than that of the previous work, and the actuator motion at high strain rates is smoother in the current report. Furthermore, given that the samples are self-referential (repeated measures), the statistical analysis is cleaner in the current experiment.

We evaluated several decades of strain rate in the present work, filling in the lower end of the gap between rates in our previous study [107]. At the rates studied here, the tissue rate stiffened in a concave-up manner as a function of the log of characterization strain rate, to an amount of about 140% at 10 s^{-1} . Our previous work reported strain rate effects on tests to failure, so they are not directly comparable to the much smaller characterization strains reported here, but the ratio of high-rate (300 s^{-1}) to quasi-static failure stress in that study was approximately 175%. Extending the trend of the current data to this strain rate would result in significantly higher relative stiffening

values, suggesting that a change in concavity would be required (Figure 11). This change in concavity is consistent with a continuous relaxation spectrum applied within the framework of quasi-linear viscoelasticity, where it is expected that stiffening plotted against the log of strain rate will lead to a sigmoid function [41, 85]. In fact, our data suggest that the lowest frequency is close to the lower asymptote of the function, verifying that it is truly a quasi-static test. However, we need more data on the upper end of the spectrum to define the upper asymptote and the cutoff frequency.

4.4 Connecting softening and ECM alterations

This study contributes to the current state of knowledge of coupled microstructure and mechanical damage in blood vessels and other soft, collagenous tissues. As visualized in Figure 17, cerebral arteries pass through a large loading regime where an unknown mechanism leads to substantial softening, prior to the initiation of tropocollagen denaturation. The shape and rate dependence of the softening curve beyond the yield point are unknown. Note that the threshold for tropocollagen denaturation and final rupture are strain rate dependent. It is presently unclear if the rate-dependent unfolding mechanisms decrease the failure stretch or if the reduced failure stretch reduces the amount of tropocollagen that experience a large enough deformation to initiate delamination.

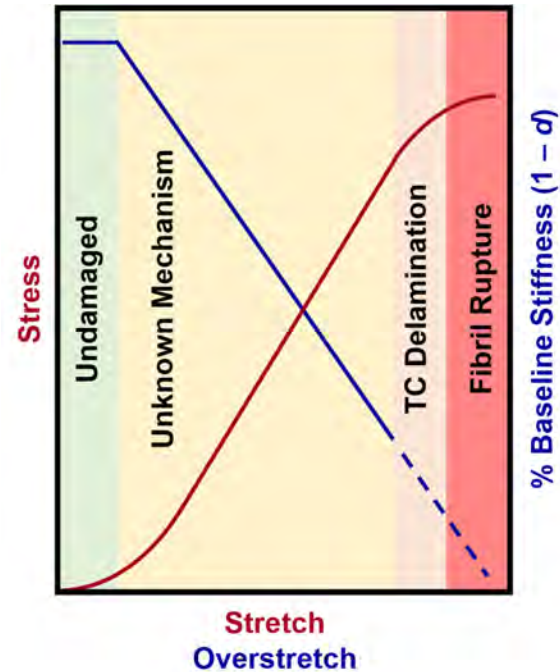


Figure 17 Proposed relationship between ECM alteration and softening. Note that tropocollagen delamination begins at the yield point, yet substantial softening due to some yet-unknown mechanism is identified at sub-yield deformations. The solid portion of the softening curve applies to both the equilibrium and non-equilibrium components of the material response following a single overstretch at any deformation rate. The shape of the dashed portion of the softening line is unknown. It is also unclear whether softening in the post-yield regime is rate dependent.

4.5 Limitations

The interpretation of these results should be considered with several limitations in mind. First, we used dynamic modulus, calculated using peak-to-peak stress and strain values, to characterize tissue behavior and quantify softening at a near-physiologic stretch. This stretch range does not allow us to address any increases in stretch at physiological stress following the overstretch protocol, such as that observed by Bell *et al.* [26]. While it is not presently known whether cerebral arteries return to their original

stretch or stress following overstretch, we anticipate that the lack of rate-induced changes in compliance will apply to both stretch- and load-controlled situations. It should also be noted that the specified version of dynamic modulus approximates the stress-strain response as linear. This is obviously inaccurate as a representation of vessel behavior, but it does provide a simple, accurate quantification of softening in the tissue.

Second, overstretch curves were not ideal but included acceleration and deceleration, especially at high strain rates, similar to our previously reported experimental limitations [107]. The effects of this acceleration were primarily mitigated by slightly buckling the vessels before accelerating the fixturing, allowing most of the acceleration to happen before reaching the *in vivo* length. A mechanical stop was placed at the highest strain rates to prevent samples from passing their target overstretch value. From this point, the voice coil actuator had to accelerate back to the unloaded configuration, causing the highest-rate vessels to experience more time at the maximum strain relative to the total test time than the rest of the samples. To ensure this was not a factor in our results, we calculated the strain-time integrals for each sample. Strain-time integral values were distinct, by an order of magnitude, between groups having the same stretch values but different rates.

We have previously written an exhaustive summary of limitations associated with the CHP methodology [Chapter 4]; however, it is worth highlighting that CHP is still a noisy marker of tropocollagen denaturation in small arteries. These limitations have been overcome in rat-tail tendon fascicles by the use of a microplate assay, as proposed by Lin *et al.* [114]. Regardless of the sensitivity of the CHP assay, researchers need to be careful

when recording a single marker of damage, given that the collagen fiber is a heterogenous, hierarchical structure.

Our overstretch curves did not reliably pass a clear yield point, insinuating that our results do not apply to failure damage modeling. Given that Marino *et al.* demonstrated that tropocollagen denaturation closely mirrors the final failure (post-yield) progression of cerebral arteries [38], and our previous observation that tropocollagen denaturation progresses in a rate-sensitive manner, we believe that there may be a rate-sensitive change in the mechanical yield behavior of samples deformed beyond the yield point. Indeed, failure progression has been shown to be mechanically rate-sensitive in various tissues [10, 31, 80, 107]. As we did not reliably observe yielding, our current data do not dispute these conclusions.

Acknowledgements

Funding for this project was provided by the National Science Foundation (Award No. 2027367), with contributions from the Henry Jackson Foundation (Contract No. W81XWH-17-2-0008). We would like to thank Kolbi Dietmeier and J. Kevin Lee for their time spent imaging. We acknowledge Cell Imaging Core at the University of Utah for use of equipment (Olympus FV1000).

CHAPTER 6

EXPLORATORY INVESTIGATION OF ECM ALTERATIONS

1. Introduction

Understanding the locations of ECM alterations due to overstretch is crucial for developing therapeutics targets [15], identifying the root causes of dysfunctional ECM maintenance [131], and designing biomimetic materials [18, 19]. Previous research has demonstrated that tropocollagen denaturation is a common ECM alteration following severe mechanical injury [39], and that the severity of denaturation is dependent on the rate at which it occurs [Chapter 4]. The identification of tropocollagen denaturation as a failure point in the ECM is considered a substantial advancement in understanding how arteries ultimately fail [24]. However, it has been observed that the tissue softens dramatically following sub-yield overstretch that does not lead to tropocollagen denaturation, so the molecular changes responsible for this softening are currently not yet understood. Additionally, the rate-dependent nature of tropocollagen denaturation suggests the need to investigate other potential sites of ECM disruption that may be activated at high rates, such as the interfibrillar proteoglycan/glycosaminoglycan complex and intrafibrillar covalent/trivalent bonds. It is also possible that the observed rate dependence is due to heterogeneous loading at the fibril level.

The proteoglycan/GAG complex has long been speculated to be an important contributor to the mechanical response of tissue [14, 16, 128]. Many researchers have used GAG degradation to explore the influence of GAGs on tissue mechanics. The results of these studies are mixed, with some groups finding changes to the mechanical response [54, 55, 132] and others observing no effect [130]. However, there are relatively few studies that have directly imaged GAGs to monitor changes in their expression. Several methods, including nuclear magnetic resonance (NMR) imaging [14], Alcian blue staining [133, 134], and the absorbance dimethylmethylene blue (DMMB)-stained, digested tissue [105, 135], have been used to visualize GAGs in tissue. While the proteoglycan core has been shown to affect the mechanical response of the tissue [129], there are no known studies that have directly visualized proteoglycan core proteins following mechanical overstretch.

Electron microscopy (EM) has been widely used to examine the structure of collagen fibrils. It is a valuable tool for identifying changes such as loss of d-banding [37, 57], fibrillar kinking [33, 36], and the specific locations of gold nanoparticle conjugated CHP (NP-CHP) binding [37]. Imaging these structures after mechanical injury allows us to determine which structures have been damaged. For instance, the presence of disrupted d-banding without NP-CHP could indicate that the intrafibrillar crosslinks have failed or that tropocollagen has undergone molecular fracture (as opposed to delamination). On the other hand, if there are clear regions of NP-CHP concentration, this could indicate that heterogeneous loading at high strain rates is responsible for the decreased fluorescent CHP (F-CHP) signal observed.

We carried out a preliminary study to assess the effectiveness of two methods in identifying the potential cause of the rate-dependent decrease in tropocollagen denaturation that we previously observed. The first method that we explored was a DMMB assay to identify any dissociation of GAGs or proteoglycans with intact GAG chains. The second method we used was electron microscopy, specifically both scanning electron microscopy (SEM) and transmission electron microscopy (TEM). SEM provides clear visualization of fibril structure, but only images the surface of a sample, while TEM allows for observations of reflected gold nanoparticles. In this work, we failed cerebral arteries both quasi-statically and at high strain rate and then examined the tissue using a DMMB assay, SEM, or TEM. This work provides guidance for future research strategies.

2. Methods

2.1 DMMB

Testing: Anterior cerebral arteries (ACAs) (n=24) from eight Göttingen minipigs were resected and cleaned as described in previous chapters. Three samples were taken from each animal, with one sample assigned as a control and the other two used for testing. Tissue was axially failed at either quasi-static (0.01 s^{-1}) or high rate ($>100 \text{ s}^{-1}$) on the tester described in Chapter 5. After the test samples were failed, all samples were washed three times in PBS for 10 minutes under gentle agitation. They were then cut longitudinally, rinsed for five seconds in deionized water, and dehydrated on a glass slide for storage.

Assay: Samples were rehydrated in PBS for 15 minutes, and then digested in 200 μL of 1 mg/mL Proteinase K solution as described in Chapter 4. DMMB (Sigma-Aldrich,

Catalog # 341088) reagent and standards curve were prepared according to [136]. Absorbance was read in duplicate; following digestion, 100 μ L sample solution was combined with 100 μ L DMMB assay. The well plate was immediately shaken and read on a microplate reader (SpectraMax Gemini XPS, Molecular Devices, San Jose, CA).

Calculations: Absorbance was normalized by the two-dimensional area of each sample in the same manner as that outlined in Chapter 4. Normalized absorbance was compared between the control, quasi-static, and high-rate samples using a one-way ANOVA.

2.2 Electron Microscopy

All EM samples were porcine MCAs resected from heads purchased from a local slaughterhouse. Samples were resected and cleaned as described in previous chapters. They were axially failed either quasi-statically or at high strain rate in an unpressurized state using the tester and methods described in Chapter 3. After failure, samples were cut open longitudinally, placed in a solution of 2% paraformaldehyde and 2.5% EM-grade glutaraldehyde suspended in 0.1 M cacodylate buffer and fixed for a minimum of 12 hours. The preparation and electron microscopy were performed by Linda Nikolova (TEM) or Nancy Chandler (SEM) at the University of Utah Electron Microscopy Core Laboratory.

SEM: Three batches of samples were prepared for SEM imaging. The first batch was post-fixed in osmium tetroxide, dehydrated in a graded series of ethanol, and then dried with hexamethyldisilazane (HMDS) before being mounted on an SEM stub and surface coated with gold-palladium. The second batch was prepared the same except it

was critically point dried instead of being dried with HMDS. The third batch was processed using the O-T-O technique [137] to build heavy metals in the tissue, eliminating the need for surface coating. This set was exposed to thiocarbohydrazide (TCH) after the osmium tetroxide post-fixation, washed in deionized water, then re-exposed to osmium tetroxide. Samples were imaged at 15 kV on a Zeiss GeminiSEM 300 (Carl Zeiss Microscopy, LLC, White Plains, NY).

TEM: Samples were stained with tannic acid prior to three washes of osmium tetroxide. The preparation was continued with uranyl acetate and critically point dried. Tissue was washed in deionized water between each treatment. Samples were embedded in epoxy resin and sectioned to 70 nm thickness using an ultratome. The sections were mounted on grids and imaged on a FEI Tecnai T12 microscope (FEI, Hillsboro, OR) at 120 kV.

3. Results

3.1 DMMB

The DMMB assay yielded no changes between any of the three groups, both visually (Figure 18) and statistically ($p = 0.555$). The absorbance of the samples was close to the bottom of the standards curve. The GAG-free standard provided an absorbance of 1.69, while the samples gave a total absorbance of 1.76 ± 0.05 (mean \pm std). After adjusting absorbance by a line fit to the standards curve, the samples contained a GAG mass of $0.984 \pm 0.786 \mu\text{g}$, which was low on the standards curve that ranged from 0 to 10 μg of GAGs.



Figure 18 GAG content for controls and failed samples normalized by its two-dimensional area in million-pixels (Mpx).

3.2 Electron Microscopy

SEM: There were two major challenges with SEM imaging of the tissue: surface charging during imaging and tissue curling during preparation. Surface charging yielded poor contrast, making the identification of structures difficult (Figure 19). Surface charging persisted even after changing to the O-T-O technique. Furthermore, cracks formed on the batch of O-T-O samples while mounting to the stub, as the sample had to be flattened and the O-T-O treatment increased tissue brittleness.

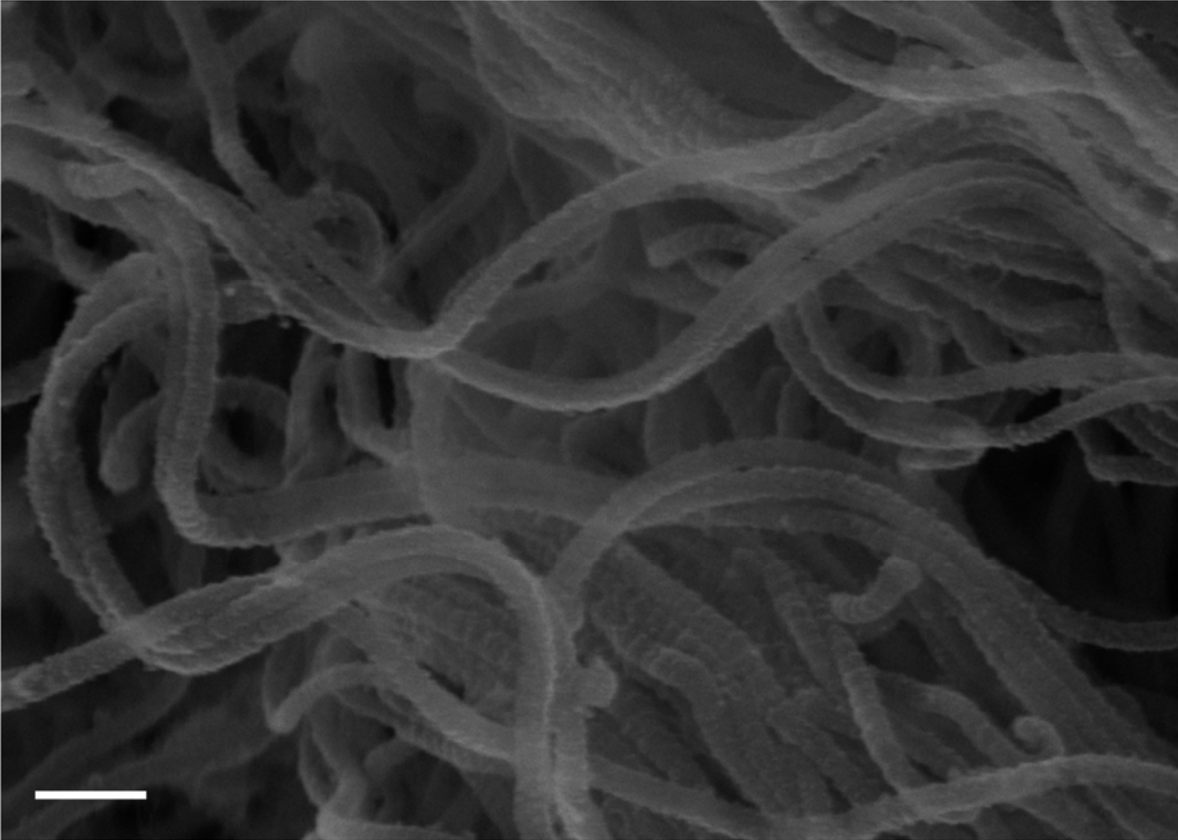


Figure 19 Representative SEM image of the adventitia of an MCA (50,000x, scale bar is 200 nm). While some fibrils show d-banding, it is challenging to view in most of the fibrils.

TEM: Curling of samples was the major limitation of TEM imaging. Tissue curled in an unpredictable manner, leading to challenges mounting the samples for consistent slicing on the ultratome. Specifically, it was challenging to identify which layer of the artery (media or adventitia) we were looking at in a given field of view, as there were no landmarks (Figure 20a). Furthermore, it was not possible to identify fibril ends, as the fibrils undulate in and out of plane. The contrast in TEM was noticeably better than in SEM (Figure 20b), with d-banding clearly evident.

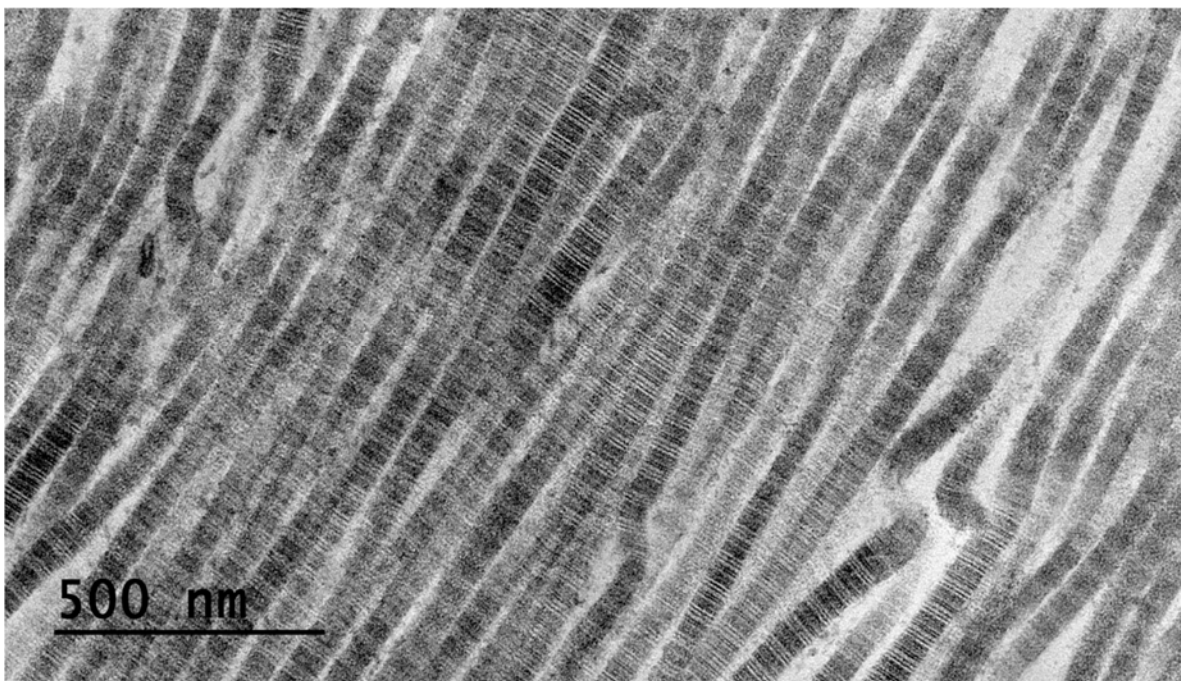
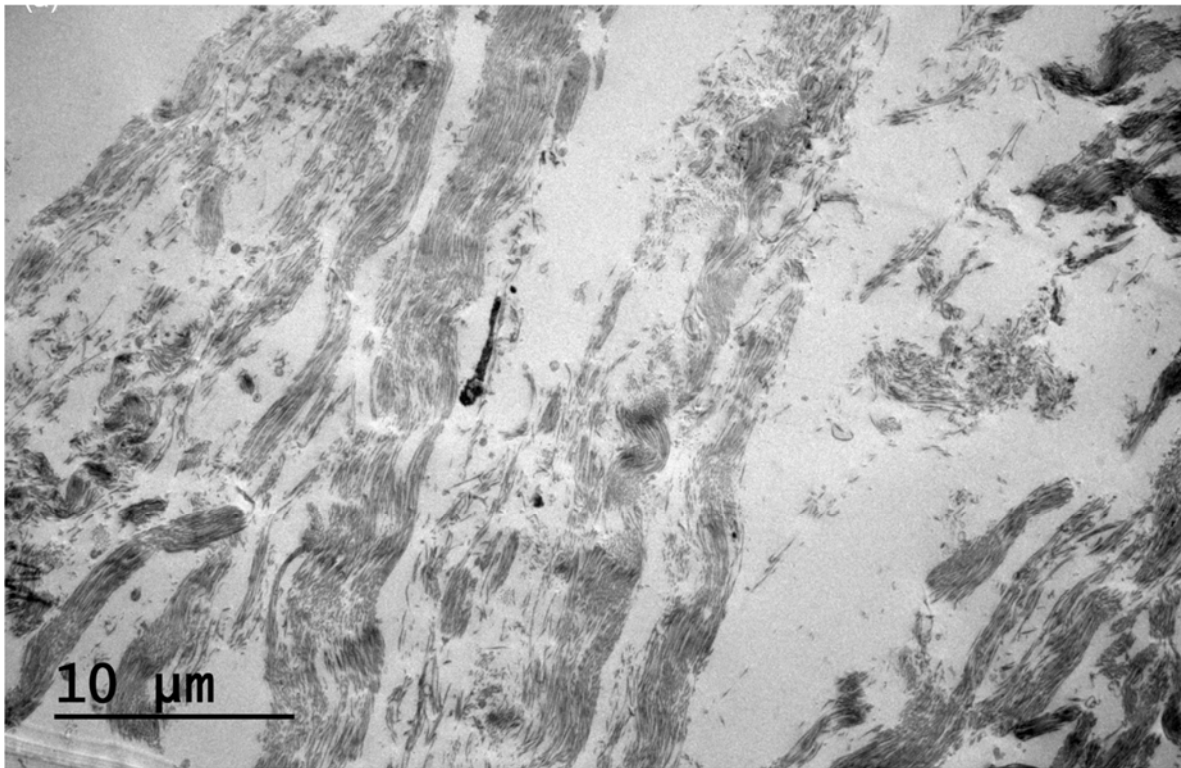


Figure 20 Representative TEM images of MCAs. (a) Low magnification (500x) image illustrating the absence of landmarks, making it difficult to determine the layer to which the fibers belong. (b) High magnification (12,000x) TEM image displaying clear d-banding in the fibers.

4. Discussion

The purpose of this preliminary study was to evaluate the effectiveness of multiple methods for detecting changes in the ECM resulting from mechanical injury. Unfortunately, we did not observe any positive results, but this work did provide valuable insights for future research efforts.

4.1 DMMB

The DMMB assay did not detect any evidence of GAG disassociation due to mechanical injury or rate. There are several reasons why we may not have observed GAG disruption using the DMMB assay in this study. The first, and possibly most obvious, is that GAGs may not be disassociated during mechanical overstretch. While this goes against some of the literature in cartilage [105, 138], it is consistent with several studies that do not find a strong relationship between GAG prevalence and tissue mechanical response [129, 130]. Another reason for the lack of GAG detection may be the strong negative charge maintained by GAG chains [54], which could inhibit the ability to wash any disassociated GAGs out of the tissue. One potential reason for the absence of a measurable effect is that the amount of GAGs in the tested tissue was already near the lower end of the standards curve. This means that even large relative changes in GAG content may result in only small absolute changes in absorbance, making it difficult to distinguish any effect from the background noise in the absorbance readings.

Based on the current findings, we do not think it is necessary to prioritize a DMMB-based assay for future research. While these findings do not conclusively rule out the possibility of GAGs being separated during mechanical injury, we believe there

are other research directions that would be more productive. One promising approach to explore the proteoglycan/GAG complex that has been successfully deployed in studying tendon is the use of plastic interfibrillar shear strain, as demonstrated by Szczesny and Elliot [128]. As proteoglycan/GAG complexes are the primary structure that binds adjacent fibrils [57], plastic interfibrillar strain can be interpreted as damage to the proteoglycan/GAG complex. Szczesny and Elliot used confocal microscopy to observe the overstretch-induced residual angles of a previously transverse photobleached line. However, the use of confocal microscopy has a limited spatial resolution, which makes it difficult to directly measure interfibrillar strains. We recommend using a multi-photon microscope to improve the spatial resolution and allow for more accurate measurement of interfibrillar residual strain in cerebral arteries.

4.2 Electron Microscopy

We encountered challenges with sample preparation during our electron microscopy of cerebral arteries. The arteries were thin (approx. 100 μm thick) and had a natural curl in both the circumferential and adventitial direction when cut open. The cross-linking that occurs during fixation appears to play a role, as samples were more deformed after the paraformaldehyde/glutaraldehyde fixation. These factors made it difficult to obtain successful images using EM.

One potential solution for this issue could be to use a more gradual dehydration process during sample preparation, as this has been shown to reduce the effects of chemical tension in samples during SEM preparations [139]. While previously tailored to SEM preparation, gradual dehydration could be successful in the preparation of TEM

samples. Another possibility is to fix and coat the tissue in a restrictive frame to prevent it from warping.

Preventing tissue warping would likely improve both TEM and SEM imaging. In TEM, it would be easier to identify the correct artery layer expected to be damaged, increasing confidence in the images and the likelihood of detecting failed fibrils. In SEM, flat tissue would conduct charge more efficiently, resulting in improved image contrast.

Although we still believe that electron microscopy has the potential to be a useful tool for studying the mechanism behind rate-dependent tropocollagen denaturation, we think it would be more efficient to collaborate with a laboratory that specializes in EM exploration of collagen ultrastructure rather than trying to develop these skills in-house. This would allow us to benefit from the expertise of others and focus on techniques that are unique to our own laboratory.

CHAPTER 7

INTERSPECIES DIFFERENCE IN CHP EXPRESSION

1. Introduction

The goal of studying tissue dysfunction in animals is to improve the treatment of human diseases [140]. Therefore, the most important methods decision to select an animal model that is representative of the disease states found in humans [141]. During testing in Chapter 4 we noticed a concerning difference between the porcine samples we were working with and a report by Converse *et al.*; ovine MCAs repeatedly experience IEL failure at high stretch while porcine MCAs do not. This unexpected finding prompted us to investigate the difference between CHP expression in ovine and Göttingen minipig MCAs that were quasi-statically pulled to failure in a preliminary study.

2. Methods

We compared the adventitial CHP expression of four ovine MCAs samples that were axially pulled to failure at quasi-static rates during Converse's doctoral work [142] with ten porcine samples axially failed (also quasi-statically) as part of the work described in Chapter 4. Since the CHP expression in Chapter 4 is calculated in a different way than the method used by Converse, we recalculated the CHP expression from

Chapter 4 using the same method as Converse. Specifically, we used a static threshold of two times the mean control intensity to identify the percent of bright pixels in the data from Chapter 4. A student's t-test comparing the mean CHP expression was used to evaluate significant differences between the animals, with a p value below 0.05 considered significant.

3. Results

The p-value between species was 0.064, which is below our *a priori* significance threshold.

4. Discussion

Although the p-value did not reach statistical significance, we believe that p-value this low is still noteworthy given the low sample size of Converse's failure data. We recommend conducting a study to compare the failure CHP expression of and IEL failure threshold in cerebral arteries from various animals used as models for humans against the response of human tissue. This will increase the efficiency of translating the study of ECM damage to humans as we will have confidence that the animal model accurately reflects the human response.

CHAPTER 8

CONCLUSION

This dissertation explores mechanical and molecular damage of cerebral arteries at various strain-rates. The definition of the material's rate dependent properties, including failure stress and stretch, in Chapter 3 motivates the identification of a rate-induced shift of tropocollagen denaturation in Chapter 4, followed by an exploration of rate effects in the mechanical softening of overstretched tissue in Chapter 5. Exploratory studies in Chapter 6 provide guidance for future research directions. The first study provides a hyperelastic model of cerebral arteries axially stretched to failure intended for implementation in FE models of TBI that do not account for softening. The next one shows a definite reduction in the amount of denatured tropocollagen in arteries failed at high strain rates, although it remains to be elucidated whether this change in denaturation is a result of increased strain rate, decreased failure stretch, or a coupled mechanism. The third study explores softening of the viscoelastic properties of cerebral arteries following overstretch across four orders of magnitude of strain rate. Several exploratory studies were conducted to guide future research. These included a dimethylmethylene blue (DMMB) study of GAG presence before and after overstretch and an electron microscopy (SEM and TEM) examination of fibril structure. Finally, an investigation of inter-species differences in ECM disruption was conducted in Chapter 7.

6.1 Synopsis of Chapter 3: Mechanical rate dependence

1. The failure properties of Göttingen minipig cerebral arteries are strain rate dependent, as evidenced by a significant increase in failure stress and a significant decrease in failure stretch at high ($>100 \text{ s}^{-1}$) strain rates compared to quasi-static (0.01 s^{-1}) strain rates. This adds another data point supporting the existence of rate dependence in cerebral arteries to a conflicting archive of the subject.
2. Rate dependence (as identified by a statistically significant change in stress at a given stretch) was not observed below a stretch of 1.23. While this could be a manifestation of a viscoelastic property (i.e., non-linear relaxation increases the effect size of viscoelasticity at higher stretch ratios), it could also be a result of poor signal-to-noise ratio at the lower stretch levels.
3. A single-fiber hyper-viscoelastic model was fit to the data, providing a ready-to-implement constitutive model for FE modeling. This model, fit up to failure, considers the entire load curve elastic. This is clearly not a physically accurate depiction of mechanical damage accumulated during loading, yet it describes full-deformation stiffness without tracking the evolution of plasticity (at considerable computational cost).

6.2 Synopsis of Chapter 4: Tropocollagen denaturation

1. The amount of tropocollagen denaturation observed in tests to failure decreases with increasing strain rates, although it remains to be elucidated whether this change is simply a result of the decreased failure stretch of the tissue at high strain rates. This observation implies that the biologic response of tissue to damage may be significantly different following severe deformations at either quasi-static or

- high rates. Further, the observed rate dependence on denaturation confirms that rate must be considered when designing experiments to explore ECM disruption.
2. Damage to transversely loaded fibers was observed, potentially challenging the notion that fibers are exclusively damaged from loading aligned with the fiber direction. This result was incidental (i.e., we did not set out to study transverse fiber damage). Therefore additional experiments must be curated to verify the results and elucidate the mechanism behind transverse damage to the fiber. Regardless, these data challenge the contemporary assumption that collagenous tissue is damaged primarily during loading aligned with collagen fiber directions, such as that predicted in [53].

6.3 Synopsis of Chapter 5: Softening of viscoelastic properties

1. The elastic and viscoelastic properties of cerebral arteries are softened equally following overstretch. This is convenient for the formulation of continuum damage models, as it implies a single damage term can account for changes in both the elastic and viscoelastic properties of a continuum damage model.
2. The rate of overstretch does not affect the softening behavior of tissue. Similar to point 1, this result suggests rate does not need to be considered when calculating the magnitude of damage evolution in a continuum damage model.
3. Severe softening is observed in the absence of widespread tropocollagen denaturation. This finding suggests that another mechanism (aside from tropocollagen denaturation) drives softening resulting from deformations maintained below the yield point.

4. Viscoelasticity was identified below a stretch of $1.1 * \lambda_{IV}$, in contrast to Chapter 3. This suggests that a poor signal-to-noise ratio was responsible for the previously identified increased viscoelastic threshold.

6.4 Synopsis of Chapter 6: Exploratory investigations

1. GAGs do not appear to be disassociated from tissue following stretch to failure, although this may be due to low sensitivity of the assay
2. Small cerebral arteries (<1 mm diameters) are challenging to prepare for electron microscopy. Specifically, curling of the tissue during sample preparation increases surface charging during SEM and prevents consistent imaging of target layers in TEM.

6.5 Synopsis of Chapter 7: Exploratory interspecies differences

1. There is a likely difference between the progression of tropocollagen denaturation between sheep and pigs.

6.6 Future work

1. Severe near-physiologic softening in the absence of tropocollagen denaturation necessitates experiments to identify other mechanisms of ECM alterations. These non-tropocollagen disruption mechanisms are likely to be more biologically relevant as sub-yield overstretch is presumably much more likely to occur. A promising avenue to explore is a combination of directly measuring permanent set of the interfibrillar crosslinks, such as the study by [122, 128, 143] and high-

resolution imaging of stained proteoglycans, such as [62, 144, 145]. We hypothesize that 1) plastic deformation will be observed in the interfibrillar space, and that 2) the altered interfibrillar strains will be strongly correlated with alterations of the interfibrillar proteoglycan complex, as observed under TEM with GAGs stained by Cupromeronic blue.

2. Many groups have noted that non-linear viscoelasticity (where relaxation is a function of strain, and creep is a function of stress) is much more representative of soft tissue behavior than the quasi-linear approach used in the present work [83, 84, 87, 88]. It clearly follows that an exploration of non-linear viscoelasticity should follow in cerebral arteries. If viscoelasticity is demonstrated to be highly non-linear in cerebral arteries (as anticipated), one should carefully consider the trade-off between more physically accurate representation of the viscoelastic behavior (and the quantifiable improvement of model fit) and the additional parameters and calculations required to utilize a fully non-linear viscoelastic formulation in FE simulations. We hypothesize that non-linear viscoelasticity is more appropriate to describe large deformation viscoelasticity in cerebral arteries.
3. Incompressibility has been shown to be a questionable assumption in many artery experiments [72, 73, 75, 146]. It should clearly be explored in cerebral arteries given the contemporary interest in high deformation overstretch. Measuring the degree of incompressibility will lead to insights on the effect of poroelasticity on the observed rate-dependence of cerebral arteries (as compressibility indicates high fluid flux). Similar to an exploration of non-linear viscoelasticity, one should carefully consider the merit of using a compressible formulation for arterial

- behavior. Does the measurable gain in performance overpower the additional computational cost associated with the more complicated formulation?
4. Deformation between the attachment points of the cannulas was assumed to be homogenous, and needle-to-needle stretch was used. Although this is a weak assumption [147], it is experimentally challenging to apply local strain markers on tissue of this size [142]. Specifically, microspheres tend to move relative to the tissue. The size of the tissue necessitates small ink dots, which are challenging to maintain as the ink diffuses along the surface of the artery. We maintain hope, however, that improved marking techniques are possible on this tissue and will lead to more accurate strain calculations.
 5. It is unclear what the relationship is between strain rate, failure stretch, and tropocollagen denaturation. An outstanding question from Chapter 4 is whether the observed decrease in tropocollagen denaturation in arteries failed at high strain rates is a true rate effect, simply due to a decreased failure strain, or a coupled mechanism. Zitnay *et al.* showed rate dependence in the structural deformation of tropocollagen and a strain dependence on severity of tropocollagen denaturation using molecular dynamics simulations [37]. Their study reinforces the notion that a coupled mechanism where structural viscoelasticity of tropocollagen leads to reduced failure strains and thus lower levels of denaturation at high strain rates. Small- and wide-angle X-ray scattering (WAXS and SAXS) may be able to confirm this theory. X-ray scattering can provide information on the deformations at discrete locations in the collagen hierarchy. Specifically, SAXS could be used to observe fibril strains and WAXS

could observe α -chain and tropocollagen deformations. Improved beamlines enable increased frame rate of X-ray scattering experiments [148], leading to the possibility of monitoring constituents at high strain-rates. We hypothesize that the tropocollagen molecule stiffens at high strain rates, simultaneously decreasing failure strain and the amount of tropocollagen denaturation.

6. Preliminary experiments indicate that ultrastructural disruption is species dependent. Given that we are ultimately concerned with improving the human condition, it is essential to define ultrastructural disruption in human tissue. Comparison between disruption progression in human tissue and that of various other species will ideally indicate the best species to use as a model for human tissue damage.

REFERENCES

- [1] N. Agarwal and R. O. Carare, "Cerebral Vessels: An Overview of Anatomy, Physiology, and Role in the Drainage of Fluids and Solutes," *Front Neurol*, vol. 11, p. 611485, 2020, doi: 10.3389/fneur.2020.611485.
- [2] K. Kenney *et al.*, "Cerebral Vascular Injury in Traumatic Brain Injury," *Exp Neurol*, vol. 275 Pt 3, pp. 353-366, Jan 2016, doi: 10.1016/j.expneurol.2015.05.019.
- [3] K. L. Monson, M. I. Converse, and G. T. Manley, "Cerebral blood vessel damage in traumatic brain injury," *Clin Biomech*, vol. 64, pp. 98-113, Apr 2019, doi: 10.1016/j.clinbiomech.2018.02.011.
- [4] C. L. Zollikofer *et al.*, "Transluminal angioplasty evaluated by electron microscopy," *Radiology*, vol. 153, no. 2, pp. 369-374, 1984, doi: 10.1148/radiology.153.2.6237385.
- [5] A. Sundaramurthy *et al.*, "A 3-D Finite-Element Minipig Model to Assess Brain Biomechanical Responses to Blast Exposure," *Front Bioeng Biotechnol*, vol. 9, p. 757755, 2021, doi: 10.3389/fbioe.2021.757755.
- [6] Y. Hua, S. Lin, and L. Gu, "Relevance of Blood Vessel Networks in Blast-Induced Traumatic Brain Injury," *Comput Math Methods Med*, vol. 2015, p. 928236, 2015, doi: 10.1155/2015/928236.
- [7] L. Zhang *et al.*, "Computational study of the contribution of the vasculature on the dynamic response of the brain," *Stapp Car Crash J*, vol. 46, pp. 145-64, Nov 2002, doi: <https://doi.org/10.4271/2002-22-0008>.
- [8] T. Christian Gasser, "Vascular Tissue Biomechanics: Constitutive Modeling of the Arterial Wall," in *Encyclopedia of Biomedical Engineering*, R. Narayan Ed. Amsterdam: Elsevier Inc., 2019, pp. 265-274.
- [9] G. M. London, "Large arteries haemodynamics: conduit versus cushioning function," *Blood Press Suppl*, vol. 2, pp. 48-51, 1997. [Online]. Available: <https://www.ncbi.nlm.nih.gov/pubmed/9495627>.
- [10] J. L. Zitnay, A. H. Lin, and J. A. Weiss, "Tendons exhibit greater resistance to tissue and molecular-level damage with increasing strain rate during cyclic fatigue," *Acta Biomater*, vol. 134, pp. 435-442, Oct 15 2021, doi: 10.1016/j.actbio.2021.07.045.

- [11] C. A. Lemarie, P. L. Tharaux, and S. Lehoux, "Extracellular matrix alterations in hypertensive vascular remodeling," *J Mol Cell Cardiol*, vol. 48, no. 3, pp. 433-9, Mar 2010, doi: 10.1016/j.yjmcc.2009.09.018.
- [12] E. Anttila, D. Balzani, A. Desyatova, P. Deegan, J. MacTaggart, and A. Kamenskiy, "Mechanical damage characterization in human femoropopliteal arteries of different ages," *Acta Biomater*, vol. 90, pp. 225-240, May 2019, doi: 10.1016/j.actbio.2019.03.053.
- [13] G. Unnikrishnan *et al.*, "A 3-D Rat Brain Model for Blast-Wave Exposure: Effects of Brain Vasculature and Material Properties," *Ann Biomed Eng*, vol. 47, no. 9, pp. 2033-2044, Sep 2019, doi: 10.1007/s10439-019-02277-2.
- [14] J. E. Scott, "Elasticity in extracellular matrix 'shape modules' of tendon, cartilage, etc. A sliding proteoglycan-filament model," *J Physiol*, vol. 553, no. Pt 2, pp. 335-43, Dec 1 2003, doi: 10.1113/jphysiol.2003.050179.
- [15] M. R. Bersi, C. Bellini, J. D. Humphrey, and S. Avril, "Local variations in material and structural properties characterize murine thoracic aortic aneurysm mechanics," *Biomech Model Mechanobiol*, vol. 18, no. 1, pp. 203-218, Feb 2019, doi: 10.1007/s10237-018-1077-9.
- [16] T. Christian Gasser, "An irreversible constitutive model for fibrous soft biological tissue: a 3-D microfiber approach with demonstrative application to abdominal aortic aneurysms," *Acta Biomater*, vol. 7, no. 6, pp. 2457-66, Jun 2011, doi: 10.1016/j.actbio.2011.02.015.
- [17] G. A. Holzapfel, T. C. Gasser, and M. Stadler, "A structural model for the viscoelastic behavior of arterial walls: Continuum formulation and finite element analysis," (in English), *European Journal of Mechanics a-Solids*, vol. 21, no. 3, pp. 441-463, May-Jun 2002, doi: Pii S0997-7538(01)01206-2
Doi 10.1016/S0997-7538(01)01206-2.
- [18] H. Geckil, F. Xu, X. Zhang, S. Moon, and U. Demirci, "Engineering hydrogels as extracellular matrix mimics," *Nanomedicine*, vol. 5, no. 3, pp. 469-484, 2010, doi: 10.2217/nnm.10.12.
- [19] X. Guan *et al.*, "Development of hydrogels for regenerative engineering," *Biotechnology Journal*, vol. 12, no. 5, p. 1600394, 2017, doi: 10.1002/biot.201600394.
- [20] W. R. Castaneda-Zuniga *et al.*, "The mechanism of balloon angioplasty," *Radiology*, vol. 135, no. 3, pp. 565-571, 1980, doi: 10.1148/radiology.135.3.7384437.
- [21] H. Weisbecker, D. M. Pierce, P. Regitnig, and G. A. Holzapfel, "Layer-specific damage experiments and modeling of human thoracic and abdominal aortas with non-atherosclerotic intimal thickening," *J Mech Behav Biomed Mater*, vol. 12, pp. 93-106, Aug 2012, doi: 10.1016/j.jmbbm.2012.03.012.
- [22] N. Austin, L. M. DiFrancesco, and W. Herzog, "Microstructural Damage in Arterial Tissue Exposed to Repeated Tensile Strains," vol. 33, no. 1, pp. 14-19, 2010, doi: 10.1016/j.jmpt.2009.11.006.
- [23] E. D. Bell, A. J. Donato, and K. L. Monson, "Cerebrovascular dysfunction following subfailure axial stretch," vol. 65, pp. 627-633, 2017, doi: 10.1016/j.jmbbm.2016.09.028.

- [24] S. Sherifova and G. A. Holzapfel, "Biomechanics of aortic wall failure with a focus on dissection and aneurysm: A review," *Acta Biomaterialia*, vol. 99, pp. 1-17, 2019, doi: 10.1016/j.actbio.2019.08.017.
- [25] Y. Kawamura, S. I. Murtada, F. Gao, X. Liu, G. Tellides, and J. D. Humphrey, "Adventitial remodeling protects against aortic rupture following late smooth muscle-specific disruption of TGF β signaling," *Journal of the Mechanical Behavior of Biomedical Materials*, vol. 116, p. 104264, 2021, doi: 10.1016/j.jmbbm.2020.104264.
- [26] E. D. Bell, J. W. Sullivan, and K. L. Monson, "Subfailure overstretch induces persistent changes in the passive mechanical response of cerebral arteries," *Front Bioeng Biotechnol*, vol. 3, no. 2, p. 2, 2015, doi: 10.3389/fbioe.2015.00002.
- [27] M. I. Converse and K. L. Monson, "Biaxial softening of isolated cerebral arteries following axial overstretch," *J Mech Behav Biomed Mater*, vol. 118, p. 104447, Jun 2021, doi: 10.1016/j.jmbbm.2021.104447.
- [28] J. D. Chalupnik, C. H. Daly, and H. C. Merchant, ""Material Properties of Cerebral Blood Vessels" Final Report on Contract No. NIH-69-2232," Univ. of Washington, Seattle, 1971.
- [29] K. L. Monson, W. Goldsmith, N. M. Barbaro, and G. T. Manley, "Axial mechanical properties of fresh human cerebral blood vessels," *J Biomech Eng*, vol. 125, no. 2, pp. 288-94, Apr 2003, doi: 10.1115/1.1554412.
- [30] E. D. Bell, M. Converse, H. Mao, G. Unnikrishnan, J. Reifman, and K. L. Monson, "Material properties of rat middle cerebral arteries at high strain rates," *J Biomech Eng*, vol. 140, no. 7, p. 071004, Mar 19 2018, doi: 10.1115/1.4039625.
- [31] T. L. Willett, R. S. Labow, N. C. Avery, and J. M. Lee, "Increased proteolysis of collagen in an in vitro tensile overload tendon model," *Ann Biomed Eng*, vol. 35, no. 11, pp. 1961-72, Nov 2007, doi: 10.1007/s10439-007-9375-x.
- [32] T. L. Willett, R. S. Labow, and J. M. Lee, "Mechanical overload decreases the thermal stability of collagen in an in vitro tensile overload tendon model," *J Orthop Res*, vol. 26, no. 12, pp. 1605-10, Dec 2008, doi: 10.1002/jor.20672.
- [33] N. C. Chambers, T. W. Herod, and S. P. Veres, "Ultrastructure of tendon rupture depends on strain rate and tendon type," *J Orthop Res*, vol. 36, no. 11, pp. 2842-2850, Nov 2018, doi: 10.1002/jor.24067.
- [34] N. Famaey, E. Kuhl, G. A. Holzapfel, and J. Vander Sloten, "Cardiovascular Tissue Damage: An Experimental and Computational Framework," in *Computer Models in Biomechanics*, 2013, ch. Chapter 10, pp. 129-148.
- [35] G. A. Holzapfel and B. Fereidoonzhad, "Modeling of Damage in Soft Biological Tissues," in *Biomechanics of Living Organs*, 2017, pp. 101-123.
- [36] S. P. Veres and J. M. Lee, "Designed to fail: a novel mode of collagen fibril disruption and its relevance to tissue toughness," *Biophys J*, vol. 102, no. 12, pp. 2876-84, Jun 20 2012, doi: 10.1016/j.bpj.2012.05.022.
- [37] J. L. Zitnay *et al.*, "Molecular level detection and localization of mechanical damage in collagen enabled by collagen hybridizing peptides," *Nat Commun*, vol. 8, p. 14913, Mar 22 2017, doi: 10.1038/ncomms14913.
- [38] M. Marino, M. I. Converse, K. L. Monson, and P. Wriggers, "Molecular-level collagen damage explains softening and failure of arterial tissues: A quantitative interpretation of CHP data with a novel elasto-damage model," *J Mech Behav*

- Biomed Mater*, vol. 97, pp. 254-271, Sep 2019, doi: 10.1016/j.jmbbm.2019.04.022.
- [39] M. I. Converse, R. G. Walther, J. T. Ingram, Y. Li, S. M. Yu, and K. L. Monson, "Detection and characterization of molecular-level collagen damage in overstretched cerebral arteries," *Acta Biomater*, vol. 67, pp. 307-318, Feb 2018, doi: 10.1016/j.actbio.2017.11.052.
- [40] J. L. Zitnay *et al.*, "Accumulation of collagen molecular unfolding is the mechanism of cyclic fatigue damage and failure in collagenous tissues," *Science Advances*, vol. 6, no. 35, p. eaba2795, 2020, doi: 10.1126/sciadv.aba2795.
- [41] J. C. Simo, "On a fully three-dimensional finite-strain viscoelastic damage model: Formulation and computational aspects," *Computer Methods in Applied Mechanics and Engineering*, vol. 60, no. 2, pp. 153-173, 1987, doi: 10.1016/0045-7825(87)90107-1.
- [42] P. J. Arnoux, P. Chabrand, M. Jean, and J. Bonnoit, "A visco-hyperelastic model with damage for the knee ligaments under dynamic constraints," *Comput Methods Biomech Biomed Engin*, vol. 5, no. 2, pp. 167-74, Apr 2002, doi: 10.1080/10255840290010283.
- [43] T. C. Gasser, "Damage in Vascular Tissues and Its Modeling," in *Material Parameter Identification and Inverse Problems in Soft Tissue Biomechanics*, (CISM International Centre for Mechanical Sciences, 2017, ch. Chapter 4, pp. 85-118.
- [44] E. Peña, B. Calvo, M. A. Martínez, and M. Doblaré, "An anisotropic visco-hyperelastic model for ligaments at finite strains. Formulation and computational aspects," vol. 44, no. 3-4, pp. 760-778, 2007, doi: 10.1016/j.ijstr.2006.05.018.
- [45] E. Maher, M. Early, A. Creane, C. Lally, and D. J. Kelly, "Site specific inelasticity of arterial tissue," *J Biomech*, vol. 45, no. 8, pp. 1393-9, May 11 2012, doi: 10.1016/j.jbiomech.2012.02.026.
- [46] A. Giudici, I. B. Wilkinson, and A. W. Khir, "Review of the Techniques Used for Investigating the Role Elastin and Collagen Play in Arterial Wall Mechanics," *IEEE Reviews in Biomedical Engineering*, vol. 14, pp. 256-269, 2021, doi: 10.1109/rbme.2020.3005448.
- [47] M. I. Converse, K. S. Nye, M. J. Dahl, K. H. Albertine, and K. L. Monson, "Stretch-Induced Intimal Failure in Isolated Cerebral Arteries as a Function of Development," *Ann Biomed Eng*, vol. 49, no. 12, pp. 3540-3549, Dec 2021, doi: 10.1007/s10439-021-02869-x.
- [48] B. K. Wicker, H. P. Hutchens, Q. Wu, A. T. Yeh, and J. D. Humphrey, "Normal basilar artery structure and biaxial mechanical behaviour," *Comput Methods Biomech Biomed Engin*, vol. 11, no. 5, pp. 539-51, Oct 2008, doi: 10.1080/10255840801949793.
- [49] P. B. Canham, P. Whittaker, S. E. Barwick, and M. E. Schwab, "Effect of pressure on circumferential order of adventitial collagen in human brain arteries," *Can J Physiol Pharmacol*, vol. 70, no. 2, pp. 296-305, Feb 1992, doi: 10.1139/y92-037.
- [50] J. D. Humphrey, "Mechanics of the arterial wall: review and directions," *Crit Rev Biomed Eng*, vol. 23, no. 1-2, 1/2, pp. 1-162, 1995. [Online]. Available: <https://www.ncbi.nlm.nih.gov/pubmed/8665806>.

- [51] V. Bolduc, N. Thorin-Trescases, and E. Thorin, "Endothelium-dependent control of cerebrovascular functions through age: exercise for healthy cerebrovascular aging," *Am J Physiol Heart Circ Physiol*, vol. 305, no. 5, pp. H620-33, Sep 1 2013, doi: 10.1152/ajpheart.00624.2012.
- [52] S. Greenwald, "Ageing of the conduit arteries," *The Journal of Pathology*, vol. 211, no. 2, pp. 157-172, 2007, doi: 10.1002/path.2101.
- [53] H. Weisbecker, C. Viertler, D. M. Pierce, and G. A. Holzapfel, "The role of elastin and collagen in the softening behavior of the human thoracic aortic media," *J Biomech*, vol. 46, no. 11, pp. 1859-65, Jul 26 2013, doi: 10.1016/j.jbiomech.2013.04.025.
- [54] J. M. Mattson, R. Turcotte, and Y. Zhang, "Glycosaminoglycans contribute to extracellular matrix fiber recruitment and arterial wall mechanics," 2016, doi: 10.1007/s10237-016-0811-4.
- [55] N. M. Ghadie, J.-P. St-Pierre, and M. R. Labrosse, "The Contribution of Glycosaminoglycans/Proteoglycans to Aortic Mechanics in Health and Disease: A Critical Review," *IEEE Transactions on Biomedical Engineering*, vol. 68, no. 12, pp. 3491-3500, 2021, doi: 10.1109/tbme.2021.3074053.
- [56] K. Grote *et al.*, "Mechanical stretch enhances mRNA expression and proenzyme release of matrix metalloproteinase-2 (MMP-2) via NAD(P)H oxidase-derived reactive oxygen species," *Circ Res*, vol. 92, no. 11, pp. e80-6, Jun 13 2003, doi: 10.1161/01.RES.0000077044.60138.7C.
- [57] T. J. Wess, "Collagen Fibrillar Structure and Hierarchies," in *Collagen*, P. Fratzl Ed.: Springer US, 2008, ch. Chapter 3, pp. 49-80.
- [58] P. Talusan, "Analysis of Intimal Proteoglycans in Atherosclerosis-prone and Atherosclerosis-resistant Human Arteries by Mass Spectrometry," vol. 4, no. 9, pp. 1350-1357, 2005, doi: 10.1074/mcp.m500088-mcp200.
- [59] B. Depalle, Z. Qin, S. J. Shefelbine, and M. J. Buehler, "Influence of cross-link structure, density and mechanical properties in the mesoscale deformation mechanisms of collagen fibrils," *Journal of the Mechanical Behavior of Biomedical Materials*, vol. 52, pp. 1-13, 2015, doi: 10.1016/j.jmbbm.2014.07.008.
- [60] Y. Li, G. Fessel, M. Georgiadis, and J. G. Snedeker, "Advanced glycation end-products diminish tendon collagen fiber sliding," *Matrix Biol*, vol. 32, no. 3-4, pp. 169-77, Apr 24 2013, doi: 10.1016/j.matbio.2013.01.003.
- [61] J. M. Lee and S. P. Veres, "Advanced glycation end-product cross-linking inhibits biomechanical plasticity and characteristic failure morphology of native tendon," *J Appl Physiol (1985)*, vol. 126, no. 4, pp. 832-841, Apr 1 2019, doi: 10.1152/jappphysiol.00430.2018.
- [62] P. Fratzl, "Collagen: Structure and Mechanics," 2008, doi: 10.1007/978-0-387-73906-9_11.
- [63] C. Hoop, J. Zhu, A. Nunes, D. Case, and J. Baum, "Revealing Accessibility of Cryptic Protein Binding Sites within the Functional Collagen Fibril," *Biomolecules*, vol. 7, no. 4, p. 76, 2017, doi: 10.3390/biom7040076.
- [64] K. d. Mark, "Localization of Collagen Types in Tissues Article," *International Review of Connective Tissue Research*, vol. 9, pp. 265-324, 1981.

- [65] M. R. Buckley *et al.*, "Distributions of types I, II and III collagen by region in the human supraspinatus tendon," *Connective Tissue Research*, vol. 54, no. 6, pp. 374-379, 2013, doi: 10.3109/03008207.2013.847096.
- [66] S. G. M. Uzel and M. J. Buehler, "Molecular structure, mechanical behavior and failure mechanism of the C-terminal cross-link domain in type I collagen," *Journal of the Mechanical Behavior of Biomedical Materials*, vol. 4, no. 2, pp. 153-161, 2011, doi: 10.1016/j.jmbbm.2010.07.003.
- [67] M. D. Shoulders and R. T. Raines, "Collagen structure and stability," *Annu Rev Biochem*, vol. 78, pp. 929-58, 2009, doi: 10.1146/annurev.biochem.77.032207.120833.
- [68] F. Bianchi, F. Hofmann, A. J. Smith, and M. S. Thompson, "Probing multi-scale mechanical damage in connective tissues using X-ray diffraction," *Acta Biomater*, vol. 45, pp. 321-327, Nov 2016, doi: 10.1016/j.actbio.2016.08.027.
- [69] Y. Yamamoto, R. R. Smith, and D. H. Bernanke, "Mechanism of action of balloon angioplasty in cerebral vasospasm," *Neurosurgery*, vol. 30, no. 1, pp. 1-5; discussion 5-6, Jan 1992, doi: 10.1227/00006123-199201000-00001.
- [70] G. A. Holzapfel, T. C. Gasser, and R. W. Ogden, "A new constitutive framework for arterial wall mechanics and a comparative study of material models," (in English), *Journal of Elasticity*, vol. 61, no. 1-3, pp. 1-48, 2000, doi: Doi 10.1023/A:1010835316564.
- [71] E. Pena, V. Alastrue, A. Laborda, M. A. Martinez, and M. Doblare, "A constitutive formulation of vascular tissue mechanics including viscoelasticity and softening behaviour," *J Biomech*, vol. 43, no. 5, pp. 984-9, Mar 22 2010, doi: 10.1016/j.jbiomech.2009.10.046.
- [72] G. Faury, G. M. Maher, D. Y. Li, M. T. Keating, R. P. Mecham, and W. A. Boyle, "Relation between outer and luminal diameter in cannulated arteries," *American Journal of Physiology-Heart and Circulatory Physiology*, vol. 277, no. 5, pp. H1745-H1753, 1999, doi: 10.1152/ajpheart.1999.277.5.H1745.
- [73] F. Di Puccio, S. Celi, and P. Forte, "Review of Experimental Investigations on Compressibility of Arteries and Introduction of a New Apparatus," *Experimental Mechanics*, vol. 52, no. 7, pp. 895-902, 2012, doi: 10.1007/s11340-012-9614-4.
- [74] P. Skacel and J. Bursa, "Poissons ratio of arterial wall - Inconsistency of constitutive models with experimental data," *J Mech Behav Biomed Mater*, vol. 54, pp. 316-27, Feb 2016, doi: 10.1016/j.jmbbm.2015.09.029.
- [75] Z. Yosibash, I. Manor, I. Gilad, and U. Willentz, "Experimental evidence of the compressibility of arteries," *Journal of the Mechanical Behavior of Biomedical Materials*, vol. 39, pp. 339-354, 2014, doi: 10.1016/j.jmbbm.2014.07.030.
- [76] K. L. Monson, N. M. Barbaro, and G. T. Manley, "Biaxial Response of Passive Human Cerebral Arteries," vol. 36, no. 12, pp. 2028-2041, 2008, doi: 10.1007/s10439-008-9578-9.
- [77] H. W. Weizsacker, H. Lambert, and K. Pascale, "Analysis of the passive mechanical properties of rat carotid arteries," *J Biomech*, vol. 16, no. 9, pp. 703-15, 1983, doi: 10.1016/0021-9290(83)90080-5.
- [78] R. Collins and W. C. L. Hu, "DYNAMIC DEFORMATION EXPERIMENTS ON AORTIC TISSUE," *Journal of Biomechanics*, vol. 5, no. 4, pp. 333-334, 335-337, 1972.

- [79] D. Mohan and J. W. Melvin, "Failure properties of passive human aortic tissue. I-uni-axial tension tests," *J Biomech*, vol. 15, no. 11, pp. 887-902, 1982, doi: 10.1016/0021-9290(82)90055-0.
- [80] B. D. Stemper, N. Yoganandan, and F. A. Pintar, "Mechanics of arterial subfailure with increasing loading rate," *J Biomech*, vol. 40, no. 8, pp. 1806-12, 2007, doi: 10.1016/j.jbiomech.2006.07.005.
- [81] R. W. Lawton, "Measurements on the Elasticity and Damping of Isolated Aortic Strips of the Dog," *Circulation Research*, vol. 3, no. 4, pp. 403-408, 1955, doi: 10.1161/01.res.3.4.403.
- [82] M. C. Lee and R. C. Haut, "Strain rate effects on tensile failure properties of the common carotid artery and jugular veins of ferrets," *J Biomech*, vol. 25, no. 8, pp. 925-7, Aug 1992, doi: 10.1016/0021-9290(92)90232-p.
- [83] D. J. Patel, W. K. Tucker, and J. S. Janicki, "Dynamic elastic properties of the aorta in radial direction," *J Appl Physiol*, vol. 28, no. 5, pp. 578-82, May 1970, doi: 10.1152/jappl.1970.28.5.578.
- [84] P. P. Provenzano, R. S. Lakes, D. T. Corr, and R. Vanderby, Jr., "Application of nonlinear viscoelastic models to describe ligament behavior," *Biomech Model Mechanobiol*, vol. 1, no. 1, pp. 45-57, Jun 2002, doi: 10.1007/s10237-002-0004-1.
- [85] Y.-C. Fung, *Biomechanics: Mechanical Properties of Living Tissues*. New York: Springer-Verlag, 1993.
- [86] M. A. Puso and J. A. Weiss, "Finite element implementation of anisotropic quasi-linear viscoelasticity using a discrete spectrum," *Journal of biomechanical engineering*, vol. 120, no. 1, pp. 62-70, 1998.
- [87] G. M. Thornton, A. Oliynyk, C. B. Frank, and N. G. Shrive, "Ligament creep cannot be predicted from stress relaxation at low stress: A biomechanical study of the rabbit medial collateral ligament," *Journal of Orthopaedic Research*, vol. 15, no. 5, pp. 652-656, 1997, doi: 10.1002/jor.1100150504.
- [88] A. Nekouzadeh, K. M. Pryse, E. L. Elson, and G. M. Genin, "A simplified approach to quasi-linear viscoelastic modeling," *Journal of Biomechanics*, vol. 40, no. 14, pp. 3070-3078, 2007, doi: 10.1016/j.jbiomech.2007.03.019.
- [89] S. Ji *et al.*, "Group-Wise Evaluation and Comparison of White Matter Fiber Strain and Maximum Principal Strain in Sports-Related Concussion," *Journal of Neurotrauma*, vol. 32, no. 7, pp. 441-454, 2015, doi: 10.1089/neu.2013.3268.
- [90] "Abaqus Analysis User's Manual." Simulia.
<http://130.149.89.49:2080/v6.9ef/books/usb/default.htm?startat=pt05ch19s07abm12.html> (accessed 2021).
- [91] S. Mass, H. M., W. J., and A. G. "FEBio Theory Manual."
https://help.febio.org/FEBioTheory/FEBio_tm_3-4.html (accessed).
- [92] C. Miehe, "On the representation of Prandtl-Reuss tensors within the framework of multiplicative elastoplasticity," *International journal of plasticity*, vol. 10, no. 6, pp. 609-621, 1994.
- [93] D. Balzani, S. Brinkhues, and G. A. Holzapfel, "Constitutive framework for the modeling of damage in collagenous soft tissues with application to arterial walls," *Computer Methods in Applied Mechanics and Engineering*, vol. 213-216, pp. 139-151, 2012, doi: 10.1016/j.cma.2011.11.015.

- [94] M. Ghasemi, D. R. Nolan, and C. Lally, "An investigation into the role of different constituents in damage accumulation in arterial tissue and constitutive model development," *Biomech Model Mechanobiol*, vol. 17, no. 6, pp. 1757-1769, Dec 2018, doi: 10.1007/s10237-018-1054-3.
- [95] C. Miehe and J. Keck, "Superimposed finite elastic-viscoelastic-plastoelastic stress response with damage in filled rubbery polymers. Experiments, modelling and algorithmic implementation," *Pergamon*, vol. 48, no. 2, pp. 323-365, 2000.
- [96] G. A. Holzapfel and R. W. Ogden, "A damage model for collagen fibres with an application to collagenous soft tissues," *Proc Math Phys Eng Sci*, vol. 476, no. 2236, p. 20190821, Apr 2020, doi: 10.1098/rspa.2019.0821.
- [97] L. M. Kachanov, "Time of the Rupture Process under Creep Conditions," *Izvestiia Akademii nauk SSSR. Bulletin de l'Académie des sciences de l'URSS. Classe des sciences techniques. Otdelenie tekhnicheskikh nauk*, vol. 8, pp. 26-31, 1958
- [98] E. Maher, A. Creane, C. Lally, and D. J. Kelly, "An anisotropic inelastic constitutive model to describe stress softening and permanent deformation in arterial tissue," *J Mech Behav Biomed Mater*, vol. 12, pp. 9-19, Aug 2012, doi: 10.1016/j.jmbbm.2012.03.001.
- [99] E. Kröner, "Allgemeine Kontinuumstheorie der Versetzungen und Eigenspannungen," *Archive for Rational Mechanics and Analysis*, vol. 4, pp. 273-334, 1959.
- [100] E. Peña, B. Calvo, M. A. Martínez, and M. Doblaré, "On finite-strain damage of viscoelastic-fibred materials. Application to soft biological tissues," *International Journal for Numerical Methods in Engineering*, vol. 74, no. 7, pp. 1198-1218, 2008, doi: 10.1002/nme.2212.
- [101] Y. Zhu, G. Kang, Q. Kan, and C. Yu, "A finite viscoelastic-plastic model for describing the uniaxial ratcheting of soft biological tissues," *J Biomech*, vol. 47, no. 5, pp. 996-1003, Mar 21 2014, doi: 10.1016/j.jbiomech.2014.01.004.
- [102] F. F. Fontenele and N. Bouklas, "Understanding the inelastic response of collagen fibrils: A viscoelastic-plastic constitutive model," *Acta Biomater*, Jul 12 2022, doi: 10.1016/j.actbio.2022.07.011.
- [103] M. M. Panjabi, P. Moy, T. R. Oxland, and J. Cholewicki, "Subfailure injury affects the relaxation behavior of rabbit ACL," *Clin Biomech (Bristol, Avon)*, vol. 14, no. 1, pp. 24-31, Jan 1999, doi: 10.1016/s0268-0033(98)00046-1.
- [104] S. Duenwald-Kuehl, J. Kondratko, R. S. Lakes, and R. Vanderby, Jr., "Damage mechanics of porcine flexor tendon: mechanical evaluation and modeling," *Ann Biomed Eng*, vol. 40, no. 8, pp. 1692-707, Aug 2012, doi: 10.1007/s10439-012-0538-z.
- [105] B. Kurz, M. Jin, P. Patwari, D. M. Cheng, M. W. Lark, and A. J. Grodzinsky, "Biosynthetic response and mechanical properties of articular cartilage after injurious compression," *J Orthop Res*, vol. 19, no. 6, pp. 1140-6, Nov 2001, doi: 10.1016/S0736-0266(01)00033-X.
- [106] E. D. Bell, J. W. Sullivan, and K. L. Monson, "Subfailure overstretch induces persistent changes in the passive mechanical response of cerebral arteries," (in English), *Frontiers in Bioengineering and Biotechnology*, Original Research vol. 3, p. 2, 2015-January-28 2015, doi: 10.3389/fbioe.2015.00002.

- [107] N. Pearson *et al.*, "A Strain Rate-Dependent Constitutive Model for Gottingen Minipig Cerebral Arteries," *J Biomech Eng*, vol. 144, no. 8, Aug 1 2022, doi: 10.1115/1.4053796.
- [108] D. R. Eyre and J.-J. Wu, "Collagen Cross-Links," Springer Berlin Heidelberg, 2005, pp. 207-229.
- [109] K. A. Piez, "Cross-Linking of Collagen and Elastin," *Annual Review of Biochemistry*, vol. 37, no. 1, pp. 547-570, 1968, doi: 10.1146/annurev.bi.37.070168.002555.
- [110] Y. Li *et al.*, "Targeting collagen strands by photo-triggered triple-helix hybridization," *Proceedings of the National Academy of Sciences*, vol. 109, no. 37, pp. 14767-14772, 2012, doi: 10.1073/pnas.1209721109.
- [111] J. Hwang *et al.*, "In Situ Imaging of Tissue Remodeling with Collagen Hybridizing Peptides," *ACS Nano*, vol. 11, no. 10, pp. 9825-9835, 2017, doi: 10.1021/acsnano.7b03150.
- [112] S. E. Szczesny, C. Aepli, A. David, and R. L. Mauck, "Fatigue loading of tendon results in collagen kinking and denaturation but does not change local tissue mechanics," *J Biomech*, vol. 71, pp. 251-256, Apr 11 2018, doi: 10.1016/j.jbiomech.2018.02.014.
- [113] A. H. Lin, A. N. Allan, J. L. Zitnay, J. L. Kessler, S. M. Yu, and J. A. Weiss, "Collagen denaturation is initiated upon tissue yield in both positional and energy-storing tendons," *Acta Biomater*, vol. 118, pp. 153-160, Dec 2020, doi: 10.1016/j.actbio.2020.09.056.
- [114] A. H. Lin, J. L. Zitnay, Y. Li, S. M. Yu, and J. A. Weiss, "Microplate assay for denatured collagen using collagen hybridizing peptides," *J Orthop Res*, vol. 37, no. 2, pp. 431-438, Feb 2019, doi: 10.1002/jor.24185.
- [115] S. Brown, M. Worsfold, and C. Sharp, "Microplate Assay for the Measurement of Hydroxyproline in Acid-Hydrolyzed Tissue Samples," *BioTechniques*, vol. 30, no. 1, pp. 38-42, 2001, doi: 10.2144/01301bm06.
- [116] Zhilei, H. Kahn, R. Ballarini, and Steven, "Viscoelastic Properties of Isolated Collagen Fibrils," *Biophysical Journal*, vol. 100, no. 12, pp. 3008-3015, 2011, doi: 10.1016/j.bpj.2011.04.052.
- [117] T. J. Bonner *et al.*, "Strain-rate sensitivity of the lateral collateral ligament of the knee," *J Mech Behav Biomed Mater*, vol. 41, pp. 261-70, Jan 2015, doi: 10.1016/j.jmbbm.2014.07.004.
- [118] G. Holzapfel, *Nonlinear Solid Mechanics: A continuum approach for engineering*. Chichester: Wiley, 2000.
- [119] P. Kannus, "Structure of the tendon connective tissue," *Scandinavian Journal of Medicine & Science in Sports*, vol. 10, no. 6, pp. 312-320, 2000, doi: 10.1034/j.1600-0838.2000.010006312.x.
- [120] S. P. Veres, E. P. Brennan-Pierce, and J. M. Lee, "Macrophage-like U937 cells recognize collagen fibrils with strain-induced discrete plasticity damage," *Journal of Biomedical Materials Research Part A*, vol. 103, no. 1, pp. 397-408, 2015, doi: 10.1002/jbm.a.35156.
- [121] E. G. Lakatta, "Arterial and cardiac aging: major shareholders in cardiovascular disease enterprises: Part III: cellular and molecular clues to heart and arterial

- aging," *Circulation*, vol. 107, no. 3, pp. 490-7, Jan 28 2003, doi: 10.1161/01.cir.0000048894.99865.02.
- [122] A. H. Lee and D. M. Elliott, "Multi-Scale Loading and Damage Mechanisms of Plantaris and Rat Tail Tendons," *J Orthop Res*, vol. 37, no. 8, pp. 1827-1837, Aug 2019, doi: 10.1002/jor.24309.
- [123] S. J. Baldwin, L. Kreplak, and J. M. Lee, "MMP-9 selectively cleaves non-D-banded material on collagen fibrils with discrete plasticity damage in mechanically-overloaded tendon," *J Mech Behav Biomed Mater*, vol. 95, pp. 67-75, Jul 2019, doi: 10.1016/j.jmbbm.2019.03.020.
- [124] D. S. DeWitt and D. S. Prough, "Traumatic cerebral vascular injury: the effects of concussive brain injury on the cerebral vasculature," *J Neurotrauma*, vol. 20, no. 9, pp. 795-825, Sep 2003, doi: 10.1089/089771503322385755.
- [125] W. N. Hardy *et al.*, "A study of the response of the human cadaver head to impact," *Stapp Car Crash J*, vol. 51, pp. 17-80, Oct 2007. [Online]. Available: <https://www.ncbi.nlm.nih.gov/pubmed/18278591>.
- [126] B. Kurz, A. K. Lemke, J. Fay, T. Pufe, A. J. Grodzinsky, and M. Schunke, "Pathomechanisms of cartilage destruction by mechanical injury," *Ann Anat*, vol. 187, no. 5-6, pp. 473-85, Nov 2005, doi: 10.1016/j.aanat.2005.07.003.
- [127] A. H. Lin, C. A. Slater, C. J. Martinez, S. J. Eppell, S. M. Yu, and J. A. Weiss, "Collagen fibrils from both positional and energy-storing tendons exhibit increased amounts of denatured collagen when stretched beyond the yield point," *Acta Biomater*, Nov 15 2022, doi: 10.1016/j.actbio.2022.11.018.
- [128] S. E. Szczesny and D. M. Elliott, "Interfibrillar shear stress is the loading mechanism of collagen fibrils in tendon," *Acta Biomater*, vol. 10, no. 6, pp. 2582-90, Jun 2014, doi: 10.1016/j.actbio.2014.01.032.
- [129] S. P. Reese, C. J. Underwood, and J. A. Weiss, "Effects of decorin proteoglycan on fibrillogenesis, ultrastructure, and mechanics of type I collagen gels," *Matrix Biol*, vol. 32, no. 7-8, pp. 414-23, Oct-Nov 2013, doi: 10.1016/j.matbio.2013.04.004.
- [130] G. Fessel and J. G. Snedeker, "Equivalent stiffness after glycosaminoglycan depletion in tendon--an ultra-structural finite element model and corresponding experiments," *J Theor Biol*, vol. 268, no. 1, pp. 77-83, Jan 7 2011, doi: 10.1016/j.jtbi.2010.10.007.
- [131] J. D. Humphrey, E. R. Dufresne, and M. A. Schwartz, "Mechanotransduction and extracellular matrix homeostasis," *Nature Reviews Molecular Cell Biology*, vol. 15, no. 12, pp. 802-812, 2014, doi: 10.1038/nrm3896.
- [132] A. Redaelli, S. Vesentini, M. Soncini, P. Vena, S. Mantero, and F. M. Montevecchi, "Possible role of decorin glycosaminoglycans in fibril to fibril force transfer in relative mature tendons—a computational study from molecular to microstructural level," *Journal of Biomechanics*, vol. 36, no. 10, pp. 1555-1569, 2003, doi: 10.1016/s0021-9290(03)00133-7.
- [133] M. Rutgers *et al.*, "PTH decreases in vitro human cartilage regeneration without affecting hypertrophic differentiation," *PLOS ONE*, vol. 14, no. 4, p. e0213483, 2019, doi: 10.1371/journal.pone.0213483.
- [134] T. Iimaa, Y. Ikegami, R. Bual, N. Shirakigawa, and H. Ijima, "Analysis of Sulfated Glycosaminoglycans in ECM Scaffolds for Tissue Engineering

- Applications: Modified Alcian Blue Method Development and Validation," *Journal of Functional Biomaterials*, vol. 10, no. 2, p. 19, 2019, doi: 10.3390/jfb10020019.
- [135] A. W. Palmer, C. G. Wilson, E. J. Baum, and M. E. Levenston, "Composition-function relationships during IL-1-induced cartilage degradation and recovery," *Osteoarthritis and Cartilage*, vol. 17, no. 8, pp. 1029-1039, 2009, doi: 10.1016/j.joca.2009.02.009.
- [136] V. J. Coulson-Thomas and T. F. Gesteira, "Dimethylmethylene Blue Assay (DMMB)," *Bio-Protocol*, vol. 4, no. 18, p. e1236, 2014, doi: 10.21769/BioProtoc.1236.
- [137] A. M. Seligman, H. L. Wasserkrug, and J. S. Hanker, "A new staining method (OTO) for enhancing contrast of lipid--containing membranes and droplets in osmium tetroxide--fixed tissue with osmiophilic thiocarbohydrazide(TCH)," *J Cell Biol*, vol. 30, no. 2, pp. 424-32, Aug 1966, doi: 10.1083/jcb.30.2.424.
- [138] V. Morel and T. M. Quinn, "Cartilage injury by ramp compression near the gel diffusion rate," vol. 22, no. 1, pp. 145-151, 2004, doi: 10.1016/s0736-0266(03)00164-5.
- [139] P. Moran and B. Coats, "Biological Sample Preparation for SEM Imaging of Porcine Retina," *Microscopy Today*, vol. 20, no. 2, pp. 28-31, 2012, doi: 10.1017/s1551929511001374.
- [140] J. G. Neyt, J. A. Buckwalter, and N. C. Carroll, "Use of animal models in musculoskeletal research," *Iowa Orthop J*, vol. 18, pp. 118-23, 1998. [Online]. Available: <https://www.ncbi.nlm.nih.gov/pubmed/9807717>.
- [141] J. B. Casals *et al.*, "The use of animal models for stroke research: a review," *Comp Med*, vol. 61, no. 4, pp. 305-13, Aug 2011. [Online]. Available: <https://www.ncbi.nlm.nih.gov/pubmed/22330245>.
- [142] M. I. Converse, "TRAUMA-INDUCED ALTERATIONS OF CEREBRAL VESSEL MECHANICS AND MICROSTRUCTURE," Ph.D., Mechanical Engineering, University of Utah, Salt Lake City, 2018.
- [143] A. H. Lee, S. E. Szczesny, M. H. Santare, and D. M. Elliott, "Investigating mechanisms of tendon damage by measuring multi-scale recovery following tensile loading," *Acta Biomater*, vol. 57, pp. 363-372, Jul 15 2017, doi: 10.1016/j.actbio.2017.04.011.
- [144] J. E. Scott, "Morphometry of cupromeronic blue-stained proteoglycan molecules in animal corneas, versus that of purified proteoglycans stained in vitro, implies that tertiary structures contribute to corneal ultrastructure.," *J Anat*, vol. 180, no. 1, pp. 155-164, 1992.
- [145] T. L. White *et al.*, "The Structural Role of Elastic Fibers in the Cornea Investigated Using a Mouse Model for Marfan Syndrome," *Invest Ophthalmol Vis Sci*, vol. 58, no. 4, pp. 2106-2116, Apr 1 2017, doi: 10.1167/iovs.16-21358.
- [146] P. Skacel and J. Bursa, "Compressibility of arterial wall - Direct measurement and predictions of compressible constitutive models," *J Mech Behav Biomed Mater*, vol. 90, pp. 538-546, Feb 2019, doi: 10.1016/j.jmbbm.2018.11.004.
- [147] K. L. Monson, V. Mathur, and D. A. Powell, "Deformations and end effects in isolated blood vessel testing," *J Biomech Eng*, vol. 133, no. 1, p. 011005, Jan 2011, doi: 10.1115/1.4002935.

- [148] L. Biron. "Advanced Light Source Upgrade Approved to Start Construction." Berkeley Lab. <https://newscenter.lbl.gov/2022/11/15/advanced-light-source-upgrade-construction/> (accessed December 22, 2022, 2022).